Surface Science Reports 67 (2012) 83–115

Contents lists available at SciVerse ScienceDirect

Surface Science Reports

journal homepage: www.elsevier.com/locate/surfrep

The surface science of graphene: Metal interfaces, CVD synthesis, nanoribbons, chemical modifications, and defects

Matthias Batzill

Department of Physics, University of South Florida, Tampa, FL 33620, USA

ARTICLE INFO

Article history:
Received 30 November 2011
Accepted 1 December 2011
editor: W.H. Weinberg

Keywords:
Graphene
CVD-growth of graphene
Metal/graphene interfaces
Defects
Graphene edge structure
Doping

ABSTRACT

Graphene, a single atomic layer of sp^2 hybridized carbon, exhibits a zero-band gap with linear band dispersion at the Fermi-level, forming a Dirac-cone at the *K*-points of its Brillouin zone. In this review, we focus on basic materials science issues of this intriguing material. The scope of this work is further narrowed by concentrating on graphene grown at transition metal surfaces, mostly under vacuum conditions, and neglecting other graphene synthesis approaches, namely growth on SiC or by graphene oxide reduction. Thus one large section of this review focuses on metal/graphene interfaces. We summarize recent surface science studies on the structure, interaction, and the growth of graphene on various metals. Metal supported graphene is a recurring theme throughout this review as it provides model-systems for studying adsorption and graphene modifications on well-defined, large area samples, and thus is ideal for employing surface science techniques. Other aspects of graphene are also reviewed. Approaches for creating and characterizing graphene nanostructures, in particular graphene nanoribbons, are discussed. Graphene nanoribbons play an important role for potential electronic applications because the lateral electron confinement in the ribbons opens a band-gap in graphene. Materials issues of nanoribbons, like formation of well-defined edges are introduced. Atomic-scale defect-structures in graphene are another topic. The known defect structures in graphene are categorized and atomic scale characterization of these defects by scanning tunneling microscopy (stocktickerSTM) and high resolution transmission electron microscopy (TEM) is illustrated. Important for applications of graphene is our ability of modifying its properties. Therefore, studies of substitutional doping of graphene with nitrogen or boron, hydrogenation or fluorination of graphene, and the adsorption of molecules with strong electron affinity are included in this review. This review is restricted to a summary of surface science studies on well-ordered systems. Other important graphene research areas such as transport measurements on pure and modified graphene are not included. The goal of this review is to give a concise overview of the materials science of graphene from the surface science perspective.

Contents

E-mail address: mbatzill@usf.edu.

0167-5729/$ – see front matter © 2011 Elsevier B.V. All rights reserved.
doi:10.1016/j.surfrep.2011.12.001

1. Introduction

Research on graphene has experienced explosive growth in the last few years. Initial excitement for graphene came from its unusual linear dispersion of the π-band at the Fermi level, which gives rise to new physical properties. The isolation of single layer free-standing graphene from highly oriented pyrolytic graphite (HOPG) and the measurements of many exotic electronic properties of graphene have earned Kostya S. Novoselov and Andre K. Geim the Physics Nobel Prize in 2010. In addition to the exciting physics of the electrons in this material, graphene also possesses other interesting physical properties, such as being the 'strongest' material (by weight) [1] and exhibiting a negative thermal expansion coefficient [2]. Such superlatives and unique properties of graphene motivated much of the fundamental research on this special material. However, this alone does not explain the enormous interest in graphene. Soon after its synthesis, the applied research community became interested in graphene. In particular, many from the carbon-nanotube community changed their focus toward graphene. One practical aspect for the interest in graphene was the prospect of large area graphene wafers and thus the use of lithographical methods for patterning and device fabrication. Such processes are more compatible with existing technologies than, for example, the selection and assembly of carbon-nanotube architectures. Graphene wafers were already available by graphitization of SiC, even before the groundbreaking experiments by Novoselov and Geim, and soon afterward large-area graphene was synthesized by chemical vapor deposition (CVD) growth on metal substrates. Development of transfer procedures from the metal substrate on which graphene is grown on, allowed these wafers to be placed on any arbitrary substrate. The synthesis of graphene on SiC and on metal substrates also brought many surface scientists into the arena of graphene research. The graphene formation on metals had been well known in the surface science community for decades. The increasing interest in graphene meant that these graphene synthesis processes were now re-investigated in more detail and with modern surface science techniques such as low energy electron microscopy (LEEM), scanning tunneling microscopy (STM) and angle resolved photoemission spectroscopy (ARPES) to obtain structural and electronic information. In general the 2D nature of graphene with all its atoms situated at the surface makes this material an obvious object for surface science studies.

Graphene research may be divided in three sub-areas: (i) the characterization of the special physical properties that are originating from the 2D nature of the material and its special electronic band structure, (ii) device applications, and (iii) the materials science of graphene, i.e. making and processing of graphene wafers, doping of graphene by impurities, and interface formation between graphene and dissimilar materials. This review is primarily concerned with the latter. Furthermore, we exclude areas that are already thoroughly reviewed. In particular single and multilayer graphene on SiC single crystal wafers is not included in this review. Information on surface studies of graphene on SiC may be found in other recent reviews [3–5]. Raman spectroscopy has played an important role in the characterization of graphene, Dresselhaus and co-workers have written excellent reviews on the application of this technique for graphene characterization [6,7] and therefore we do not include any Raman spectroscopy studies in this article. Also, formation of graphene by reduction of graphene oxide is not included here.

Although graphene has just recently become a 'hot topic', it is not a new material and therefore we start this review by describing historical highlights in the materials science of graphene.

1.1. A brief history of graphene

Graphene, a single layer of sp^2 bonded carbon atoms, is the basic building block of carbon nanotubes, fullerenes and, of course, graphite and HOPG. Therefore, it is somewhat ironic that the most basic 'building block' achieves 'maturity' last among these carbon materials. However, the concept of graphene is not new. As early as 1947 Wallace [8] showed that a single sheet of sp^2 hybridized carbon would have a linear energy dispersion as function of electron-momentum vector ($E(k)$) at the K-point of the Brillouin zone. The first synthesis of single and multilayer graphene was probably achieved by Boehm in 1962 [9]. Boehm used a method based on the reduction of graphene oxide, which has now been re-discovered as chemical synthesis method of graphene. For many other experimental works on sp^2 carbon the synthesis and commercialization of HOPG crystals in the 1960s was essential. HOPG would also lay the foundation for the work by Novoselov and Geim four decades later. But first, in the 1970's, most interests in carbon materials were on intercalation compounds [10]. Intercalation compounds are single or multilayers of graphene sandwiched in between intercalant layers of guest atoms or molecules.

Before the interest in graphene as a 'nanomaterial', the discovery of fullerenes by Kroto et al. [11] in 1985 and then the identification of carbon nanotubes by Iijima [12] in 1991 were the center of attention. The existence of free-standing graphene was dismissed for some time as not being thermodynamically stable; first by Landau [13] and later by Mermin [14]. On the other hand, formation of supported mono- and multilayer graphene on transition metal substrates was observed by surface scientists in vacuum, either by segregation of carbon containing samples or by exposure of hot samples to hydrocarbons. Graphene was first suggested to form on transition metals by hydrocarbon dissociation from low energy electron diffraction (LEED) observations on Pt(100) in 1968 [15,16]. First scanning tunneling microscopy investigations of graphene on Pt(111) surfaces was performed by the Comsa group [17] in 1991. Blakely and co-workers, studied the segregation behavior of carbon from Ni-crystals by Auger-electron spectroscopy (AES) in 1974 and found the formation of single layer graphene as a thermodynamic stable surface termination while multilayer graphene formed by precipitation of carbon if the samples are cooled to lower temperatures [18]. Single layer graphene on Ni was also obtained by exposure of pure Ni-crystals to hydrocarbons in ultrahigh vacuum (UHV) [19] and electronic decoupling of graphene from the Ni-substrate was investigated by metal intercalation [20]. These early surface science studies of graphene on metals had, however, little motivation in the direction of fundamental properties or applications of graphene in electronic devices. This was different for the studies of graphene formation on SiC. The formation of graphene on SiC was first observed in 1975 by van Bommel et al. [21]. In 2001 the de Heer group developed the process of forming planar graphene layers on SiC substrates further by heating SiC wafers to above 1300 °C. These studies were motivated by the prospect of 2D electronics and in 2004 they published a paper highlighting the 2D electron gas properties of the graphene charge carriers in an electric field [22]. In terms of the characterization of basic physical properties of graphene the breakthrough came, however, with the development of a mechanical exfoliation method of single and multilayer graphene from HOPG by Novoselov and Geim [23–26]. Also at the same time the group around Kim [27,28] developed their own exfoliation method for few-layer graphene. This preparation of high quality graphene allowed the verification of many predicted exotic behaviors of the charge carriers in graphene for which the Physics Nobel Prize was awarded in 2010. From an application perspective the exfoliation method is, however, unlikely to produce the graphene-materials needed for scalable production and device fabrication. Therefore, the above mentioned processes of graphene oxide reduction [29,30] and chemical vapor deposition (CVD) growth processes on metal supports [31,32] have been refined in recent years.

1.2. Outline of this review

The literature on graphene is growing almost exponentially and therefore new developments are reported at an extraordinary pace. Nevertheless, for many aspects a thorough understanding is emerging which will be the basis for future studies and therefore we believe now is a good time to provide a summary of the experimental materials research of graphene. This review summarizes published results up to summer 2011. This review focuses on experimental advances. Theoretical studies are considered if they provide support of experiments in this review.

We start by investigating metal/graphene interfaces. This is a field with a long tradition in the surface science community and has reached maturity. There exist a large number of studies on single crystal substrates and the structure of graphene on these metal substrates is thoroughly characterized for a number of materials. The initial fundamental interest in these metal/graphene interfaces has become of applied interest due to its importance in graphene synthesis by CVD processes. In Section 3 we will investigate processes to form graphene with limited lateral extension, such as graphene nanoribbons. Graphene nanostructures are an important field of graphene research and lateral electron confinement in these nanostructures enables opening of a band gap in graphene. In Section 4 we focus on atomic-scale defects in graphene and at its edges. High resolution transmission electron microscopy and scanning tunneling microscopy have given us insight into defect formation in graphene at the atomic level. Defects can be utilized for modifying graphene properties and may play an important role for chemical functionalization of graphene. In this section we also consider substitutional impurity doping, namely nitrogen and boron doping as extrinsic defects in the graphene sheet. Furthermore, 1D defects, such as grain boundaries of graphene are included in Section 4. Section 5 discusses briefly the formation of chemical derivatives of graphene such as hydrogenated or fluorinated graphene. Section 6 studies interfaces between graphene and molecules. Especially organic interfaces have attracted interest for doping graphene by charge transfer from the organic molecules to graphene to create p- and n-type graphene. Section 7 concludes this review.

2. Graphene/metal interfaces

The observation of graphene-formation on transition metal surfaces dates back to the beginning of surface science studies on single crystal metals. On Pt(111) and Ru(0001) characteristic LEED patterns were observed after annealing to high temperatures. These LEED patterns were identified as originating from carbon segregation from the bulk and formation of graphitic layers. Later, graphene was grown on different metals intentionally by either saturating crystals with carbon outside of the UHV chamber and subsequently characterizing the surface phases as a function of temperature by surface science probes (mainly AES) in UHV, or by exposure of clean (carbon free) metals inside the UHV chamber to hydrocarbons. Of the former studies, the investigations of single and multilayer graphene formation on carbon saturated Ni crystals by Blakely and co-workers stands out [18]. They demonstrated that carbon exists in different forms on Ni(111) at different temperatures. From C_{KVV} AES intensities it was shown that above 1200 K carbon exists only as a dilute phase

at the surface, in a temperature range between 1100 and 1200 K monolayer graphene was observed through carbon segregation to the surface. This phase may be considered a thermodynamic equilibrium phase, i.e. the graphene terminated surface lowers the surface free energy of the system. (Note that the phase stability temperature of monolayer graphene on Ni(111) depends on the carbon concentration in the bulk. We show below that for graphene on Ni with only a small carbon concentration in the bulk the graphene sheet is only stable to ~930 K.) In Blakely et al.'s experiments lowering the temperature below 1100 K caused carbon to precipitate to the surface and multilayer graphene, or graphite, is formed. This precipitation process is driven by the reduced carbon solubility in the Ni-bulk at lower temperatures. These processes are quite relevant for graphene synthesis on Ni-foil in ambient pressure CVD reactors. Under these conditions the Ni-foil are likely saturated and the challenge in controlling the number of graphene layers stems from the difficult-to-control kinetic processes of carbon precipitation during sample cooling.

These days, most fundamental surface science studies of graphene/metal interfaces are performed by exposure of clean single crystals to hydrocarbons inside the UHV chamber. These low pressure conditions lead to mainly monolayer graphene formation for most systems including Ni. One may distinguish between two growth procedures: (i) segregation growth, where carbon is dissolved in the bulk at high temperatures and segregates to the surface at lower temperatures, or (ii) surface growth, where carbon remains at the surface after de-hydrogenation of hydrocarbons and aggregates at the surface to form graphene. In the latter process the self-terminating growth at a single monolayer can be easily pictured, because for most hydrocarbons the metal acts as a catalyst for dehydrogenation and thus as the source of carbon. Once the surface is covered with graphene no more active sites are available and carbon production ceases. Single layer formation of graphene by the segregation method, on the other hand, is likely due to the lowering of the surface energy of the metal by covering it with graphene, i.e. it is related to wetting of a surface by a lower-energy material. In this case, the lowering of the free energy of the systems provides the driving force for monolayer graphene formation. Further carbon precipitation, i.e. formation of multilayer graphene, does not lower the free energy further and therefore the driving force for carbon diffusion to the surface is diminished. This scenario also explains why monolayer formation can be easily accomplished while formation of a controlled number of graphene sheets is difficult. While the monolayer lowers the free energy and thus is thermodynamically favored the energy difference between different numbers of graphene layers is negligible and thus there is no thermodynamic mechanism that would control graphene with a defined number of layers.

2.1. Structure of graphene–metal interfaces

There exist a large number of surface science studies of graphene on different transition metals. Wintterlin and Bocquet [33] reviewed these studies up to summer 2008 and earlier reviews for graphene/metal interfaces were published in 1997 [34,35].

The basic adsorption structures of graphene on metals are shown in Fig. 1. In this article we use a nomenclature where the adsorption structure is labeled by the sites of the carbon atoms with respect to the underlying metal surface, i.e. 'fcc-site' ('hcp-site') corresponds to structures with carbon atoms resting on top of the fcc-hollow (hcp-hollow) site of the substrate and other carbon atoms on atop sites. In the literature one sometimes also encounters a nomenclature that labels adsorption sites with respect to the center of the carbon-ring, i.e. in that nomenclature Fig. 1(a) would be labeled 'atop', (b) 'hcp', and (c) 'fcc'. However, only on Ni and possibly on Co a good lattice match between

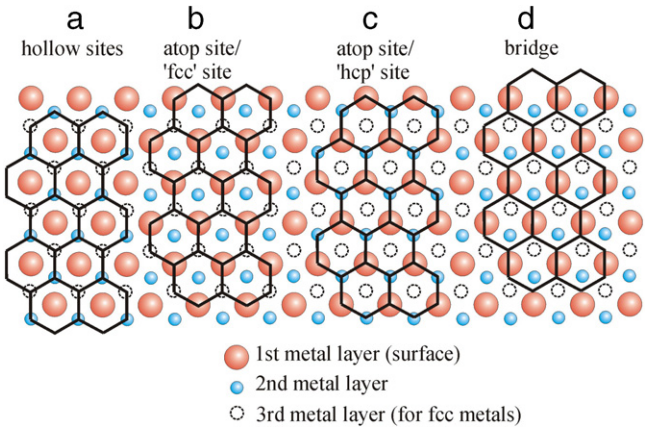

Fig. 1. Four basic adsorption arrangements for non-rotated graphene on hexagonal (fcc(111) or hcp(0001)) metal surfaces. (a) All carbon atoms of the graphene are located in three-fold hollow sites of the surface, i.e. the carbon-atoms surround the surface metal-atom. (b) Carbon atoms are alternately occupying metal-atop sites and the 'fcc' hollow sites. (c) Carbon atoms are alternately occupying metal-atop sites and the 'hcp' hollow sites. (d) Illustrates the adsorption structure that is known as bridge-structure. Here we use the nomenclature that labels the adsorption sites by the position of the carbon atoms with the respect to the substrate. Another sometimes used nomenclature labels the adsorption sites by the position of the center of the carbon relative to the substrate. In this second alternative nomenclature (a) would be labeled 'atop', (b) 'hcp', (c) 'fcc', and (d) 'bridge' adsorption.

graphene and the metal substrate exist, which allows the graphene to adopt (at least within large domains) a single adsorption structure. For lattice mismatched systems the lattice of graphene and that of the substrate are incommensurate and therefore periodic repetitions of certain adsorption structures give rise to a moiré pattern. Within the unit-cell of the moiré structure the different 'basic' adsorptions structures are locally observed. As we discuss below the binding of graphene to the substrate may depend strongly on the carbon arrangement relative to the substrate and this can give rise to a strong buckling of the graphene as the relative lattice positions within the moiré pattern changes.

In the following, we give a summary of recent (~2000–2011) studies of graphene/metal interfaces sorted by substrate material.

2.1.1. Ruthenium(0001)

Most studies report a single rotational domain of graphene grown on Ru(0001) with the ⟨10–10⟩ direction of graphene and Ru aligning parallel, i.e. no rotation of the graphene lattice relative to the Ru lattice. The moiré pattern of graphene is apparent from 'extra' diffraction spots around the 1 × 1 spots in LEED (see Fig. 2(a)). STM images also show the moiré pattern with a large 'apparent' corrugation [36], as shown in Fig. 2(c). The origin of the observed corrugation in STM images is somewhat controversial. Miranda and co-workers explain the corrugation in STM by mainly electronic effects and propose that the geometrical corrugation is only 0.15 Å [37] based on helium atom scattering (HAS) data. They also claim a change in the corrugation of the moiré pattern in STM images from 1.1 to 0.5 Å with a change in the bias voltage from −0.8 to 0.8 V [38] and that at high bias voltages (+2.6 eV) even an inversion of the contrast in STM images is observed. Wintterlin and co-workers, on the other hand, explain the corrugation mainly as a consequence of geometrical arrangement of carbon atoms backed by LEED I(V) and density functional theory (DFT) calculations (see Fig. 2(b) and (d)) [39,40]. LEED I(V) [41] and surface X-ray diffraction [42] measurements point to a significant corrugation of 1.5 Å. Recent re-analysis of the surface X-ray diffraction data reduced this value to 0.82 ± 0.15 Å [43]. In addition to a large corrugation of the graphene, the diffraction studies also showed that the underlying Ru is significantly distorted. LEED I(V) found

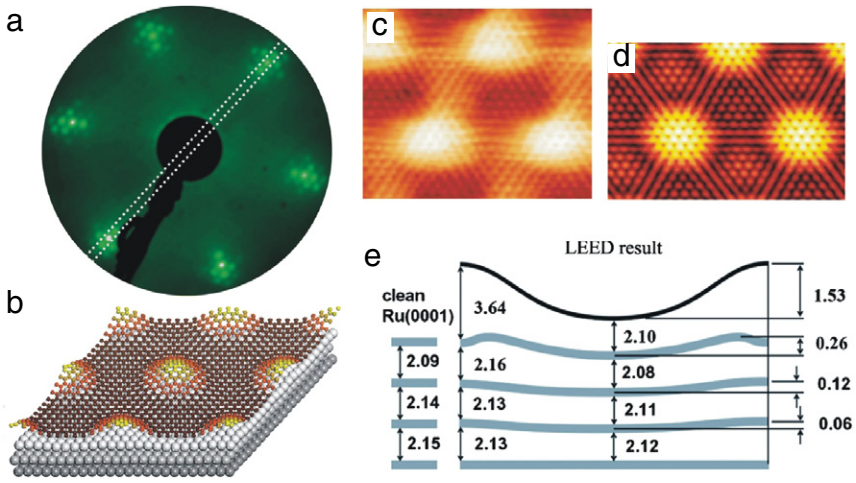

Fig. 2. Graphene on Ru(0001). (a) LEED pattern at 112 eV showing single domain graphene with superstructure spots due to moiré pattern. (b) 3D surface structure model. (c) Experimental STM image acquired at −0.05 V bias voltage and 1 nA tunnel current. (d) Simulated STM image, and (e) structure of graphene and Ru-surface layers derived from LEED I(V) analysis.
Source: (a), (b), and (e) reproduced from Ref. [41].

Source: (c) and (d) reproduced from Ref. [39].

a corrugation of the first Ru-layer of 0.23 Å in good agreement with the surface X-ray diffraction data that indicate a corrugation of 0.19 ± 0.02 Å. Due to the strong corrugation of both the substrate and the graphene sheet, the separation between the graphene and the metal also strongly varies across the unit cell. Values varying between 2.1 Å and 3.64 Å have been found in LEED I(V) studies and 2.0 Å and ∼3 Å in surface X-ray diffraction (SXRD) [43]. A schematic view of the corrugations of surface and sub-surface layers derived from LEED I(V) is shown in Fig. 2(e).

The recent LEED I(V) and SXRD studies indicated a size of the coincidence lattice of the graphene overlayer on Ru(0001) as a 23 × 23 superstructure with 25 × 25 graphene unit cells lying on top of 23 × 23 Ru surface unit cells. This is larger than the 11 × 11 or 10 × 10 superstructure suggested earlier from STM measurements [36,44,45]. DFT calculations showed that carbon atoms within this unit cell located on top of Ru-atoms interact strongly with the substrate, while C-atoms in-between Ru-atoms interact much weaker with the substrate, as measured by charge re-distribution. These differences in the interaction with the substrate also give rise to the strong corrugation of the graphene sheet. 'Non-bonding' areas of the graphene sheet, with carbon atoms mostly at in-between sites, alternate with 'bonding areas' where every second carbon atom is located close to an atop site and the other carbon atoms occupy three-fold hollow sites of the substrate (see Fig. 1). The difference in the location of the carbon atoms in the 'bonding' areas is the reason why, in STM, only every second carbon atom is imaged while in the 'non-bonding' area all carbon atoms are imaged (see Fig. 2(c) and (d)). The different charge transfer between Ru and graphene in the different areas of the moiré-pattern may also explain the observed splitting of the C1s core level in synchrotron radiation based high resolution X-ray photoemission spectroscopy (XPS) [46].

A strong interaction between graphene and ruthenium substrate is also apparent from electronic structure measurements. ARPES showed a strong disruption of the graphene π-bands [47] and a shift of 2.6 eV to higher binding energy [48] at the K-point compared to free-standing graphene. This can be attributed to the hybridization between the graphene π and the Ru 4d valence band states. The structural changes in the Ru-substrate also indicate a strong interaction between Ru and graphene. The strong effect of the substrate on the electronic structure of graphene is almost completely diminished for a second graphene layer on Ru [47,49].

2.1.2. Iridium(111)

Graphene has been grown on Ir(111) by hydrocarbon decomposition. Because of low carbon solubility in iridium the graphene growth is self-limiting to one monolayer [50,51], i.e. once the surface is covered by graphene the surface is deactivated for hydrocarbon decomposition effectively shutting down the carbon source. However, under certain conditions bi-layer growth of graphene can also be obtained on Ir(111), indicating that carbon segregation from the bulk cannot be entirely neglected [52]. Several domains with specific rotation angles with respect to the metal substrate have been observed. The preferred orientation appears to be an alignment of rows of densely packed carbon atoms with the densely packed rows of the Ir(111) surface [50,53,54], those graphene domains are referred to as R0°. Domains with rotational angles of R30°, R18.5°, and R14° have also been observed in LEEM studies [54]. In addition, domains with small angle rotation around the ideal R0° have been observed in STM, giving rise to small angle tilt boundaries in graphene [51]. The rotational alignment of graphene sheets appears to be dependent on the preparation temperatures. High resolution (spot profile) LEED has been used to characterize the graphene rotation at different growth temperatures [55]. It was found that below 1200 K the graphene layer exhibits high disorder. Temperatures between 1255 and 1400 K produced randomly oriented domains, with a preference of R30° domains. At temperatures above 1500 K a single R0° domain has been obtained, thus demonstrating a preparation method for single domain graphene on Ir(111). Because of the lattice mismatch between graphene and the Ir(111) surface, the graphene sheets form an incommensurate phase that exhibits moiré patterns. Similar to Ru, the moiré-structure is a consequence of carbon atoms occupying different sites on the Ir(111) surface; models of different rotational domains may be found in Refs. [50,54]. The geometric structure of the graphene-moiré on Ir is less well characterized than that on Ru and in particular, no LEED I(V) or SXRD studies have been reported as of yet. In STM the moiré structure shows a corrugated profile. For the R0° domain, STM images could differentiate the three basic adsorption structures shown in Fig. 1(a)–(c). The contrast in STM may depend sensitively on the tunneling conditions and even contrast reversal has been observed by changing the bias voltage from 0.32 to 1.5 V. In general the measured corrugation in STM is around ∼0.3 Å, i.e. 5 times less strong than for Ru.

For an R30° domain structure, an even smaller corrugation of only 0.04 Å was measured [54].

The electronic structure of graphene on Ir was measured by ARPES. For the R0° structure it was found that the Dirac cone is almost intact and only slightly shifted to lower binding energy due to a substrate induced p-type doping of graphene [56]. Downward shifting of the bands by n-doping of the graphene with potassium allowed determining the existence of a small band gap (∼100 meV) at the Dirac point [57]. This is in contrast to R30° rotated graphene domains that do not exhibit a band gap at the Dirac point, although its p-type doping by the substrate is stronger than for R0° domains. Thus ARPES show that for graphene on Ir, the π bands are not significantly perturbed. However, the interaction of graphene with Ir(111) depends sensitively on the orientation of the graphene sheet. It has been shown by DFT calculations that the interaction between graphene and Ir(111) is best described as physisorbed with only local charge accumulation between graphene and Ir at certain areas within the large moiré-supercell, where the interaction can be described as a weak chemisorption state [58]. The R0° domain may exhibit more of the weak chemisorption contribution and thus explain the observed small band-gap resulting from this hybridization of the carbon with Ir-states near the Fermi-level, while the R30° has less of the chemisorption contribution to its bonding to the substrate. This difference between the domains may also explain why Raman active phonons are observed on R30° but are suppressed on R0° domains [57]. The differences in the bonding for these two domains may also contribute to the above mentioned difference in the corrugation of the moiré-pattern observed in STM. Finally, band structure replicas due to the moiré-superstructure are observed in ARPES for the R0° domains [56] but not for the R30° domains [57] indicating that the observation of these replicas correlates with the strength of the graphene–substrate interaction.

2.1.3. Platinum(111)

Graphene on platinum can be grown by carbon segregation from the bulk or by a self-limiting decomposition of hydrocarbons at the surface. The interaction between monolayer graphene and the metal substrate is weak causing the formation of many rotational domains. LEEM studies have identified a number of domains with small $\{(3 \times 3)_G$, $(\sqrt{6} \times \sqrt{6})R2_G$, and $(2 \times 2)R4_G\}$ or large unit cells $\{(\sqrt{44} \times \sqrt{44})R15_G$, $(\sqrt{52} \times \sqrt{52})R14_G$ and $(8 \times 8)_G\}$ [59]. To explain the multitude of different rotation-angles between graphene and Pt(111) a simple geometrical model has been proposed [60]. In this model the mismatch of the moiré-superstructure unit cell with respect to Pt atoms are considered. Moiré structures with rotation angles that result in a small mismatch are considered more favorable and thus expected to occur more frequently. This simple model appears to be in satisfying agreement with experimental observations. Furthermore, a faster growth of domains with a smaller unit cell was observed compared to domains with large unit cells in growth experiments by carbon segregation [59]. Graphene films grown by direct decomposition of ethylene at different temperatures showed the best quality at growth temperatures around 800 K [61]. This optimum growth temperature was associated with a sparse nucleation of graphene at this temperature. Comparison of specular beam LEED I(V) measurements with simulated I(V) spectra on $(\sqrt{44} \times \sqrt{44})R15_G$ domains showed the best Pendry R-factor for Pt–graphene separation of 3.3 Å [59]. This is similar to the plane separation in graphite of 3.36 Å and is in excellent agreement with DFT simulations for graphene on Pt(111) [62]. Micro ARPES on different graphene domains showed that the band structure of graphene is very similar to free-standing graphene, with well defined linear π band dispersion at the K-point. The graphene monolayer was, however, p-doped with the Dirac point about 0.3 eV above the Fermi-level [59] again in good agreement with DFT calculations [61,62]. Consequently, by all indicators – graphene–Pt separation, electronic structure, and formation of various rotational domains – the interaction between graphene and Pt is weak.

2.1.4. Palladium(111)

LEEM studies of graphene formed by carbon segregation from carbon saturated Pd(111) single crystals show many rotational domains. Rotational angles between the Pd [63] and graphene [11–20] direction of −2°, −5°, −10°, 17°, 22°, and 26° were observed [64]. This situation of several rotational domains is similar to the observations on Pt and thus may suggest a weak interaction between graphene and palladium. However, scanning tunneling spectroscopy (STS) measurements of graphene on Pd suggest the existence of a 0.3 eV band gap in Pd supported graphene [65]. The existence of such a band gap would indicate a strong hybridization between graphene and Pd. However, it should be pointed out that STS measurements are not as conclusive as photoemission measurements and therefore the existence of a band gap should be confirmed by other techniques. STM measurements show a corrugation of the moiré pattern of ∼0.2 Å and a reversal of the contrast has been observed by reversing the bias voltage [65]. Relative work function measurements of different rotational domains using image contrast in LEEM, reveal that the work function for different domains can vary by up to 0.15 eV. This was interpreted as an orientation dependent charge transfer [64].

2.1.5. Rhenium(0001)

A strong interaction between Re and graphene is proposed. LEEM studies show the formation of a single domain and μ-LEED analysis indicate a 10×10 graphene unit cell over a 9×9 Re(0001) unit cell. DFT calculations show that the resulting moiré structure should be strongly corrugated with a buckling of 1.6 Å. The C–Re distances depend on the position in the moiré structure and are mainly distributed between 2.1 and 2.4 Å, but can be as large as 3.8 Å as a consequence of the large buckling of the graphene sheet. The different areas of interactions within the moiré unit cell also give rise to differences in the C 1s core level peak position. Two main components for the C 1s peak for graphene on Re are observed. The two components are separated by ∼700 meV. The higher binding energy component is due to stronger interacting carbon atoms that are closer to the Re surface [66].

2.1.6. Rhodium(111)

Graphene on Rh(111) forms a single domain with a moiré pattern that corresponds to a coincidence lattice with a 12×12 graphene cell matching a 11×11 Rh surface cell [46,67]. Like on Ru the different adsorption sites of carbon atoms within the 11×11 superstructure gives rise to different bonding which causes a strongly corrugated graphene sheet. The weakest adsorption is in regions where the carbon-hexagon surrounds the surface metal atoms (Fig. 1(a)) and those regions show the largest carbon–Rh separation of ∼3.8 Å according to DFT simulations. Regions with alternating carbon atoms in hollow sites and on atop sites (Fig. 1(b) and (c)) have a graphene–Rh separation of 3.1 Å and 2.9 Å depending if the fcc or hcp hollow sites are occupied, respectively. The strongest adsorption was found in regions where carbon atoms occupy bridge sites (Fig. 1(d)). In these regions a carbon–Rh distance of 2.2 Å was found. These DFT simulations are in agreement with STM measurements, suggesting that at low bias voltages the STM measurements are dominated by topographic surface features. Thus the DFT and STM measurements suggest a buckling of the graphene sheet by 1.6 Å, similar to that for graphene

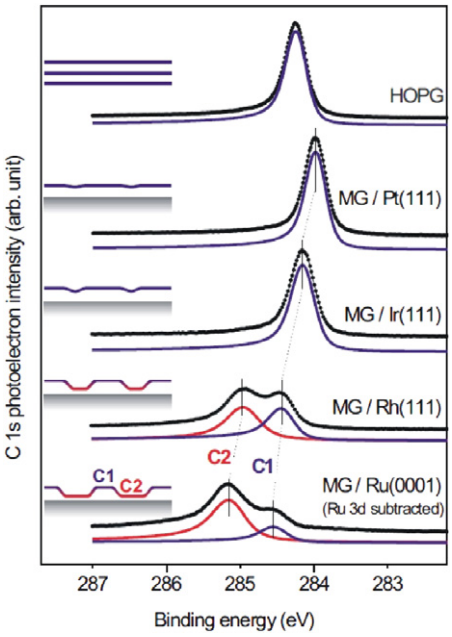

Fig. 3. C-1s core level binding energies of monolayer graphene on various metal substrates acquired with 400 eV photon energy. For graphene that exhibit a strongly corrugated graphene moiré-pattern two binding energy peaks are observed corresponding to the strongly and weakly interacting areas within the moiré-unit cell. With increasing metal–graphene interaction a shift toward higher binding energy is measured.
Source: Reproduced from Ref. [46].

on Ru. C-1s XPS and near edge X-ray absorption fine structure (NEXAFS) measurements also suggest similar graphene–metal interactions for Ru and Rh, with both showing clearly two C-1s core-level components due to areas within the moiré pattern that are strongly and weakly interacting with the substrate [46]. A comparison of the C-1s binding energies for graphene on various metal substrates is shown in Fig. 3.

2.1.7. Nickel(111)

As outlined in the introduction, graphene formation on Ni(111) was studied early on. The close lattice match between graphene and Ni allows the growth of commensurate graphene overlayer on Ni(111) with no superstructure spots in LEED and this makes nickel a unique substrate material for graphene/metal interface. LEED I(V) studies identified the adsorption structure of graphene with one carbon atom atop of Ni-surface atom and the second carbon at fcc-hollow sites (Fig. 1(b)). The graphene–Ni separation was measured as 2.11 and 2.16 Å for carbon atoms at fcc-hollow and atop carbon sites respectively [68]. This surface structure has been supported by Li^+-impact collision ion scattering spectroscopy (ICISS) [69] and DFT simulations [70]. Most DFT calculations show the adsorption of graphene with carbon atoms at atop and fcc-hollow sites as preferred, however, adsorption of the second carbon atom over hcp-hollow sites (Fig. 1(c)) instead of the fcc-hollow site is only slightly less favorable. This indicates the possibility that under certain growth conditions both adsorption geometries are present in different domains. The domain boundaries resulting from such two, relative to the Ni-substrate, translated domains have been observed in STM and are discussed in Section 4.4 [71]. In STM of graphene on Ni, the two non-equivalent carbon atoms are imaged with different contrast [72]. From imaging of translational domain boundaries it is shown that the carbon atoms above the hollow sites are imaged brighter. This is in agreement with DFT simulations of STM images. From STM measurements it is also apparent that under certain circumstances rotated graphene can form that exhibits moiré-patterns [72,73]. This is discussed further in Section 2.2.3. Two recent DFT calculations claim that a different adsorption geometry, i.e. with carbon occupying bridge sites (Fig. 1(d)), is another possible arrangement in addition to carbon-atoms occupying both 3-fold hollow and atop sites [74,75]. The only experimental evidence for such an adsorption structure comes from the interpretation of two different components in C-1s core level peak as the presence of domains with both bridge and top-fcc hollow configurations. It has been argued that carbon atoms at atop, hollow, and bridge sites have C 1s binding energies of ~285.04 eV, 284.46 eV, and 284.88 eV, respectively. However, additional experimental evidence would be desirable to confirm such bridge adsorption geometry. For example, since all the carbon atoms in bridge adsorption geometry are equivalent no difference between the carbon atoms in atomic resolution STM imaging is expected. Therefore STM images with such a contrast would be an additional test for the existence of such a bridge adsorption structure.

Several ARPES studies of the electronic structure of graphene on Ni have been performed. They all show a large down-ward shift of the π states by about 2 eV [76–78] and opening of a band gap at the K-point indicating a strong interaction between Ni and graphene (see e.g. Fig. 4 for comparison of ARPES of graphene on Ni(111) and formation of quasi-free-standing graphene after Au-intercalation). Dedkov et al. reported a large shift of up to 225 meV in the graphene π-band depending on the magnetization of the Ni-substrate [77]. This was interpreted as a signature of spin-polarized electrons in the π-band due to a Rashba-type spin–orbit interaction. However, subsequent work using spin polarized photoemission [79] and ab initio calculations [80] demonstrated that such spin-polarization of the π-band on Ni substrates does not exist.

2.1.8. Cobalt(0001)

The Co(0001) surface exhibits only a slightly larger lattice mismatch relative to graphene than Ni(111) does {$a_{graphene}$ = 2.46 Å; a_{Ni} = 2.48 Å; a_{Co} = 2.51 Å}. STM studies of nanometer sized graphene islands suggest that graphene is commensurate with the Co(0001) substrate, similar to Ni(111). Both STM and DFT-simulations [81] indicate that the honeycomb is situated such that the carbon atoms in the honeycomb alternately occupy atop and three-fold hollow sites of the Co-substrate (see Fig. 1(b) and (c)). This non-equivalence of adjacent carbon atoms is, like for Ni(111), also apparent in STM images, which only 'sees' every second carbon atom. The measurements and DFT calculation could not identify if the fcc- or hcp-hollow sites are preferred as carbon adsorption sites. Scanning tunneling spectroscopy (STS) and DFT calculation indicate a strong alteration of the electronic structure of graphene compared to free-standing graphene. Also the calculated Co–graphene distance of ~2.07 Å indicates a strong interaction of graphene π-states with the Co d-states [81]. All these findings suggest that Co and Ni behave similarly when it comes to interacting with graphene.

2.1.9. Copper(111)

Formation of graphene on Cu has become of great interest since it has been shown that single layer graphene can be readily formed in ambient pressure CVD processes [2,31,82]. Copper has low carbon solubility and thus even at high temperatures graphene forms at the surface with negligible carbon dissolution into the bulk. This enables a self-terminating monolayer growth unlike e.g. on Ni where growth proceeds by carbon segregation from the bulk [83]. Growth of graphene on Cu(111) in a UHV chamber succeeded by exposure of higher than 10^{-5} Torr ethylene and cycling the sample temperature up to 1000 °C (i.e. close to

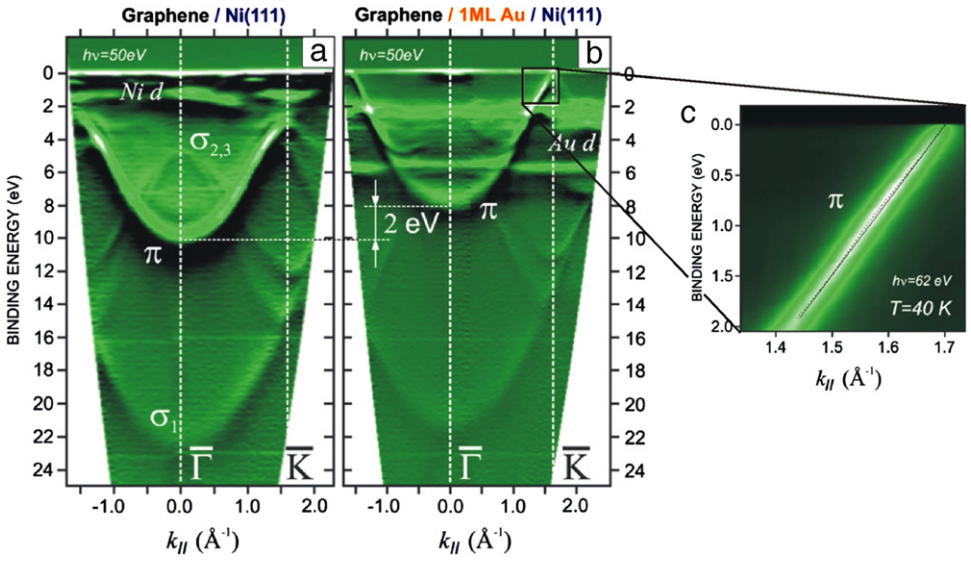

Fig. 4. ARPES measurement of graphene grown on Ni(111)(a) and after intercalation of a monolayer of Au (b). The linear band dispersion at the Dirac point after Au-intercalation is highlighted in (c). For graphene on Ni the π band is downshifted by ~2 eV. Intercalation of Au decouples graphene from the Ni-substrate and forms electronically quasi-freestanding graphene.
Source: Reproduced from Ref. [78].

the melting temperature of copper) [84]. This growth procedure resulted in the formation of at least two predominant domain orientations as judged from STM images. The observed moiré patterns of the supported graphene were associated with 0° and 7° rotation. The formation of multiple domains implies the formation of grain boundaries which necessarily have degrading effects on the graphene quality. Recent advances in CVD growth have, however, demonstrated that low nucleation density can result in large single grain graphene islands on polycrystalline Cu-foil (single-grains up to 0.5 mm in diameter has been achieved) [85]. STM studies of graphene grown on polycrystalline Cu-foil also shows that the graphene sheet can grow over facets and substrate grain boundaries to contiguously cover the substrate [86,87]. Detailed experimental information of the interaction of graphene with Cu, i.e. Cu–graphene separation and electronic structure of graphene on bulk copper has not yet been reported. However, studies of Cu-intercalation on graphene/Ni(111) (discussed next) indicate that the graphene electronic structure on Cu closely resembles that of free standing graphene.

2.1.10. Intercalated Au, Ag, Cu, and Fe

Graphene may not be easily synthesized on some metals, especially in UHV. These metals include Cu, Ag, Au, and Fe. It should be mentioned, though, that recent advances in growing graphene with ambient pressure CVD processes or by direct deposit of carbon at the surface has demonstrated the ability to directly grow graphene on Cu (see previous section) and even on gold foils at ambient pressures by a CVD process [88]. Due to the weak interaction between the metals and the graphene, the graphene directly grown on these metals are, however, polycrystalline in nature, even if single crystal substrates are used. To determine, for example, the electronic structure of graphene supported on different metals by ARPES single crystalline graphene is required. The solution for studying single crystalline graphene on different metal substrates is to grow graphene first on a strongly interacting metal substrate, such as Ni or Ru, and subsequently intercalate the metal of choice in between the metal substrate and graphene. This approach has been demonstrated for Au [47], Pt, Pd, Ni, Co, In, and Ce [89] between graphene grown on Ru and for noble metals (Cu [90], Ag [91], Au [78,92]), as well as Fe [93] and alkali elements (Na, K, Cs) [76] for graphene grown on Ni. Noble metal intercalation showed a decoupling of graphene from the substrate and the formation of quasi-free-standing graphene as judged from the band structure in ARPES [78] shown in Fig. 4. The intercalation process by itself is not well explained. The energy for distorting the graphene hexagon for a metal atom in order to diffuse through a defect-free graphene sheet is prohibitively high and therefore the intercalation has to occur at defects in the graphene sheet. These may be pre-existing defects or defects that are formed if the graphene sheet is sandwiched between two metals. For graphene on Ni(111) the intercalation process of deposited Ni was studied by AES and carbon monoxide adsorption–desorption studies [94]. In these studies it was found that the deposited Ni destroys the graphene locally, forming a surface-carbide which allows Ni at the surface to penetrate the graphene and merge with the substrate. After all the Ni has merged with the substrate the graphene can reform at the surface. A similar formation of an intermediate carbide could, however, not be observed for Cu intercalation [70] and thus the intercalation process may be different for different metals and therefore is still not completely explained.

2.1.11. Metal carbides

Many of the early transition metals are carbide forming and this may prevent the formation of graphene on the pure metal. However, studies have shown that graphitic layers can form on top of carbide–substrates formed from early transition metals. This field of research has not yet been revived by the recent interest in graphene and therefore most surface science studies on graphene/carbide interfaces are from the 1990s. Graphene was grown on WC(0001) [95] as well as on carbides with rock salt-structure {TaC(111) and (001), TiC(111) and (001), and HfC(111) and (001)} by exposure to ethylene in UHV [96–98]. Formation of graphene on the (111) surfaces is reported to be easier (lower ethylene exposure needed) than for the (001) surfaces. LEED studies have shown the formation of two graphene domains on TaC(111) and HfC(111) with $\langle 10\text{–}10\rangle_{\text{graphene}} \parallel \langle 1\text{–}10\rangle_{\text{carbide}}$ and $\langle 11\text{–}20\rangle_{\text{graphene}} \parallel \langle 1\text{–}10\rangle_{\text{carbide}}$ crystallographic relationships while for TiC(111) only the first domain structure was observed. Measurement of the phonon structure by EELS of the carbide supported graphene indicated a significant softening of the phonon

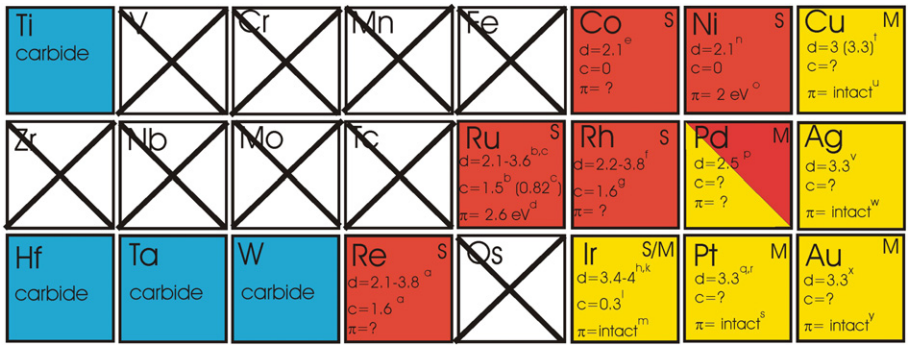

Ti	TiC: [96, 97, 98]
Hf	HfC: [96, 97, 98]
Ta	TaC: [96, 97, 98]
W	WC: [95]
Re	(a) DFT [66]
Ru	(b) LEED I(V) [41] (c) SXRD [43] (d)ARPES [48]
Co	(e) DFT + STM [81]
Rh	(f) DFT [67] (g) STM +DFT[67]
Ir	(h) 3.8-4 Å DFT for moiré structure [101], 3.44 Å DFT [265], (k) 3.38 x-ray standing wave [58] (l) STM[54] (m) ARPES [57]
Ni	(n) LEED I(V)[19] (o) ARPES [76, 77, 78]
Pd	(p) DFT [100]
Pt	(q) LEED I(V)[59] (r) DFT [265, 100, 62, 266] (s) ARPES [57]
Cu	(t) 3 Å DFT[265], 3.2 Å DFT [266], 3.3 Å [62] (u) ARPES [92]
Ag	(v) DFT [62, 265, 266] (w) ARPES [92]
Au	(x) DFT [62, 265, 266] (y)ARPES [92, 99]

Fig. 5. Summary of the interactions between transition metals and graphene. For the elements labeled in blue, graphene may grow on the bulk-carbides of these elements. Elements in red are characterized as metals that interact strongly with graphene and elements in yellow are those that interact weakly. '*S*' or '*M*' in the upper right corner of each element-box indicates if graphene forms single or multiple rotational domains, '*d*' is the reported graphene–metal separation in Å. Different values may indicate the range of separations within the moiré super-structures. The buckling or corrugation of the graphene sheet is given by '*c*' in Å, and the amount of downward shift of the π-band is given by 'π' ('Intact', means that a linear dispersion at the Dirac point is still observed). The measurement methods or computation for deriving the values are given in the table together with the appropriate reference (see also references [265,266]). (For interpretation of the references to colour in this figure legend, the reader is referred to the web version of this article.)

modes, which was interpreted by a softening of the π bonds due to charge transfer from the substrate.

2.1.12. Summary and comparison of graphene/transition metal interfaces

The formation of graphene and its interaction with different substrate metals can be divided into three categories as indicated by the differently colored elements in Fig. 5. Early transition elements are carbide forming and graphene monolayers have been formed on the carbides of these elements but not on the pure metals. For graphene on pure metals, we can differentiate between strong and weak interacting elements. Characteristics of a metal that interacts strongly with graphene are: (i) formation of a single domain structure if grown by CVD or carbon deposition on the substrate, (ii) a strong alteration of the graphene π-band, in particular a shift to higher binding energy of 1–3 eV and opening of a band gap, (iii) the smallest distance between the metal and graphene is around 2.1–2.2 Å, i.e. much smaller than the graphene-plane separation in graphite. This is clearly observed for Ni and Co. For these elements, graphene is well lattice matched and graphene can adsorb in a single adsorption geometry, i.e. the honeycomb lattice has the same registry with the metal substrate atoms across the surface. (iv) If a moiré-pattern is formed, a large corrugation of the graphene layer with a buckling of more than 1 Å is observed. The moiré-pattern is a consequence of the lattice-mismatch between graphene and the substrate which forces carbon atoms in the graphene sheet to occupy various adsorption sites on the metal substrate. The large corrugation in strongly interacting metals indicates large variations in the carbon–metal interaction depending on the position of the carbon atoms relative to the metal atoms. For all elements the weakest interaction is found if the carbon-hexagon is centered over the surface metal atoms (Fig. 1(a)), i.e. all carbon atoms are over the three-fold hollow sites of the substrate. Such a configuration gives rise to the largest separation between the metal and the graphene, around 3.6–3.8 Å for Re, Ru, and Rh. For Ru and Re it is found that graphene with one carbon-atom at atop sites and the other in three-fold hollow (Fig. 1(b) and (c)) forms the strongest adsorption while for Rh, a bridge adsorption geometry (Fig. 1(d)) is proposed to give the strongest interaction. The metal–graphene separation in the areas of strong interaction is around 2.1 Å, i.e. similar to the separation on Ni(111). The different areas within the moiré pattern that exhibit different bonding to the substrate also gives rise to slight variation of chemical shifts in C-1s core levels. Fig. 3 shows a comparison of high resolution C-1s peaks for Ru, Rh, Ir and Pt substrates. A clear shift to higher binding energy is observed with increasing graphene–metal interaction and two components are resolved for Rh and Ru due to the moiré-structure [46]. Similar two components are also observed for graphene on Re [66].

Weakly interacting metals are colored yellow in Fig. 5. The characteristic of weakly interacting graphene is a graphene–metal separation of ~3.3 Å, i.e. a similar separation as observed for graphene layers in HOPG, and an almost undisturbed π-band with the Dirac cone at the *K*-point intact. However, some p- or n-type doping of the graphene can shift the Fermi-level below or above the Dirac point. This shift in the Fermi-level may be as much as 0.5 eV.

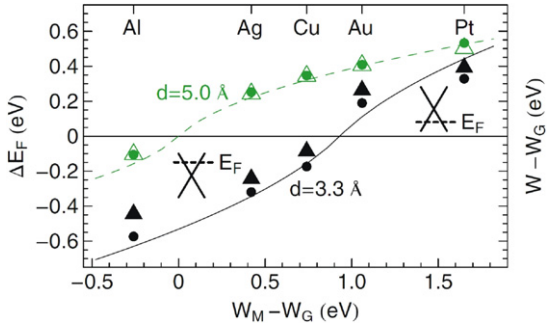

Fig. 6. Calculated Fermi-energy shift, ΔE_F, relative to the conical point for graphene in contact with different (weakly interacting) metals. The Fermi-energy shift is plotted as a function of the difference in the work function of the metal and graphene, $W_M - W_G$. The black curve is for an equilibrium separation between graphene and the metal of 3.3 Å, while the green curve is for a hypothetically larger separation of 5.0 Å. At 5.0 Å separation, there would be negligible interactions between graphene and the substrate and the crossover from n- to p-type doping would occur at $W_M = W_G$. An equilibrium separation of 3.3 Å results in a crossover shifted toward a higher metal work functions by ∼0.9 eV. (For interpretation of the references to colour in this figure legend, the reader is referred to the web version of this article.)
Source: Reproduced from Ref. [62].

This shift is due to charge transfer processes as a consequence of differences in the work function of the metal and graphene and is *not* related to any hybridization and chemical bonding. The crossover from p- to n-type doping occurs at a metal work function of ∼5.4 eV, which is larger than the work function of graphene of 4.5 eV [62]. The results of DFT computations are shown in Fig. 6. This doping effect through the metal contact is in good qualitative agreement with experiments. For example, with graphene on Pt a p-type doping with the Dirac point 0.3 eV above the Fermi-level was found experimentally [59] and for Au (intercalated in graphene/Ni(111) system) a shift of the Fermi-level 0.1 eV below the Dirac point was measured [99]. For Ag and Cu n-type doping was observed [92], however, the experiments were not accurate enough to give a precise number for the Fermi-level shift above the Dirac point.

We have marked Pd as intermediate between strong and weak interacting metals. This is primarily based on the DFT number for graphene–Pd separation of 2.5 Å. More data would be desirable to give more weight to the values for the graphene/Pd interface cited in Fig. 5 and substantiate its intermediate position. For Ir multiple domains are observed at low growth temperature, however, a single domain structure can be synthesized at high temperature. This may indicate that it is at the border between single and multiple domain formation. Some of the values available for the graphene–Ir separation seem quite large, i.e. larger than the separation expected for the weak interacting metals. This may be a consequence of the short-comings of DFT simulations in weak van der Waals interacting systems. In the particular case for graphene–Ir separation, the generalized gradient approximation (GGA) was used which is known to overestimate the distance for van der Waals interactions [100] and this may explain the unreasonably large value for the separation. More recent DFT calculations give a more reasonable value of 3.44 Å which is also in excellent agreement with experimental studies using a X-ray standing wave technique that indicate a mean separation of 3.38 ± 0.04 Å, which is very close to the interlayer separation of HOPG of 3.35 Å. Other properties, like the comparably small corrugation of the moiré pattern and the intact π-band and Dirac cones of graphene would also justify classifying iridium as a weakly interacting metal. Therefore Ir takes a special place in the sense that it is the only weakly interacting metal on which graphene can be grown in a single rotational domain structure.

The chemical reason for the different interactions between the different metals and graphene can be given by first approximations in the position of the d-bands of the metal surface below the Fermi level [101], since the d-band electrons are primarily responsible for the bonding with graphene. This can give some guidance in justifying the differences in the interaction. In Table 1 the position of the center of the d-band of the transition metal is compared to the values for the graphene–metal separation d given in Fig. 5. From this comparison one may reach an empirical categorization of the metals in: (i) metals with their d-band center less than ∼2 eV below the Fermi level as strongly interacting metals, and (ii) metals with their d-band center below ∼2 eV as weak interacting metals. However, the lattice-mismatch and ensuing moiré-pattern complicates the situation as the carbon atoms are forced away from the most stable adsorption configuration. Therefore more detailed electronic structure calculations are required to understand the bonding. Recent advances in DFT calculations of weak van der Waals systems and increasing computation power have shown to be capable of tackling even large moiré-structures quite successfully.

2.2. Graphene-growth on transition metals

In the quest of synthesizing high quality graphene by CVD processes over transition metal substrates, a lot of effort has been spent in trying to understand the fundamental growth processes involved in the formation of macroscopic graphene sheets. Most fundamental surface science studies on the growth of graphene have been reported for Ru, Ir and Ni. These studies are aided by the fact that graphene can be grown in UHV, i.e. by exposure to fairly low pressures of hydrocarbons. Different processes have been studied: (i) exposure to hydrocarbons at room temperature and subsequent decomposition by annealing in vacuum, (ii) exposure of the hot sample to hydrocarbons, and (iii) dissolving carbon into the bulk and growing graphene by carbon segregation during cooling. Recently some more interest was devoted to the growth of graphene on Cu with the main goal to increase the grain sizes of graphene. For growth of graphene on Cu by CVD processes usually higher pressures are needed than accessible in a UHV chamber and therefore graphene growth by hydrocarbon decomposition is difficult under UHV conditions [84]. However, direct deposition of carbon from a physical vapor source, i.e. a process similar to molecular beam epitaxy (MBE), enables one to study graphene growth on Cu under UHV conditions. In the following, we discuss the growth studies on these different metal substrates.

2.2.1. Ruthenium

Growth of graphene on Ruthenium has been most thoroughly studied. LEEM studies have given important new insights into the growth dynamics [103–106]. In these studies it was identified that atomic-step edges on graphene are overgrown by graphene (carpet growth), but only in the down-direction of the staircase of Ru-steps [103]. The graphene islands are attached to a step-up edge, indicating bonding of graphene to the step. During growth, carbon-atoms are being added to the 'free' island edge which can overgrow step down edges with little 'resistance'. Recent high temperature STM measurements of the growth of graphene at step edges have given a more detailed view of the interaction of the graphene-growth front with steps [107]. It has been shown that the growth front becomes rough when it crosses a step edge due to the graphene traversing the step only locally rather than the graphene growth front crossing the entire step simultaneously. At low hydrocarbon pressures or high temperatures a different growth was observed by high temperature STM. In this growth mode the graphene does not cross the step, but instead the underlying metal terrace grows together with the graphene, so that

Table 1
Comparison between d-band center of the transition metal surfaces and the reported values for graphene–metal separation (for strongly corrugated moiré-structures the area with the smallest separation was chosen as this represents the areas with strongest adsorption). From this comparison one may roughly separate into strongly interacting metals with a d-band center between the Fermi level and 2 eV binding energy and weak interacting metals with their d-band center at binding energies below 2 eV.

	Binding energy of d-band center relative to Fermi energy [102] (eV)	Graphene–metal separation (see also Fig. 5) (Å)
Co(0001)	−1.17	2.1
Ni(111)	−1.29	2.1
Cu(111)	−2.67	3.3
Ru(0001)	−1.41	2.1
Rh(111)	−1.73	2.2
Pd(111)	−1.83	2.5
Ag(111)	−4.30	3.3
Re(0001)	−0.51	2.1
Ir(111)	−2.11	3.4
Pt(111)	−2.25	3.3
Au(111)	−3.56	3.3

the graphene remains on the same atomic-plane. This necessarily requires ruthenium transport to increase the terrace size for the graphene to grow on. Formation of a single terrace for the graphene to grow on was observed in both uphill, i.e. the etching of steps, and downhill, i.e. the adding to Ru to steps. This process resulted in multiple step heights in both uphill and downhill direction at the edge of the graphene-covered terrace [107]. LEEM studies also showed a related growth mode that involved Ru step etching. In this growth, the graphene island grew at the step edge, which is attached to the graphene sheet. This is possible by removing Ru atoms from the step-up edge and simultaneously growing of the graphene sheet. No step-bunching like in the high temperature STM study was reported, however. It has been proposed that these Ru-atoms that are removed from the step edge diffuse underneath of the graphene sheet and nucleate Ru-islands or attach to other step edges. Some evidence for the formation of dislocation networks formed underneath of the graphene by these etched Ru-atoms has been shown in STM images [106].

The clearest insight on the growth kinetics comes from elegant studies of the 'carpet-growth mode' by McCarty and co-workers using the electron reflectivity in LEEM to give an accurate measure of the carbon ad-atom concentration at the metal surface [104,105]. Simultaneous measurement of the carbon ad-atom concentration and the growth rate of individual graphene islands allowed them to correlate growth rates with carbon concentration on the surface. Fig. 7(a) shows the variation of the carbon monomer concentration on the Ru-surface in a typical experiment. It was shown that the behavior of the carbon concentration is independent of the carbon source, i.e. atomic carbon deposition, ethylene decomposition at the surface, or carbon segregation from the bulk. In Fig. 7(a), the carbon concentration increases with increasing carbon deposition at the surface. Once a critical concentration is reached, graphene nucleates. This happens on Ru at a carbon concentration of ~0.035 ML. When graphene is nucleated the C-monomer concentration drops as an equilibrium is established between carbon-monomers consumed by the graphene islands and the carbon re-supplied to the surface from the carbon source. If the carbon source is shut off the carbon monomer concentration reaches another lower equilibrium which is the phase equilibrium concentration between graphene and a carbon monomer lattice-gas on the surface. On Ru, this equilibrium is around 0.017 ML of carbon at $T = 1020$ K. From an Arrhenius plot of the equilibrium carbon concentration at different temperatures, an enthalpy for carbon monomer formation of $E^f_{Ru} = 0.31$ eV has been derived [104]. Surprising was the finding that the graphene growth velocity did not increase linearly with the C-monomer concentration. Instead a non-linear behavior was obtained; this can be appreciated in Fig. 7(b). The growth velocity dependence on the carbon concentration can be fitted by:

$$v \sim \left[\left(\frac{C}{C_{eq}}\right)^n - 1\right] \quad (1)$$

with $n \approx 5$. This behavior is explained if not carbon monomers attach to the growing graphene front but instead graphene clusters are pre-formed in the carbon lattice-gas and these clusters then attach to the graphene. In this model n is the number of C atoms in the cluster that attach to the graphene edge. This model has given further justification by experimental findings of small carbon clusters on Rh-substrates, even though they were of 7 C_6 rings, i.e. 24 C atoms in size, rather than the 5 atoms expected from the growth model [63]. The experimentally found carbon concentration in LEEM was also verified by a simple rate theory of epitaxial growth of graphene [108]. Optimizing the barriers in the rate equations gave an excellent match to the experiment. The physical reason why carbon monomers do not attach directly to the graphene front may lie in the fact that carbon monomers are fairly strongly bound to the metal at hcp sites, 1.0 Å above the Ru surface atoms, whereas graphene is less strong bound to Ru(0001) (2.1–3.6 Å above the surface; see e.g. Fig. 5). Therefore, to attach a monomer to the graphene edge, it would need to break the carbon–metal bond, which involves a large barrier and thus makes this process unfavorable. Instead, intermediate carbon structures may form that involve both C–C as well as C–metal bonds. The formation of these intermediate structures may lower the kinetic barriers by bridging the spatial and energetic gap between C-monomers and graphene as illustrated schematically in Fig. 7(c) [104].

2.2.2. Iridium

LEEM studies, like the one described for Ru, have also been conducted for graphene growth on Ir [105]. It was found that the growth on Ir follows the same cluster attachment scenario. Small differences were found for the carbon-monomer concentration in equilibrium with graphene islands. On Ir, a lower carbon monomer concentration was found compared to Ru, indicating a higher formation enthalpy, which was estimated to $E^f_{Ir} = 0.4$ eV. Also, while on Ru the graphene islands were found to only grow down on the metal-step staircase, on Ir the steps do not impede its growth direction and graphene has been found to grow in both up and down step directions. This may indicate that graphene interacts less strongly with Ir-steps. This is in agreement with the overall weaker interaction of graphene with Ir compared to Ru. On Ir, different rotational domains may form and the graphene domain orientation has strong effect on their growth rate. Graphene

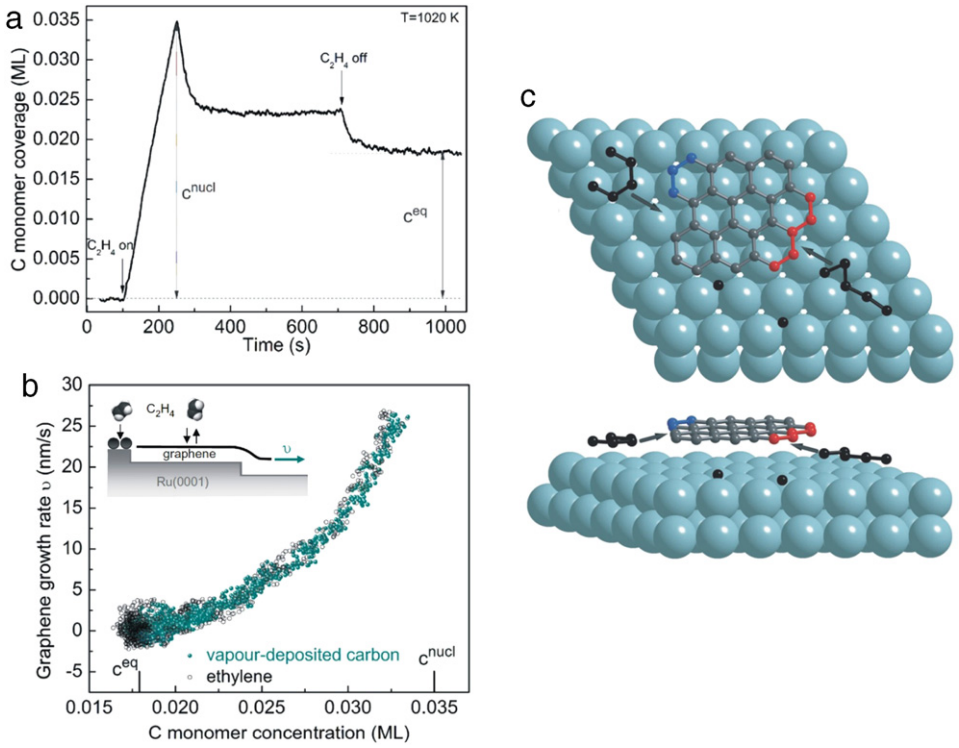

Fig. 7. Growth studies of graphene on Ru(0001) by LEEM. The measurement of carbon monomer concentration on Ru-substrates throughout a typical experiment is shown in (a). Initially, the monomer concentration increases until it reaches a graphene nucleation threshold, it then decreases to a stable steady-state reaction concentration. After shutting of the C_2H_4 valve the carbon-monomer concentration reaches an equilibrium with graphene. In (b) the growth rate of graphene (monitored by LEEM) is plotted as a function of the steady state C-monomer concentration. The clearly non-linear behavior is explained by a carbon cluster attachment mechanism that is illustrated schematically in (c).
Source: Reproduced from Refs. [104,105].

islands that nucleate later in the growth have been shown to adopt different rotation relative to the substrate. Surprisingly, these graphene islands have been found to grow much faster than the initially nucleated islands. This demonstrates that the edge orientation of the graphene relative to the substrate may play an important role in the carbon attachment to the graphene islands. In other studies it has been shown that the alignment of graphene with the substrate is temperature dependent [55] with single graphene orientations formed at high growth temperatures. The initial nucleation and growth of graphene on Ir was also investigated by STM [53]. Initial islands were shown to be primarily terminated by zigzag graphene edges and a preponderance of nucleation of graphene at Ir step edges was observed. In agreement with LEEM studies that show that graphene are not strongly bound to Ir-step edges, STM shows that the initially nucleated graphene islands lie across the step edges with no indication of graphene-edges terminating at Ir-steps. Initially formed small graphene clusters have been investigated in a combination of high resolution XPS and density functional calculations [109]. In these studies it was shown that the edges of graphene nanoislands interact strongly with the Ir-substrate while the interior of these small graphene islands act like quasi-free-standing graphene. These nanoislands may be graphitic precursor states to large area graphene formation. For extended graphene sheets grown at elevated temperatures and cooled to room-temperature formation of ridges within the graphene sheet are observed. These are regions where the graphene is locally delaminated from the Ir-substrate. These ridges form as a consequence of stress-relaxation induced by the different thermal expansion coefficients of the metal substrate and the graphene [110].

The formation of bilayer graphene by carbon segregation from the bulk as well as elemental carbon deposition was also investigated by LEEM on Ir(111) [52]. It was found that independent of the carbon source the second layer nucleates in between the graphene and the metal substrate. Also the second layer nucleated more readily for first layer rotational variants that are more weakly bond to the metal substrate. Nucleation occurred at substrate defects and the second layer graphene is not necessarily rotationally aligned with the first layer.

2.2.3. Nickel

LEEM studies of graphene growth by carbon segregation from the bulk on Ni(111) indicated a low nucleation density [111]. It was found that a second layer may nucleate and grow underneath the first layer upon its completion. The edges of the graphene islands were straight for the first layer-island, dendritic for second and straight again for the third layer again. This behavior was suggested to arise from a variation of the interfacial-bond strength of the graphene to the Ni substrate.

XPS studies of CVD graphene growth in UHV on a thin Ni(111) epitaxial film on W(110) substrates showed that graphene growth is self-terminating after completion of the first monolayer [112]. It is important to point out that these studies were performed at low hydrocarbon pressures (2×10^{-7} Torr propylene) and a clean metal, i.e. without significant amounts of carbon dissolved in the Ni crystal. Upon exposure to propylene a C-1s signal at 283 eV binding energy was observed and the graphene signal at ~284.7 eV binding energy started to grow after around 100s time delay. However, the 283 eV carbon peak was only observed for growth temperatures below 600 °C. This peak was associated with hydrocarbon fragments, although a nickel carbide phase (discussed below) has a similar binding energy. As the graphene film grows, the 283 eV carbon species diminishes and the graphene

peak at 284.7 eV saturates at completion of a monolayer. At higher growth temperatures (669 °C) graphene only exists at the surface as long as carbon is supplied. Once the hydrocarbon is shut off, the graphene peak decreases and disappears after ~400 s. This indicates that carbon dissolves into the bulk at high temperatures. This is consistent with AES studies that showed that graphene is stable at the pure Ni surface up to 650 °C [70]. This temperature is lower compared to the temperature determined on a carbon saturated Ni crystal where graphene was found to be stable up to ~900 °C [18]. This illustrates that the stability and growth of graphene on Ni is related to the subsurface carbon concentration, which in many experiments is difficult to control. In general a much lower hydrocarbon exposure is required for graphene growth on ultrathin Ni-films (e.g. Ni/W(110)) than on bulk Ni(111) samples, further indicating a significant loss of carbon into the bulk during growth on bulk samples. Importantly, in UHV growth studies of graphene, the growth temperature is also adjusted below the phase stability temperature of graphene on Ni which is only ~650–700 °C (although this temperature may increase with increasing carbon concentration in the bulk) and this enables monolayer growth at the surface, while in CVD growth higher temperatures (~900 °C) are commonly employed in a tube furnace. This results in saturation of the Ni-bulk with carbon and consequently graphene growth by carbon segregation upon sample cooling [83].

In addition, Ni is special compared to all the other transition metals investigated in that the surface exhibits a surface carbide phase, i.e. carbon can form a third phase in addition to the dilute carbon lattice gas and graphene overlayer. This phase is an ordered surface-carbide, i.e. a carbide confined to the surface layer. Its structure has been described as a quasi-square Ni_2C overlayer on the hexagonal Ni(111) surface with a $\sqrt{39}\bar{R}16.1^\circ \times \sqrt{39}R16.1^\circ$ structure where $\bar{R}$ and R represent rotation in clock- and counterclockwise direction, respectively [113,114]. This structure and a representative STM image of the surface carbide face are shown in Fig. 8(a). The surface carbide and graphene have characteristic AES C_{KVV} peak shapes as shown in Fig. 9(a) and (b). Therefore, AES can be used to differentiate between carbide and graphene. This difference in the AES C_{KVV} peak was used to understand the thermal stability of these surface phases. As mentioned above, the graphene is stable to 650 °C while the carbide is only stable to 460 °C; above these temperatures carbon dissolved into the bulk. Consequently, between 460 °C and 650 °C graphene grows on pure Ni without the presence of a carbide. The lower phase stability temperature of the carbide compared to the graphene surface phase, also has the consequence that if graphene is grown by carbon segregation from the bulk upon sample cooling the graphene phase forms before the carbide can form and thus under these conditions graphene is grown in the absence of a carbide. In UHV studies the graphene growth can be monitored in AES as shown in Fig. 9 where the C_{KVV} only shows the peak shape characteristic of graphene. Below 460 °C a carbide can form whose formation is rather rapid compared to the growth of graphene. The carbide phase once formed may prevent the nucleation of the carbon-denser graphene phase by carbon segregation from the bulk. It has been proposed that such a graphene nucleation barrier occurs because the ordered carbide is a 'line-phase' within a carbon–Ni(111) surface phase diagram and slight variations from the ideal carbon concentration is associated with a high energy cost [70]. Once graphene nucleated within the surface carbide the graphene sheet can grow. This has been observed by the transformation of C_{KVV} AES signal from a carbide to a graphene peak shape (see Fig. 9(e) and (f)). This growth of graphene is fundamentally different than the growth of graphene in the absence of the carbide. As STM imaging shows, the growing graphene does not have 'free' edges in the presence of a carbide but rather is in direct contact with the carbide phase, i.e. the graphene and the carbide exist in the same atomic layer and form an in-plane phase-boundary [73]. At this boundary graphene is formed, presumably by replacing Ni-atoms by carbon. A consequence of the growth of graphene at the boundary to the surface-carbide is that not the Ni(111)-substrate but the carbide boundary determines the orientation of graphene. The carbide phase is rotated by 3° relative to the ⟨1–10⟩ direction of the Ni(111) substrate (see Fig. 8(a)). This rotation is imposed on the growing graphene by matching the graphene to the carbide at its common boundary. The rotation of the graphene with respect to the substrate causes the formation of a moiré superstructure, which is not observed if graphene grows in the absence of the carbide at elevated temperatures. Fig. 8(b) shows the moiré structure observed in STM as well as the one-dimensional interface between the graphene and carbide phases.

In conclusion, on Ni, three distinctively different growth scenarios can be observed. Below 460 °C a Ni_2C surface phase forms readily and graphene growth appears to proceed by the in-plane transformation of the carbide along a one-dimensional graphene-Ni_2C phase boundary. At temperatures between 460 and 650 °C graphene grows on pure Ni and the growth mechanisms may not differ much from that on other transition metals. Above 650–700 °C carbon dissolves into the bulk and graphene is only formed during cooling of the sample by carbon precipitating to the surface.

2.2.4. Copper

The growth of graphene on copper has been motivated by the low carbon solubility in copper because this suppresses multilayer formation due to carbon segregation from the bulk. This enables self-terminating single layer growth even under high pressure conditions. However, copper is fairly non-reactive and sufficient hydrocarbon decomposition for CVD growth of graphene only occurs at elevated pressures and high temperatures. The growth temperatures for graphene are close to the melting temperature of copper and this may cause problems in the stability of the copper substrate.

As outlined above, the interaction between graphene and copper is weak and this may explain the observations that step edges and surface facets and grain boundaries in a copper substrate are easily 'crossed' by the growing graphene sheet. On the other hand, the weak interaction leads to the formation of many rotational domains and thus it is challenging to obtain large single crystalline domains. However, minimizing the nucleation density by choosing appropriate conditions during CVD growth have recently shown to achieve single crystal graphene grains on copper foil as large as 0.5 mm in side-length [115]. To overcome the low decomposition rate of hydrocarbons in vacuum, graphene growth on copper foil was conducted by elemental carbon deposition, which enabled LEEM investigations of the graphene growth [116]. In these experiments copper foil was (100) textured, as is the case for most cold-rolled copper foils, with grain sizes as large as 1 mm. Thus for all practical purposes this can be considered a single crystal study on Cu(100). Heterogeneous nucleation of graphene was observed. At each nucleation site, four graphene grains nucleated and grew approximately in the ⟨001⟩ direction of the substrate. Each of the graphene grains had a different crystallographic alignment with the substrate. Higher growth velocities of graphene in the ⟨001⟩ direction of the copper substrate resulted in a four-lobed graphene island consisting of the four graphene grains, as shown in Fig. 10. The dependence of the growth velocity on different substrate directions is not well understood yet, but it may indicate that the way the edges of the graphene bond to the substrate influences the carbon attachment rate to the graphene edge. Graphene only grew at substrate temperatures of above ~790 °C. At this temperature

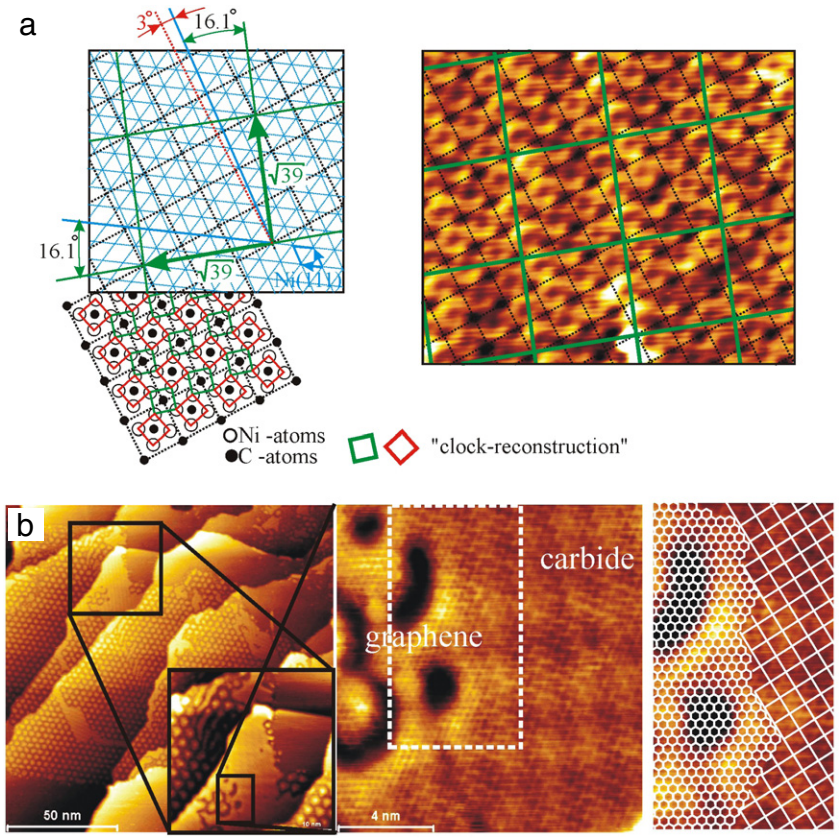

Fig. 8. Carbon phases on Ni(111). The structural model and STM image of the Ni_2C surface phase is shown in (a). It consists of a quasi-square carbide phase with a 'clock-reconstruction' on top of the hexagonal Ni(111) surface, giving rise to a large unit cell. A STM-'snapshot' of the transformation of the carbide phase into graphene is shown in panel (b). The left large scale (150 nm) image shows regions of graphene with a moiré-pattern and carbide patches. Zoomed-in images characterize the carbide–graphene interface shown on the right side of panel (b). It is apparent that the carbide and graphene are within the same atomic layer and the 1D-interface is perfectly matched, i.e. no defects are discernible.
Source: Adapted from Ref. [73].

sublimation of copper from step edges occurs. As retreating step edges interfere with a graphene island, the sublimation rate from the step edge is suppressed, presumably because the Cu-atoms are trapped underneath the graphene and need to diffuse to the edge of the graphene island to leave the surface. This causes the surface morphology to change with mounds forming underneath the graphene islands. The formation mechanism by retreating step edges is schematically shown in Fig. 10(f)–(i). This surface roughening may influence the quality of the graphene that can be obtained. Note, that for the above mentioned 100's of micrometer-sized graphene grains, the Cu-foils was enclosed by copper [115]. This may help to reduce the loss of copper from the surface by resupplying copper from surrounding copper surfaces.

2.2.5. Summary of graphene growth on metals

Table 2 gives an overview of graphene growth studies on late transition metals. The carbon solubility in the transition metal bulk indicates whether graphene may grow (additional layers) upon cooling by carbon segregation from the bulk. Multilayer formation in high-carbon soluble materials may be counteracted by the use of thin-metal films rather than bulk metal foils to reduce the amount of dissolved carbon in the metal.

UHV studies of graphene growth on various metals have given detailed insight in the formation mechanisms of graphene. Especially in-situ LEEM studies have provided information on the dynamics of the growth. Furthermore, there is evidence that CVD growth at elevated hydrocarbon pressures follow the same fundamental growth processes as those revealed by the UHV studies. It has been shown that graphene growth on both Ru and Ir, i.e. a strong and weak interacting substrate, occurs by addition of carbon clusters to the graphene edges rather than carbon monomers. This may be a universal process for graphene growth on transition metals as the carbon monomers are more strongly bond to the substrate and the formation of intermediate carbon clusters may reduce the energetic barriers for carbon attachment. Also, for the growth of graphene on Ir it was found that the growth velocity depends on the orientation of the graphene relative to the substrate and for graphene on Cu(100) the growth velocity was non-uniform with the substrate direction. This may imply that the interaction of the graphene edges with the substrate may also play an important role for the carbon attachment rate. DFT calculations for graphene on Ni, for instance, have shown that the graphene edges form bonds to the Ni-substrate [70]. Breaking these bonds for attaching carbon will add to the 'carbon attachment barrier'. The strength of the bond to the substrate will depend sensitively on the position of the edge atoms relative to the substrate atoms and therefore this may give rise to orientation dependent barriers and growth rates. However, there exist no detailed studies of such effects to date.

Although there are similarities between the growths of graphene on different metals there are also differences. On Ru, for instance, it appears that graphene interacts strongly with step edges which causes the growth of graphene in a step down direction only and under certain growth conditions the etching of step-up edges. On Ir, the interaction with steps is much smaller allowing the growth of graphene over both, up and down step

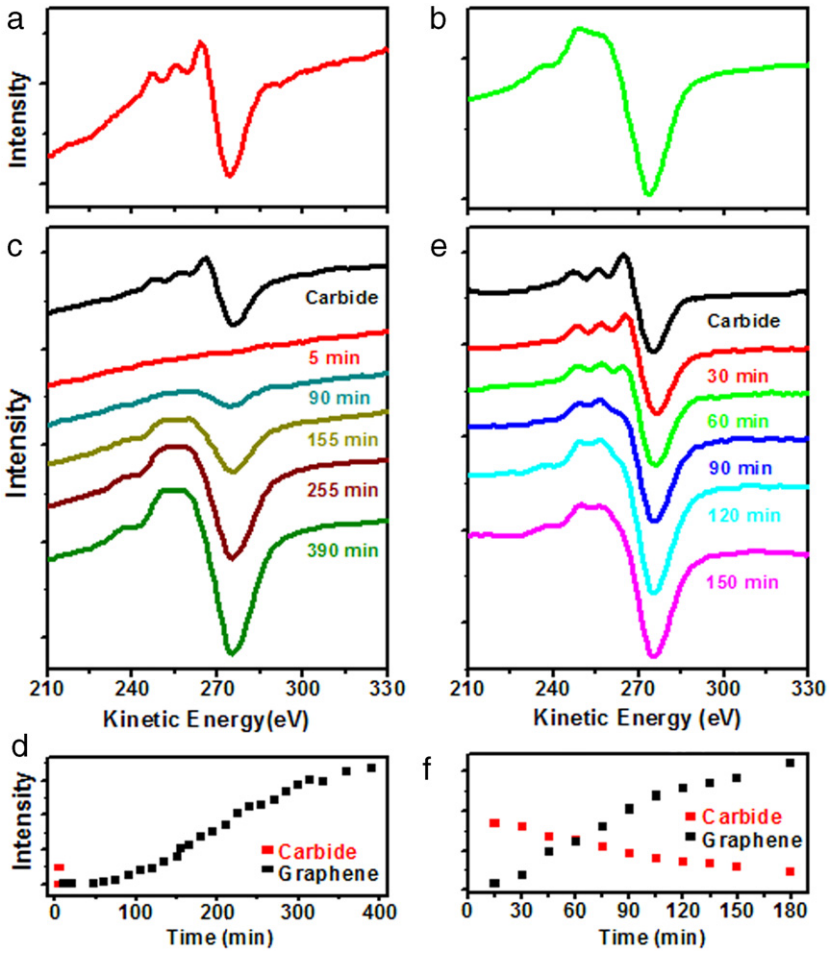

Fig. 9. Graphene growth on Ni(111) monitored by Auger electron spectroscopy (AES). AES can be used to differentiate between graphene and carbide surface phases. (a) and (b) show the C_{KVV} Auger signal for the carbide and graphene phase, respectively. The growth of graphene by carbon segregation from the bulk is monitored by AES in (c) and (e) for temperatures above and below 460 °C, respectively. Upon annealing to above 460 °C the carbide signal disappears and the graphene grows in the absence of any surface carbide on Ni(111), whereas at low temperatures the carbide transforms into graphene in accordance with the STM-images show in Fig. 8. The time evolution for the carbide and graphene components for graphene growth by carbon segregation above and below 460 °C is shown in (d) and (f), respectively.
Source: Adapted from Ref. [73].

edges. On Cu the interaction between graphene and the substrate is very weak allowing overgrowth of steps and larger surface features such as facets and grain boundaries. Ni is special for all the transition metals in that it has a carbide surface phase in addition to graphene. The carbide phase may play a role for low temperature growth. However, if graphene is grown by carbon segregation from the bulk by cooling from high temperatures, then the graphene sheet is likely to form before the lower phase-stability temperature of the surface carbide is reached and thus the carbide may never be observed.

2.3. Graphene-moiré patterns as templates for metal cluster formation

The corrugation arising from the lattice mismatch or rotation of the graphene lattice with respect to the metal substrate has been recognized as a template for self-assembly of metal clusters. The strongly verifying interaction of the graphene sheet with the metal substrate depending on the position of the carbon atoms with respect to the metal lattice gives rise to a corrugated surface, as discussed in detail in Section 2.1. Vapor-deposited metals on these corrugated graphene sheets may experience different adsorption strengths at different sites, resulting in preferred nucleation sites within the moiré superstructure unit cell. Preferential nucleation sites of deposited metals on graphene moiré patterns have been observed for several systems: Ir [122], (Pt, W, Re, Fe, Au) [123] on graphene/Ir(111); (Pt [124,125], Co [126], Rh, Pd, Au) [127], Ru [128] on graphene/Ru(0001), and Ni [129] on graphene/Rh(111).

The adsorption sites of metal clusters in graphene moiré structures may depend on the substrate material. For metal adsorption on graphene/Ir it was observed in the STM images shown in Fig. 11(a) and (b) that sites in the moiré-pattern where the carbon ring is centered over the hcp-hollow site of the Ir(111) substrate (see Fig. 1(b)), are the preferred nucleation sites [101, 123]. This contrasts with the moiré structure on Ru(0001), where sites with the carbon ring centered over the fcc-sites (Fig. 1(c)) in the moiré-pattern acts as the preferred nucleation site [127,128] whereas for Ni on graphene/Rh(111) nucleation in both fcc and hcp sites were observed [129]. The cluster formation and their thermal stability also depend on the cluster material.

On graphene/Ir(111) highly perfect cluster superlattices can be grown for Ir, Pt, W, and Re; see for example Fig. 11(c) for Ir clusters. For Ir clusters initial growth is 2D and it transforms to 3D growth when the cluster reaches ~25 atoms [101]. Investigations of the thermal stability showed that the Ir-clusters were the most stable. Pt clusters also remained intact to annealing temperatures up to 400 K. It has been suggested that the cluster decay is due to merging of metal clusters, i.e. at elevated temperatures the clusters

Table 2
Summary of graphene growth on late transition metals and comparison of lattice constants between graphene and densely packed metal surfaces. The values for the bulk-carbon solubility for the transition metals has been taken from Ref. [117]. The growth methods are categorized as CVD: using a tube furnace CVD-reactor; UHV-CVD: exposure of metal samples to low pressure hydrocarbons (equal or less than 10^{-6} Torr) inside a UHV chamber; MBE: vapor deposition of atomic carbon onto a metal substrate in UHV; and ethylene irradiation: using a low energy ion gun to irradiate the surface ethylene ions.

	Surface lattice constant (Å)	Carbon solubility at 1000 °C (at.%) Ref. [117]	Graphene growth method/comment
Graphite	2.46		
Co(0001)	2.52	3.41	UHV: dehydrogenation of adsorbed hydrocarbons [81]
Ni(111)	2.49	2.03	UHV-CVD; $< 10^{-6}$ Torr hydrocarbon (commonly ethylene) at ~500–650 °C; the required exposure depends on sample T and sample (bulk Ni [68] vs. Ni-film on W(110) [112]). CVD (CVD on Ni-foils at $>$ 900 °C mostly leads to multilayer graphene formation by carbon segregation from the bulk [83])
Cu(111). Most Cu-foils have a (001) texture	2.56	0.04	UHV: dehydrogenation of adsorbed hydrocarbons [84]; CVD(on Cu foil has become the mainstream method for monolayer graphene synthesis [31,32]); MBE [118] Ethylene irradiation [119]
	.	.	
Ru(0001)	2.71	1.56	UHV-CVD [103]
Rh(111)	2.69	0.89	UHV-CVD [67]
Ag(111)	2.89	0.01	Graphene/Ag interfaces only formed by Ag-intercalation; graphene has not yet been directly grown on Ag substrates.
Pd(111)	2.75	5.98	UHV-CVD [64,65]
Re(0001)	2.76	4.39	UHV-CVD [66]
Ir(111)	2.72	1.35	UHV-CVD [50,53]
Pt(111)	2.77	1.76	UHV-CVD [17,59]
Au(111)	2.88	0.01	CVD [120] Ethylene irradiation [119] MBE [121]

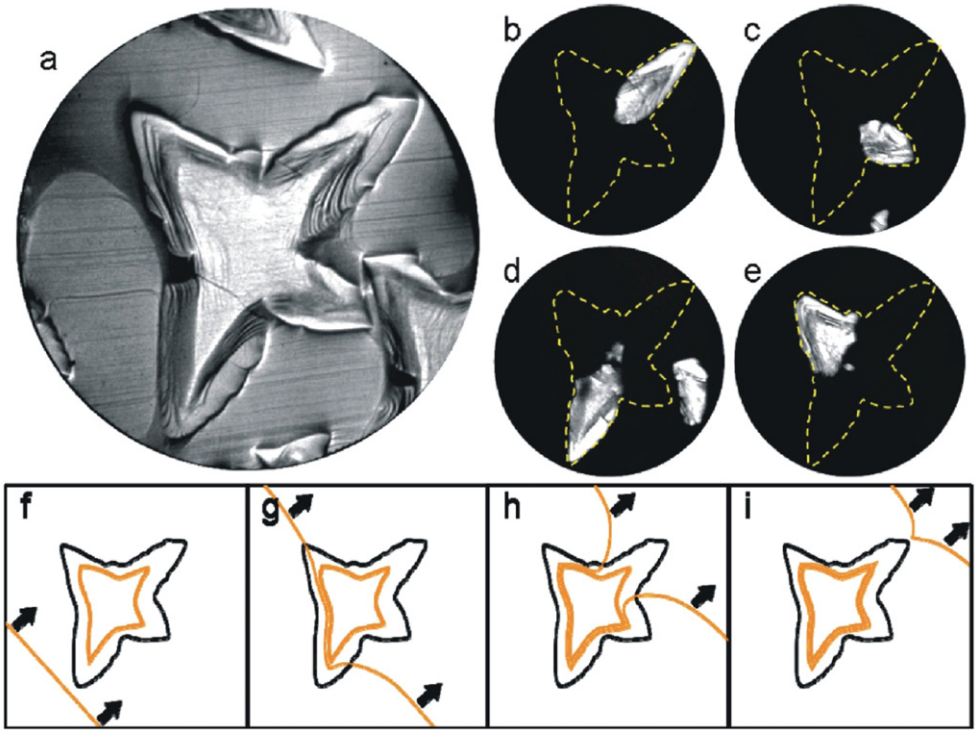

Fig. 10. LEEM study of graphene growth on copper foil with (100) texture. Four-lobed graphene islands are observed (a). Dark-field LEEM images in (b)–(e) demonstrates that each lobe is a separate graphene grain with different orientation relative to the Cu(100) substrate. The high temperature needed to grow graphene on Cu causes Cu-sublimation from the substrate, which causes mound-formation underneath the graphene islands. The mechanism of mound formation is illustrated in (f)–(i). Cu-sublimation is reduced underneath of the graphene islands causing a 'pinning' of retreating monatomic step edges and thus causes the build-up of a mound.
Source: Reproduced from Ref. [116].

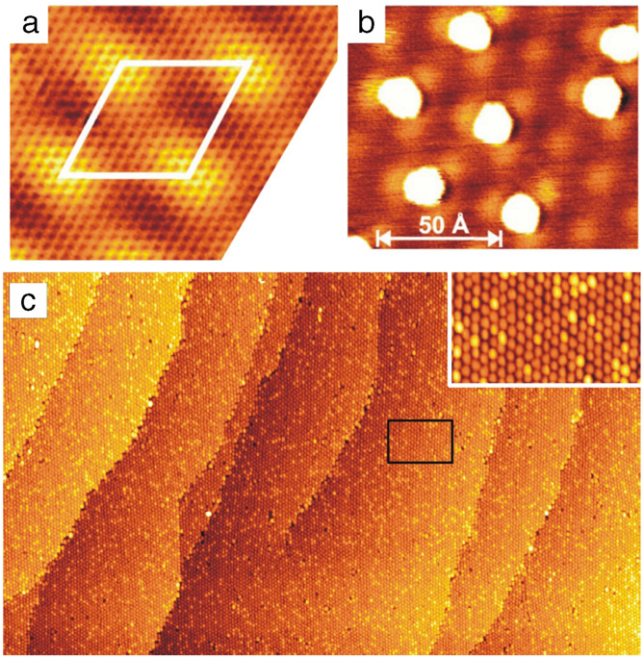

Fig. 11. Ir-cluster arrays on Ir(111) supported graphene. (a) Atomic-resolution STM image of the pristine moiré structure of graphene on Ir(111). (b) STM image of adsorption of Ir (0.02 ML) on top of the graphene moiré structure. Preferential adsorption of Ir in the 'depressed' regions of the moiré is apparent. (c) Ir-cluster superlattice obtained by depositing 0.8 ML Ir on graphene/Ir(111). Large scale image 0.5 μm × 0.3 μm, inset 50 nm × 30 nm.
Source: Reproduced from Ref. [101].
© 2006, The American Physical Society.
Source: Reproduced from Ref. [123].
© 2009, Institute of Physics.

fluctuate around their equilibrium position and once they make contact with an adjacent cluster, the two clusters merge. Ni, Fe, and Au did not lead to ordered superlattice growth, although some preferential nucleation is evident at low growth temperatures. It has been shown, however, that ordered arrays may still be obtained for these elements by first seeding the cluster growth by depositing low amounts of Ir, which then 'anchor' Ni, Fe, or Au clusters [123].

On graphene/Ru(0001), Pt and Rh form finely dispersed metal clusters while Pd and Co form larger clusters at similar metal coverage. Au initially nucleates at fcc sites similarly to the other metals but continues to grow in a 2D fashion all over the graphene, covering the entire moiré-structure. Rh clusters exhibit the highest thermal stability with little changes up to annealing temperatures of 900 K. At this temperature Ostwald ripening is setting in, i.e. atoms diffuse from smaller to larger clusters [127]. This is in contrast to the coalescence of clusters suggested for Pt on graphene/Ir(111).

The formation and stability of clusters on graphene moiré structures obviously depends on the deposited metal. There are several parameters that can give rise to the different behavior of the metals, such as lattice constant of the deposited metals, cohesive energies of the metals, and the interaction (bond strength) between the metal and the graphene. The high stability of Ir on graphene/Ir(111) has been explained by DFT calculation to be a consequence of strong Ir–C bonds through a re-hybridization of the carbon from $sp^2 \rightarrow sp^3$ underneath of Ir clusters with at least two Ir-atoms [130,131]. Such a mechanism may also explain the stability of Rh clusters on graphene/Ru(0001). One may conclude that the different local arrangements of carbon atoms within the moiré supercell only allows re-hybridization of the carbon from $sp^2 \rightarrow sp^3$ in certain areas of the moiré structure and thus cause a strongly varying admetal–carbon interaction. This determines the nucleation and ordering of metal clusters, for metals that can induce the re-hybridization in the graphene. For admetals that do not induce $sp^2 \rightarrow sp^3$ re-hybridization the local variation of the adsorption energy within the moiré structure is weak and therefore the metal cohesive energy favors formation of larger clusters without preferred adsorption sites on the graphene moiré-structure. The transition from 2D metal cluster to 3D metal clusters depends on the relative difference of metal–carbon bond strength and metal cohesive energy. If the metal–carbon dissociative energy is larger than the cohesive energy, 2D clusters form. With increasing cluster size the cohesive energy increases and therefore the cluster shapes transforms to a 3D growth once a critical cluster size is reached [127]. The 2D growth of Au on graphene/Ru(0001) up to a coverage of 0.75 ML and its stability up to room temperature [132] is not explained by the interplay of metal–carbon bonds and metal cohesive energy, though, indicating that in specific cases other phenomena become important. The unusual growth of Au on graphene/Ru(0001) is as yet unexplained.

Highly uniform metal cluster superlattices may be interesting model systems for metal cluster research. For instance graphene supported metal clusters, especially those with high thermal stability, may make excellent model systems for heterogeneous catalysis research. Also it already has been shown that the unusual 2D Au layer on graphene may have exciting catalytic properties such as catalyzing CO oxidation [127]. Also studying magnetic properties of metal clusters would be interesting [129], unfortunately most interesting materials for this purpose (Fe, Ni, Co) do not form well ordered superlattices.

3. Making ribbons and other graphene structures: cutting, etching, and template-growth of graphene

One attractive prospect of graphene, in contrast for example to carbon nanotubes, is that it can be handled as a wafer and patterned and cut by lithography methods much like in today's silicon technology. A potentially major application of graphene is in high frequency field effect transistors (FETs). To use graphene in FETs a sizable band gap is required, however [133]. One way to introduce a band gap in graphene is to laterally confine the charge carriers, which may be achieved by making graphene nanoribbons with limited widths. In nanoribbons, the band gap becomes dependent on the width and the edge orientation [134–137]. In this chapter we discuss different approaches to synthesizing graphene nanoribbons [138] and other morphologies. We mainly focus on self-formation processes and *not* on direct lithography methods, like cutting of graphene with an STM [139] or an atomic force microscope (AFM) [140] tip out of a graphene sheet, or other lithography methods using deposition/exposure masks [141,142]. An important aspect to the functionality of graphene ribbons is the structure and termination of the edges. Atomic-scale edge structures are discussed in Section 4.

3.1. Direct growth of nanoribbons

Graphene nanoribbons are potentially important for FETs. The lateral quantum confinement of electrons in the ribbons opens a band gap which is essential for sufficient on/off switching ratios in FET applications. In this section we are investigating various approaches for the fabrication of nanoribbons that may be used as model systems for proof-of-principle devices or as building blocks in future electronic applications.

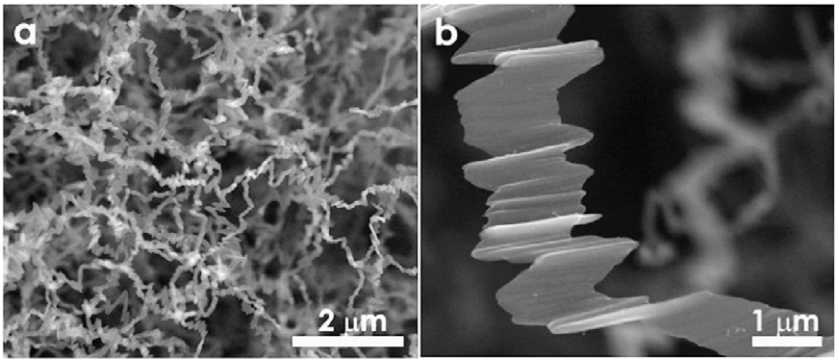

Fig. 12. SEM images of multilayer graphene nanoribbons grown by a chemical vapor reaction process.
Source: Reproduced from Ref. [145].

3.1.1. Growth using a catalyst

Multilayer graphene fibers (or graphite) with limited widths may be obtained in similar ways as carbon nanotubes from catalyzed growth on metal or carbide nanoclusters in a CVD process. This has been demonstrated as early as 1990 [143]. In these early studies graphite nanoribbons were produced through decomposition of $CO/H_2/Fe(CO)_5$ at 400–700 °C. These graphite ribbons had dimensions of 10 μm long, 100–700 nm wide, and 10–200 nm thick with an iron carbide particle at the end. More recent studies investigated the formation of graphite filaments by decomposition of ferrocene and tetrahydrofuran at 950 °C [144] and ferrocene/ethanol/thiophene also at 950 °C [145]. The latter approach produced ribbons ∼40 graphene layers thick, 20–300 nm in width, and tens of microns in length as is shown by the SEM images in Fig. 12.

3.1.2. Growth at surfaces

Surfaces as templates: Surfaces may act as a template if they exhibit morphologies that assist assembly of nanostructures. Such morphologies may be (periodic) step edges on vicinal surfaces or certain crystallographic orientations on faceted surfaces. There are no recent studies that would clearly demonstrate by microscopic means that such surface morphologies can be successfully used for the fabrication of graphene nanoribbons. Older reports indicate that graphene nanoribbons may be grown on vicinal Ni surfaces [146–148]. However, the recent findings that graphene easily grows across step edges cast some doubt on these reports. For carbide surfaces, the TiC surface has been claimed to be a useful template for growing graphene with limited lateral extend [149]. A TiC(111) surface facets into 'pyramids' with (100) microfacets of ∼200 nm upon annealing. Graphene can be grown on this microfaceted surface as demonstrated by ARPES. A vicinal TiC(410) surface exhibits (100) terraces of 0.886 nm width and it was suggested that this allows growth of graphene nanoribbons of the same size. This may need further investigation though.

Molecules as building blocks: An exciting new approach of designing graphene ribbons and other graphene nanostructures has been recently demonstrated by coupling of molecules into chains at surfaces [150]. In these experiments precursor hydrocarbon molecules with two halogen endgroups were deposited from a Knudsen cell on a gold or silver surface. At the deposition temperatures of ∼200 °C the halogen atoms are removed from the precursor molecules, yielding biradical species. These form the building blocks for chain molecules. As the radicals diffuse across the surface they undergo radical addition reaction. Subsequent annealing to higher temperatures (∼450 °C) a surface assisted cyclodehydrogenation reaction establishes an extended fully aromatic system. Fig. 13(a) shows the schematic reaction path for this process for 10,10′-dibromo-9,9′bianthryl precursors. This process results in graphene nanoribbons of uniform width with armchair edges and 7 carbon rows wide. STM images of the final wires are shown in Fig. 13(b) and (c). By choosing other appropriate precursors the width of the graphene ribbons can be selected or more complex graphene architectures can be achieved such as zigzag wires or *Y*-junctions within the wires. The versatility of this approach and the high accuracy by which it allows to control the ribbon size and morphology makes this a promising method for synthesizing graphene nanoribbons with well controlled, predefined properties. One challenge for practical application may be the scalability of the process and the controlled transfer of the ribbons into devices. The controlled assembly of graphene nanoribbons appears to be a similar problem to that of making carbon nanotube electronics.

3.2. Chemical cutting and etching

Atomic oxygen and hydrogen can attack graphene. Initially chemisorbed species may form at the graphene surface (see Section 5); however, especially at elevated temperatures complete oxidation of graphene may occur. Edges of graphene are much more prone for chemical attack allowing for selective etching of graphene edges by hydrogen or oxygen if the parameters are chosen correctly. Graphene sheets can be patterned by delivering etchants (such as hydrogen or OH^- radicals) at predefined locations. One way to achieve this is by using a patterned catalyst that activates the etchant locally, e.g. cracking H_2 into atomic hydrogen. In the following we briefly summarize methods that have been developed to chemically attack graphene in order to obtain defined nanostructures.

3.2.1. Unzipping of carbon nanotubes

Graphene nanoribbons can be obtained from carbon nanotubes by 'unzipping' them along their axis by oxidative processes. Ab-initio computational studies of the unzipping process propose that epoxy groups that are formed during oxidation have a tendency to align in a line. These aligned epoxy groups then cause rupture of the underlying C–C bond causing the unzipping of the graphene sheet [151]. This process causes the termination of the newly created graphene edges with carbonyl groups [152]. A solution based oxidative process using sulfuric acid (H_2SO_4) and potassium permanganate ($KMnO_4$), as an oxidizing agent, has been shown to unzip multiwall carbon nanotubes [153]. This process resulted in oxygen containing edge groups that can be removed by annealing in hydrogen. In a related study it was shown that the unzipping process can be optimized at 60 °C and adding a second acid ($C_2HF_3O_2$ or H_3PO_4). The second acid prevents the creation of vacancies in the nanoribbon. Furthermore

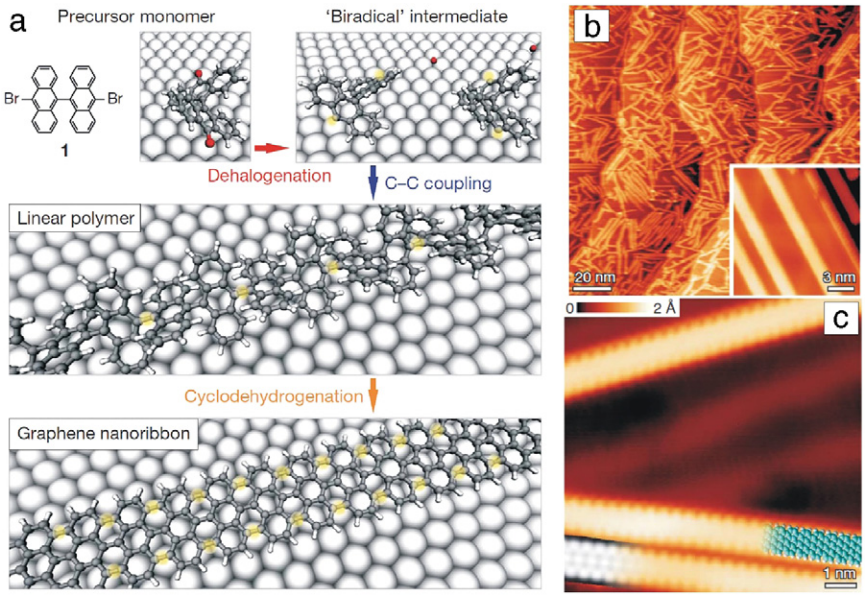

Fig. 13. Synthesis of graphene ribbons on Au(111) surface by molecular coupling reactions. (a) Schematic of molecular reactions. (b) and (c) STM image of the graphene nanoribbons obtained in this process.
Source: Reproduced from Ref. [150].

the degree of oxidation can be adjusted by controlling the amount of oxidizing agent ($KMnO_4$). This results in much longer (>5 mm) and narrower ribbons (<100 nm) with more atomically perfect edges [154]. Plasma etching [155] of partially polymer-embedded nanotubes enabled the production of graphene nanoribbons with a narrow (10–20 nm) width and better edge quality. Unzipping by alkali-atom intercalation was demonstrated for Li intercalation in conjunction with ammonia [156].

3.2.2. Cutting graphene with catalysts

Ni [157,158] or Fe [159] metal clusters deposited on graphene or HOPG can etch graphene if heated in a hydrogen atmosphere. It is proposed that the metal acts as a catalyst to promote hydrogenation reactions as follows:

$$C(s) + 2H_2(g) \xrightarrow{Ni/Fe} CH_4(g). \quad (2)$$

This etching process yields straight edges determined by the crystallographic orientation of the graphene. It has been proposed that preferential zigzag or armchair edges can be obtained depending on the metal cluster size [158]. Defects of free edges in the graphene may act as obstacles that cause a 'deflection' of the cluster and change in the etching direction, allowing for some control of the obtained etching pattern.

Photocatalytic patterning of graphene was demonstrated by using a TiO_2 photomask that is brought in close proximity to graphene [160]. Illumination of the photomask generates OH^- radicals that attack the graphene and locally etch it. By patterning the TiO_2 mask using standard lithography techniques arbitrary patterns can be etched into graphene. This is a solution-free, potentially scalable and cost-efficient approach for structuring graphene and the fabrication of graphene based devices.

3.2.3. Chemical etching of graphene edges

Narrowing of graphene nanoribbons was achieved by selective etching from the edges. Using a hydrogen plasma at a sample temperature of 300 °C it was possible to narrow graphene nanoribbons obtained from unzipping carbon nanotubes to a sub-5 nm width [161]. Importantly at this sample temperature no damage of the graphene basal plane was observed. An etching rate of 0.27 ± 0.05 nm/min and 0.10 ± 0.03 nm/min was measured for single layer and multilayer graphene, respectively. The same group also demonstrated selective etching of graphene edges of graphene pre-patterned by standard lithography techniques. In this way wide graphene features can be formed by lithography and then critical features can be narrowed to a desired width of <10 nm [162] and thus obtain feature sizes that are beyond the resolution of standard lithography. The authors experimented with different O_2 and H_2 or NH_3 mixtures. The best results, i.e. slowest etching rate of 1 nm/min, was obtained under ~25 mTorr of O_2 in 1 Torr of 10% NH_3 in Ar. The prepared nanoribbons demonstrated a high on/off ratio of $\sim 10^4$ at room temperature in field effect transistors built with sub-5 nm graphene nanoribbon semiconductors.

The dynamics of oxygen etching of metal (Ru, Ir) supported graphene islands were investigated by LEEM [163,164] and photoemission electron microscopy (PEEM) [165] in UHV. Two etching mechanisms were observed [164]. One etching mechanism observed for 980–1070 K and O_2 pressures of 5×10^{-7} Torr, is the inverse of graphene growth, i.e. oxygen is consuming carbon monomers on the metal surface by reacting carbon to CO. This causes the detachment of carbon from the graphene to re-establish a carbon-equilibrium between carbon in the lattice gas and carbon in graphene. For graphene on Ir, etching rates dependent on the orientation of the graphene relative to the substrate was found, which is also in agreement to the observations of orientation dependent graphene growth discussed in Section 2.2.2. In a second etching mechanism oxygen intercalates underneath the graphene [166], which destabilizes the graphene and can cause formation of holes in the graphene islands. Intercalation of oxygen at 550 K and subsequent raising of the temperature to 720 K resulted in direct attack of graphene by oxygen at an extreme rate. For bilayer graphene, it was observed that both layers were etched simultaneously rather than sequentially.

3.3. Electron beam induced damages and patterning

Energetic electron beams can lead to carbon sputtering. The threshold energy for displacing a carbon atom from the honeycomb lattice is 18–22 eV according to first-principle calculations [167,168] and 18–20 eV according to experiments [169,170].

This displacement energy requires an electron beam energy of 90–100 keV to form defects by a 'knock-on' process [171]. These are values that are easily reached in transmission electron microscopes (TEMs) and scanning transmission electron microscopes (STEMs) and therefore these instruments have been used to create defects and simultaneously characterize them. By choosing the electron beam energy of 80 keV, i.e. just below the threshold for knock-on damage, it was shown that one can still remove the more weakly bond carbon atoms at edge-sites of multilayer graphene. This enables one, for example, to selectively remove monolayers from the surface [172]. The preferential removal of edge atoms was also used to narrow graphene nanoribbons, and even to eventually obtain a single carbon-atom thread, i.e. either polyyne (. . . C ≡ C–C ≡ C . . .) or cumulene (. . . C=C=C=C . . .) [173]. The formation of point defects for electron energies above the knock-on threshold and the eventual transformation into amorphous carbon was also studied in high resolution aberration corrected TEM [174]. Point defects in graphene will be described in Section 4. A focused electron beam can also be used to form nanometer scaled pores, slits, and gaps within suspended graphene without introducing long range distortions of the graphene [175]. This may open up opportunities for the design and fabrication of more complex graphene structures for research purposes. Irradiation of multilayer graphene by highly energetic electrons in air resulted in an oxidation of graphene [176]. This is a consequence of the creation of reactive sites in electron beam damaged graphene. If used in a controlled way (electron current and ambient), this may be an approach for chemically functionalizing graphene.

4. Atomic-scale imperfections in the graphene

Defects can be characterized by their extent as zero, one, or two dimensional defects. A point defect (zero dimensional) may be vacancies or interstitials; in graphene a structural defect described by a bond rotation (Stone–Wales defects) is also possible that does not require any change in the carbon density. The restructuring of the carbon lattice surrounding these point defects causes them to exhibit a lateral extent of ∼1 nm. Extrinsic defects such as substitutional dopants on the other hand may maintain the hexagonal lattice in first approximation. Higher dimensional defects such as (one-dimensional) dislocations are properties of 3D-bulk materials where it is defined by a Burgers vector and a dislocation line. Strictly speaking dislocations cannot exist in a 2D material like graphene. Two dimensional defects in bulk materials, such as grain boundaries, become 1-D defects in graphene. All these defects have fairly high formation energies. Even zero dimensional defects such as single vacancies or Stone–Wales defects have formation energies of 7.3–7.5 eV [177], and 4.5–5.3 eV [178,179], respectively. As a consequence, graphene has very few defects in thermodynamic equilibrium at room temperature. However, there have been only a few studies of the defects that may form during growth by, for example, CVD processes at metal surfaces. It is likely that under various growth conditions defects may be (kinetically) trapped in the graphene sheet. Another more obvious defect that forms in graphene grown by CVD on weakly interacting metal surfaces (e.g. on Cu or Pt) is rotational domain boundaries. These defects, in addition to the structure of free graphene edges, the effects of impurities, and 1D heterointerfaces, are discussed in this chapter.

4.1. Intrinsic point defects and defects with limited lateral size

In this sub-section we discuss pure carbon structures with defects of only very limited extent, i.e. defects that are surrounded by undisturbed honeycomb lattice. These defects may be single defects or an array of defects that form a closed loop structure. Strictly speaking these are not all point defects since some can have a lateral extend of a few nanometers. We categorize these defects by the number of carbon atoms, i.e. we distinguish defects that have the same number of carbon atoms, and defects that have more or less carbon atoms compared to a defect-free graphene lattice.

4.1.1. Structure of defects

Defects maintaining carbon density: A bond rotation by 90° of a C–C bond in graphene causes the formation of two pentagons and two heptagons. This kind of defect is called a Stone–Wales defect and does not require any removal or addition of carbon. The high formation energy of ∼5 eV indicates that it only forms at very high temperatures or under electron irradiation in for example a TEM. Once formed, it should remain stable at room temperature because of a high barrier for the reverse transformation. Fig. 14(a) shows a structural model and a TEM-micrograph [180] of the Stone–Wales defect.

Other potential defect structures that do not change the carbon density are closed loop grain boundaries [181]. Conceptually, this can be described by cutting-out a small piece of the graphene, rotating it, and then re-inserting it into the graphene. For certain sizes and rotation angles the edges can be 'stitched' back together by connecting carbon atoms such that all the atoms are three-fold coordinated and form pentagonal and heptagonal rings. In this procedure the number of carbon atoms is conserved. Depending on the area that is 'cut-out' this may become a large defect that is better categorized as a two-dimensional defect with limited lateral extent. However, there is no evidence that larger closed loop boundaries actually form. Fig. 15 shows possible closed loop grain boundary configurations. In the concept of closed-loop grain boundaries, the Stone–Wales defect may be considered as the smallest closed loop grain boundary with the core consisting of two atoms rotated by 90°. The formation energy per pentagon–heptagon pair is the lowest for the structure shown in Fig. 15(b) with only 1.2 eV compared to 2.5 eV for the Stone–Wales defect (note that there are two pentagon–heptagon pairs in a Stone–Wales defect and therefore the energy quoted here is half the total formation energy). 'Flower-like' defects have been observed in TEM for graphene grown by CVD on Ni substrate [182] and by STM on graphene on SiC [183,184] (see Fig. 15(f)). It has been suggested that these 'flower like' defects correspond to the low energy loop grain boundary in Fig. 15(b).

Defects with reduced carbon density: If a single carbon atom is removed, two of the three dangling bonds will recombine and form a pentagon. One dangling bond will remain unsaturated though and this results in a fairly high formation energy of ∼7.5 eV. This structure is shown in Fig. 14(c). Double carbon vacancies allow the graphene structure to restructure in a number of different ways that leaves no dangling bonds, i.e. all carbon atoms are three-fold coordinated. These possibilities and their experimental observations are shown in Fig. 14(d)–(f). Because of the lack of any dangling bonds, double vacancies are thermodynamically favored over single vacancies in graphene. The formation energy of the two pentagons and one octagon structure is 8 eV, i.e. 4 eV per vacancy [177,185]. The lowest double vacancy structure is the three pentagon- and three heptagon-structure with a formation energy of 7 eV, i.e. 3.5 eV per vacancy [186,187]. Thus combining two single vacancies into one divacancy lowers the formation energy by more than 1/2 and thus divacancies are energetically favorable compared to single vacancies.

Defects with added carbon: Similarly to vacancies a single adatom cannot be easily incorporated into a honeycomb lattice and it is either adsorbed on bridge-site or in a so-called dumbbell structure where two carbon atoms are in the same lateral position but are displaced above and below the graphene plane. For two extra

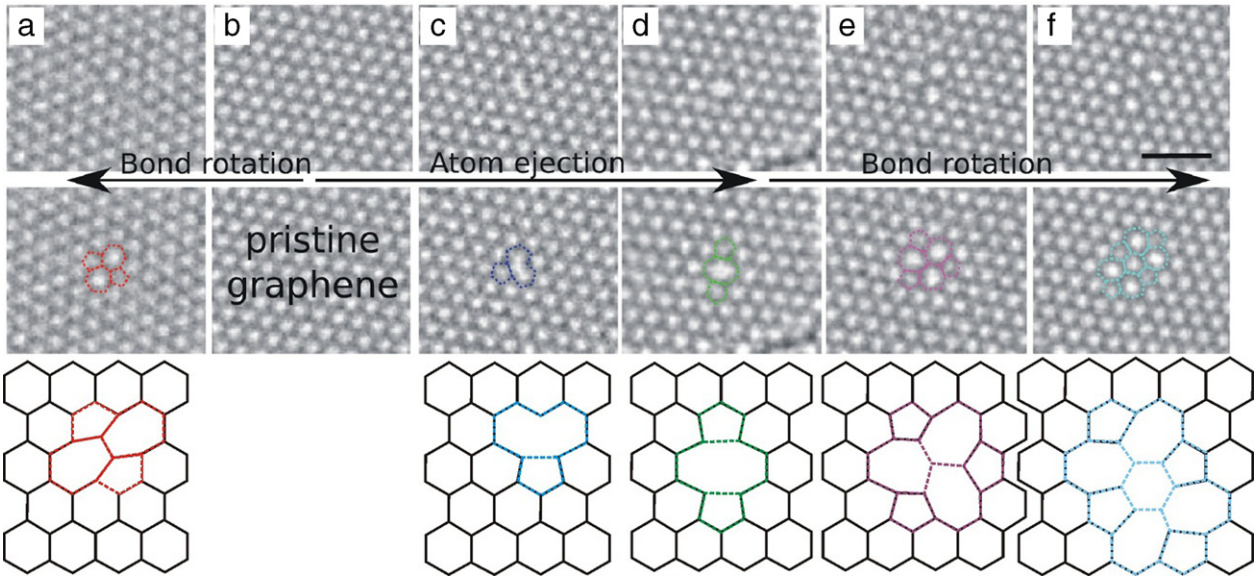

Fig. 14. Atomic scale defects in graphene induced by electron irradiation and imaged with high resolution TEM. (a) Stone–Wales defect, formed by rotating one C–C bond by 90°. (c)–(f) are defects formed by C-vacancy formation and subsequent restructuring of the graphene lattice. The defect structure of a single carbon vacancy is shown in (c). Different defect structures for two missing carbon atoms are shown in (d)–(f).
Source: Reproduced from [174].

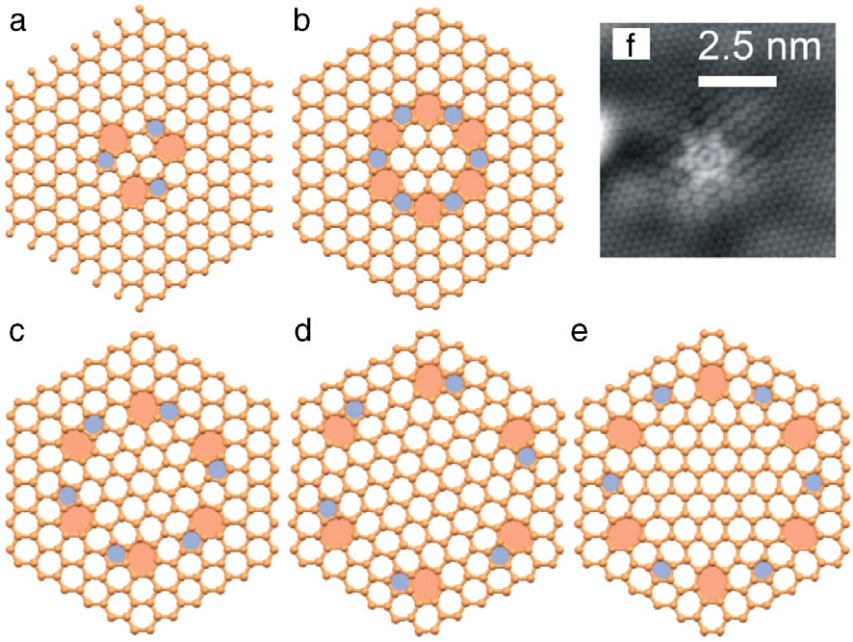

Fig. 15. Closed grain boundary loops in graphene. These defects do not change the carbon concentration and consist of a rotated honeycomb core, surrounded by a loop of pentagon and heptagon defects that form a closed grain boundary. The structure in (b) has the lowest formation energy and it has been suggested that this structure is the 'flower defect' sometimes observed in epitaxial graphene. A STM image of the 'flower defect' found on graphene/SiC is shown in (f).
Source: (a)–(e) reproduced from Ref. [181].

Source: (f) reproduced from Ref. [184].

carbon atoms the graphene sheet can restructure in what has been labeled the 'inverse Stone–Wales' defect; this defect structure is shown in Fig. 16(a). The formation energy of this defect is ~5.8 eV [188,189]. This defect consists of two pentagons and two heptagons, i.e. the same as a Stone–Wales defect. However, because of the higher carbon density and the arrangement of the pentagons, a buckling of the defect atoms out of the graphene plane is caused. To the best of our knowledge this defect has not been observed experimentally so far. Another reconstruction that has two additional carbon atoms is shown in Fig. 16(b); it consists of three pentagons and three heptagons with a hexagon, rotated by 30° relative to graphene hexagons, in the center. This structure has a computed formation energy of 6.07 eV [189], i.e. slightly larger than that of the inverse Stone–Wales defect. It can be viewed as a combination of Stone–Wales defect with an inverse Stone–Wales defect. A periodic arrangement of this defect structure has been proposed to form a new carbon allotrope, called Haeckelite [190]. The ground state energy of such an allotrope was calculated

Table 3
Summary of defect formation energies in graphene based on DFT calculations.

	Formation energy (eV)	Number of missing or additional carbon atoms	Figure	Reference
Stone–Wales defect	4.5–5.3	0	14(a)	[178,179,181]
Single vacancy	7.3–7.5	−1	14(c)	[177]
Divacancy 1	7.2–7.9	−2	14(d)	[177,185]
Divacancy 2	6.4–7.5	−2	14(e)	[186,187]
Divacancy 3	7	−2	14(f)	[174]
Grain boundary loop (13 atom core)	9.3	0	15(a)	[181]
Grain boundary loop (24 atom core) 'flower defect'	7.0	0	15(b)	[181]
Grain boundary loop (54 atom core)	19.9	0	13(c)	[181]
Inverse Stone–Wales defect	5.8	+2	14(a)	[189]
Stone–Wales + inverse Stone–Wales defect	6.07	+2	14(b)	[188]

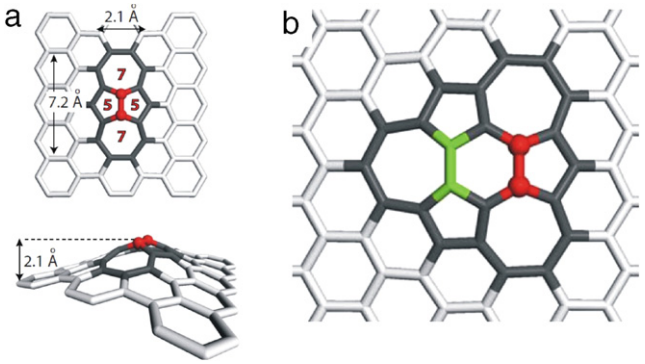

Fig. 16. DFT-simulations of defect structures in graphene with two extra carbon atoms. (a) the 'inverse Stone–Wales' defect, causing a distortion of the graphene lattice, and (b) a combination of a regular Stone–Wales defect (green bond) and an 'inverse Stone–Wales 'defect. (For interpretation of the references to colour in this figure legend, the reader is referred to the web version of this article.)
Source: Reproduced from Ref. [188].

to be 229 meV/atom above the energy of graphene, which has been stated to be lower than the energy for C_{60} molecules with 360 meV/atom above the energy of graphene [189]. Nevertheless, it seems challenging to stabilize such a structure and avoid energy minimization by forming graphene sheets. So for now, the Haeckelite structure is purely hypothetical. A summary of defect structures and their calculated formation energies is given in Table 3.

4.1.2. Properties of point defects

Experimental studies of electronic and chemical properties of controlled point defects in graphene are very rare. This is because of the low concentration of defects in graphene and the possibility of the presence of multiple types of defects. This requires local probe techniques like STM or TEM to investigate defect specific properties. TEM studies were used to create defects and to investigate the interaction of metal adatoms with these defects [186]. It was found that the reconstructed vacancies acted as trap sites for metals. Computational studies [191,192] have shown that defects should be much more reactive for adsorption of hydroxyl, carboxyl or other groups. Recent studies have shown that perfect graphene, i.e. without pre-existing defects, can also be covalently functionalized, however, in the functionalization process defects are being generated [193].

The electronic properties of defective graphene have been thoroughly investigated theoretically, see for example Ref. [194] for a review. Experimentally the challenge of investigating the electronic properties of individual defects in graphene is obviously more challenging. STM images of vacancies on a graphite (HOPG) surfaces may appear as bright protrusions which are interpreted as defect induced localized states near the Fermi level which may also be responsible for magnetic moments in defective graphene [195]. DFT calculations showed the formation of a band gap at Stone–Wales defects [196] and at vacancy type defects [197] of up to 0.3 eV. Overall there is an acute lack of reliable experimental investigations of defect structures and their properties in graphene. This lack of experimental studies of electronic or chemical properties of defects reflects the challenges in preparing well defined defect structures in unsupported or on weakly interacting supports, which would give access to their investigation by e.g. scanning tunneling spectroscopy.

4.2. Nitrogen or boron substitution in graphene

Traditional doping of semiconductors is done by impurity doping. This approach is more difficult in 2D materials but doping of graphene with elements adjacent to carbon in the periodic table, i.e. boron and nitrogen, has been demonstrated. In this case the group III element boron introduces a hole, i.e.it acts as a p-type dopant, while the group V element nitrogen donates an electron and thus acts as an n-type dopant.

Boron doping has been accomplished by using diborane (B_2H_6) as a precursor [198]. XPS showed that the boron was incorporated in the sp^2 carbon network with a doping level of 1.2%–3.1%. A p-type doping with the Fermi level 0.65 eV below the Dirac point has been suggested from DFT calculations.

Nitrogen doping can be achieved by several means. Ammonia [199], or pyridine [200] have been used as dopant precursors during CVD growth. It has also been shown that ammonia [201] or nitrogen plasma [202,203] can introducing N-dopants in the graphene lattice post growth. Even the exfoliation of graphene from graphite in an N-atmosphere has been claimed to produce N-doped graphene [204]. In addition, two step approaches consisting of defect formation by ion bombardment and subsequent annealing in ammonia atmosphere have been demonstrated. It is proposed that in the annealing step carbon-vacancies are healed by N-incorporation [205]. Doping levels as high as 8.9% nitrogen have been reported during CVD growth and the N-concentration can be controlled by adjusting the ammonia to CH_4 ratio in the feeding gas [199]. Edge doping of graphene ribbons has also been reported by annealing graphene ribbons in an ammonia gas [206]. Both in-plane substitutional doping as well as edge doping have shown n-type behavior of the graphene. In addition to the doping effect an opening of a band gap in N-doped graphene has been reported [199]. The charge re-distribution around the N-dopant in graphene has recently been observed by high resolution TEM [207]. The electron distribution in carbon atoms next to a nitrogen dopant is significantly disturbed causing differences in the electron scattering and consequently contrast-differences in high resolution TEM images. To the best of our knowledge, no STM/STS studies of doped graphene have been reported to date. STS in particular would be very powerful to obtain information on the influence of dopants on the local electronic structure.

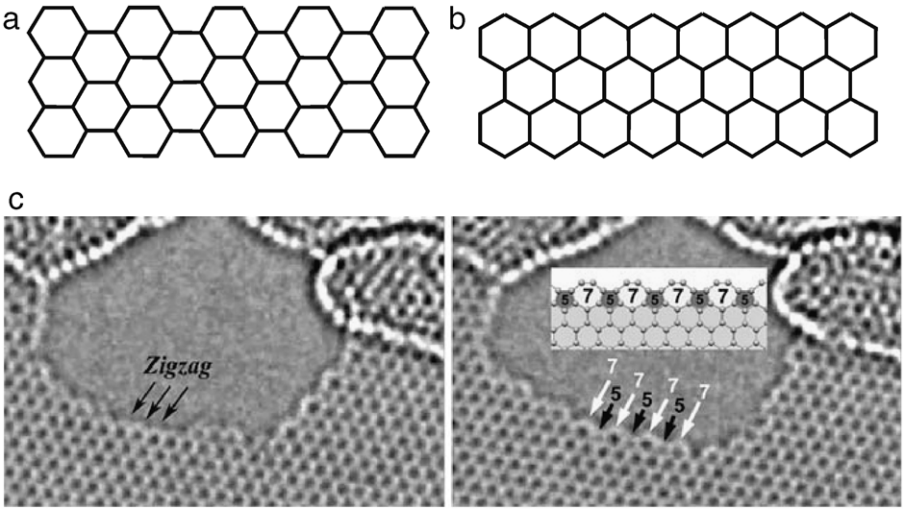

Fig. 17. Graphene edge structures. An ideally terminated edge is either of armchair (a) or zigzag (b) type. The zigzag edge easily reconstructs as the TEM images in (c) demonstrate. Under the electron beam of the TEM the initially zigzag edge restructures into alternating 5- and 7-fold rings.
Source: Reproduced from Ref. [210].

4.3. Free graphene edges

As mentioned above, an important way of inducing a band gap in graphene is by quantum confinement of electrons in narrow graphene ribbons. The formation of band gaps in graphene is one of the main requirements for using graphene in FETs. Making graphene ribbons necessitates the formation of graphene edges. The structure and chemical termination of these edges influence the charge carrier transport and device operation [208,209] and therefore understanding and controlling of graphene edges is of technological significance.

Two basic, achiral graphene edge structures can be differentiated. Depending on along which low index direction the graphene sheet is cut we obtain either a 'zigzag' or an 'armchair' edge. These different edges are illustrated in Fig. 17(a) and (b). Chiral edges are obtained by cutting the graphene sheet along a non-low index direction. It has been demonstrated that Joule-heating or electron beam irradiation evaporates edge atoms and contaminations and preferentially generates step edges of the achiral type [211]. It has been proposed based by computational studies, that zigzag edges are metastable and that they should spontaneously restructure into pentagons and heptagons [212]. Such a restructuring of zigzag edges has been, for example, observed under electron irradiation in a TEM [210] as shown in Fig. 17(c). Recent advances in STEM now allows to measure electron energy loss near edge fine structure for individual carbon atoms. This enables characterization of bonding of edge atoms, but the electron beam may modify the edge structure [213]. Scanning tunneling microscopy and spectroscopy, on the other hand, is less intrusive and STM/STS has been used to characterize the electronic structure of edges [214–216]. Electronic edge states had been predicted more than 15 years ago before it was conceivable that well defined graphene ribbons could be synthesized [217]. For armchair and zigzag ribbons distinctively different electronic edge states are present. Zigzag edges exhibit localized electronic states at the Fermi level with almost flat bands while no such states are observed for armchair edges [217]. The metallic character of zigzag edges has been verified by STM/STS measurements and a decay of the edge state into the interior of graphene with a decay length of 1.0–1.2 nm was found [214]. The edge states of chiral graphene edges have also been recently measured. Well defined chiral edges were obtained by un-zipping carbon nanotubes. The obtained graphene nanoribbons were supported on Au(111) surface which enabled STM and STS measurements at low temperatures. The Au-supported ribbons are shown in Fig. 18 [215]. The graphene ribbons exhibited a region of topographic curvature at the terminating edges of about 3 Å in height and 30 Å lateral extension (see cross-section in Fig. 18(b)). STS along these edges confirmed theoretical prediction of a 29 meV band gap in the flat-band edge states. These edge states exhibited a decay into the graphene ribbon with a 1.2 nm decay length. Also spatial oscillation of the edge-state amplitude was observed. This oscillation has been attributed to the 'kinks' in the zigzag edge structure that gives the chiral character to the edge (see Fig. 18(a)). Furthermore, it has been suggested that an energy-split in the spectroscopic peaks indicate the formation of spin-polarized edge states at these chiral edges.

In most practical applications, the graphene edges are not pristine but easily react during or post ribbon fabrication. This leads to oxygen, hydrogen, hydroxyl, or other contamination at the edge. On the positive side the reactivity of graphene edges may enable a controlled functionalization with desired chemical groups. Hydrogen terminated step-edges on HOPG were characterized by STM where a prevalence of armchair edges was found. At zigzag edges, edge-states were found [218]. More atomic scale studies or controlled functionalization of edges would be desirable to better understand the edge chemistry and the potential of tuning graphene nanoribbon properties by edge decoration.

4.4. Grain boundaries

Grain boundaries in HOPG are rare, but have been observed by STM [219]. Because HOPG is essentially a single grain, exfoliated graphene usually does not exhibit grain boundaries. On the other hand, graphene grown by CVD on copper and other weakly interacting metal substrates usually exhibits different rotational grains and therefore grain boundaries must be present. These 1D defects strongly affect graphene properties such as charge transport [220]. As discussed for the growth of graphene on metals, in Section 2, the orientational relationship with respect to the metal substrate depends on the interaction of the graphene with the metal. On weakly interacting metals, different rotational-domains can nucleate and grown even on single crystal metal

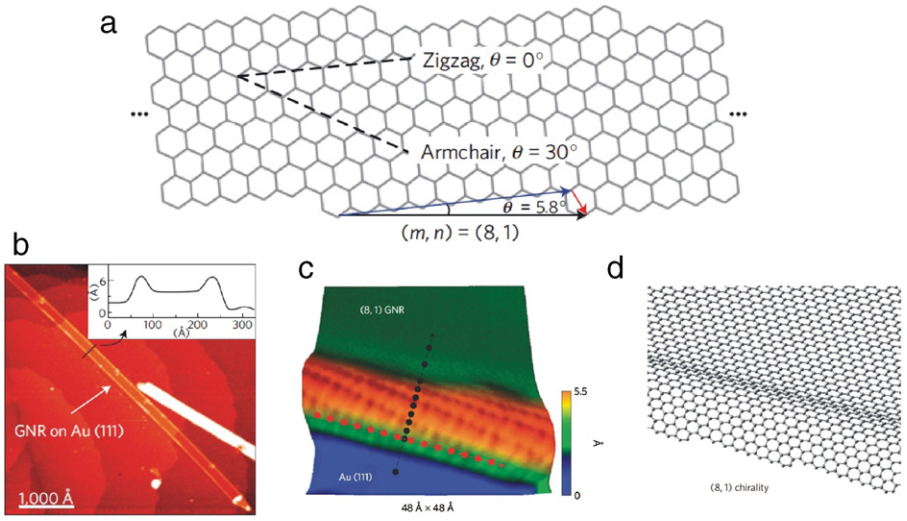

Fig. 18. Chiral graphene nanoribbon created by unzipping of a carbon nanotube and supported on a Au(111) surface. The edge structure of the chiral ribbon is schematically shown in (a). STM images of the supported ribbons are shown in (b) and (c). The edges of the ribbon are 'bulging' as shown in the line scan in the inset in (b) and the pseudo-3D view in (c). The structure of the bulged edge is shown in (d).
Source: Reproduced from Ref. [215].

substrates. This implies the formation of grain boundaries, whose density is determined by the nucleation density of graphene. The existence of grains with different orientation can be determined by electron diffraction with high spatial resolution as is possible for example by LEEM [85,221,222] for supported graphene or TEM for free-standing graphene [223–225]. By using pre-patterned growth seeds, graphene nucleation and therefore grain boundary formation can be controlled to some extend [220].

STM studies of graphene grown on Ir(111) have revealed (tilt) grain boundaries [51]. As in bulk materials these boundaries can be described by a linear array of edge dislocations (with the (imaginary) dislocation line normal to the graphene sheet). As shown in computer simulations a single dislocation core can be constructed from a heptagon and a pentagon ring or pairs thereof to obtain zigzag or armchair oriented tilt grain boundaries, as shown in Fig. 19(a)–(f) [226,227]. The orientation and position of these rings determine the Burgers vector of the dislocation and the separation of these dislocations in a periodic arrangement determines the tilt angle in a grain boundary. Somewhat surprisingly, atomistic calculations showed that the strength of the graphene sheet is only reduced for small-angle tilt boundaries while large angle boundaries exhibit the same strengths as pristine graphene [226]. The arrangement of pentagons and heptagons does not just allow the construction of regular tilt boundaries but are also used to 'stitch' together arbitrarily tilted grains as have been shown by high resolution TEM studies and is shown in Fig. 19(g) and (h) [223].

A special kind of domain boundary, which does not require any tilt rotation of two graphene sheets, has been constructed on a Ni(111) support [71]. Graphene can grow on the lattice matched Ni-substrate with two different adsorption structures due to similar adsorption energies for every second carbon atom in fcc- or hcp-hollow sites, i.e. the adsorption energies for the structures shown in Fig. 1(b) and (c) are very similar for graphene on Ni(111). These two adsorption structures and the resulting domain boundary are illustrated in Fig. 20(a). If the two domains meet, the graphene sheets do not match. Consequently the interface has to restructure into a pair of pentagons and an octagon as is evident from STM images shown in Fig. 20(b). This defect line is periodic and straight since it can only form along one crystallographic direction of the graphene. This line defect has electronic properties very similar to zigzag graphene edges, i.e. it has flat bands at the Fermi-level which gives it a metallic character. Furthermore, as is the case of free edges, the metallic states decay exponentially into the neighboring graphene lattice. This can be observed as an increased contrast in STM images surrounding the defect line (see Fig. 20(c)). Because the two graphene domains are not rotated relative to each other, this defect exhibits unique properties. It has potential applications as metallic wires within a graphene wafer, or by exploiting its electron scattering behavior which may enable highly efficient valley filtering [228]. The main obstacle for the utilization of extended line defects is, however, the challenge in a controlled fabrication of defects.

Heteroboundaries. The formation of in-plane boundaries between graphene and other 2D materials open the possibility of creating new hybrid materials. In Section 2.2.3 we have discussed the growth of graphene on Ni(111) in the presence of a Ni_2C surface carbide phase [73]. In this case a sharp lattice matched interface has been observed, which may be interpreted as in-plane heteroboundary of two 2D materials. However, the Ni_2C phase can only exist as a surface phase on top of bulk Ni and thus cannot be prepared as a free-standing material. Nevertheless, these kinds of in-plane interfaces may be useful to tune metal–graphene contacts.

Potentially more interesting are interfaces between truly 2D materials, such as graphene and hexagonal boron nitride (*h*-BN). These two materials have largely different electronic properties (*h*-BN has a 5.9 eV band gap) but are closely lattice matched. Simultaneous growth of graphene and *h*-BN by CVD on a Cu-foil resulted in a phase-separated growth of graphene and *h*-BN domains in the same lattice plane with lattice matched edges [229]. In the synthesized films the graphene forms a percolation network and transport measurements indicated a band gap opening of 18 meV. This band gap was interpreted as a consequence of quantum confinement of the electrons in graphene by the wide band-gap *h*-BN that surrounds the graphene network. Thus graphene/*h*-BN hybrid materials may be used to induce a band gap in graphene and if the interfaces and sizes of the graphene domains can be controlled then this may provide an alternative material to nanoribbons for field effect transistors.

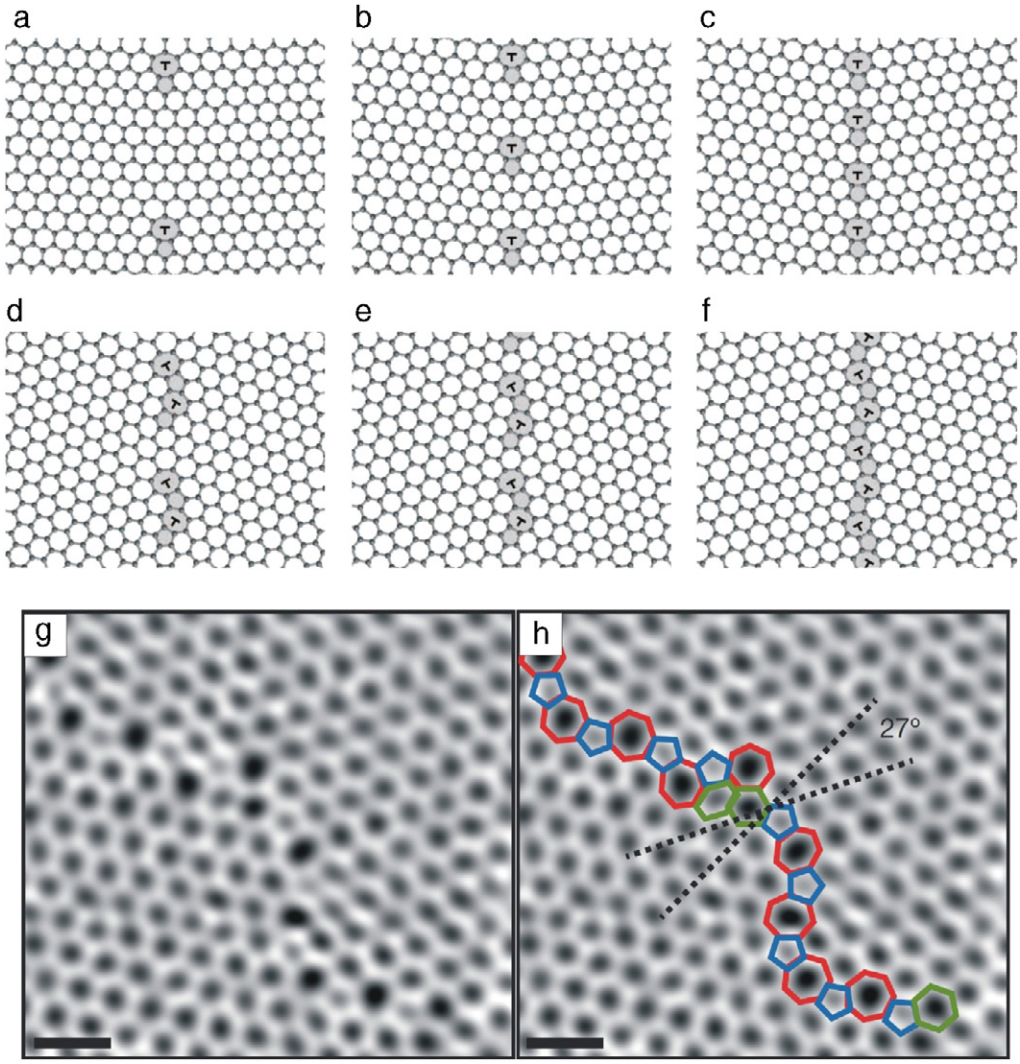

Fig. 19. Structure of tilt grain boundaries for zigzag-oriented (a)–(c) and armchair oriented (d)–(f) graphene sheets with various rotation angles. High resolution TEM of randomly oriented grain boundary with a tilt rotation of ∼27° between graphene sheets is shown in (g) and (h).
Source: (a)–(f) reproduced from Ref. [226].

Source: (g) and (h) reproduced from Ref. [223].

5. Chemically modified graphene: graphane, fluorographene, and related materials

Local chemical modifications of graphene may be another approach to pattern extended graphene sheets. The chemical surface modifications and the formation of graphene with hydrogen or fluorine have been of particular interest. Graphane is a theoretically predicted compound with one hydrogen atom attached to each carbon atom on alternating sides of the graphene sheet [230]. According to computational results graphane is a wide-band gap semiconductor, whereas a half-hydrogenated graphene would have a modest band gap of 0.43 eV [231]. Graphene membranes exposed to atomic hydrogen exhibit a compressed lattice compared to pure graphene and this was taken as evidence for the existence of graphane [232]. Hydrogen from hydrogenated graphene could, however, easily be desorbed at moderate temperatures suggesting that it is not a very stable compound. Hydrogenation of graphene by atomic hydrogen in UHV on graphene supported on SiC [233,234] as well as on Ir(111) [235] was also demonstrated. In the case of supported graphene only one side of the graphene can be exposed. The adsorbed hydrogen was stable in STM imaging at room temperature. Also, a depletion of the electronic states surrounding a hydrogen adsorbate was found from STS measurements [236]. Furthermore it has been demonstrated that the STM tip may be used to remove adsorbed hydrogen from the surface if the bias voltage is increased to +4.5 V. Scanning the surface under these conditions therefore allows patterning of the surface at the nanometer scale [233]. Hydrogen adsorption on the moiré pattern of graphene on Ir(111) is shown in Fig. 21 for increasing hydrogen exposures [235]. This demonstrates that the hydrogen adsorption leaves the moiré structure intact and hydrogen preferentially adsorbs at specific atom sites within the moiré structure. DFT calculations reveal similar mechanisms for hydrogen adsorption as for Ir-cluster adsorption, which we have discussed in Section 2.3. Hydrogen adsorbs strongest in regions where every other carbon atom is on top of substrate Ir-atoms (i.e. structure shown in Fig. 1(b) or (c)). In this case hydrogen adsorbs on carbon atoms located close to the three-fold hollow sites in the substrate. In this case the carbon can re-hybridize from sp^2 to sp^3. Consequently, the moiré-pattern of graphene on Ir(111) acts as a template for nanopatterned hydrogen adsorption. In the hydrogenated areas, a

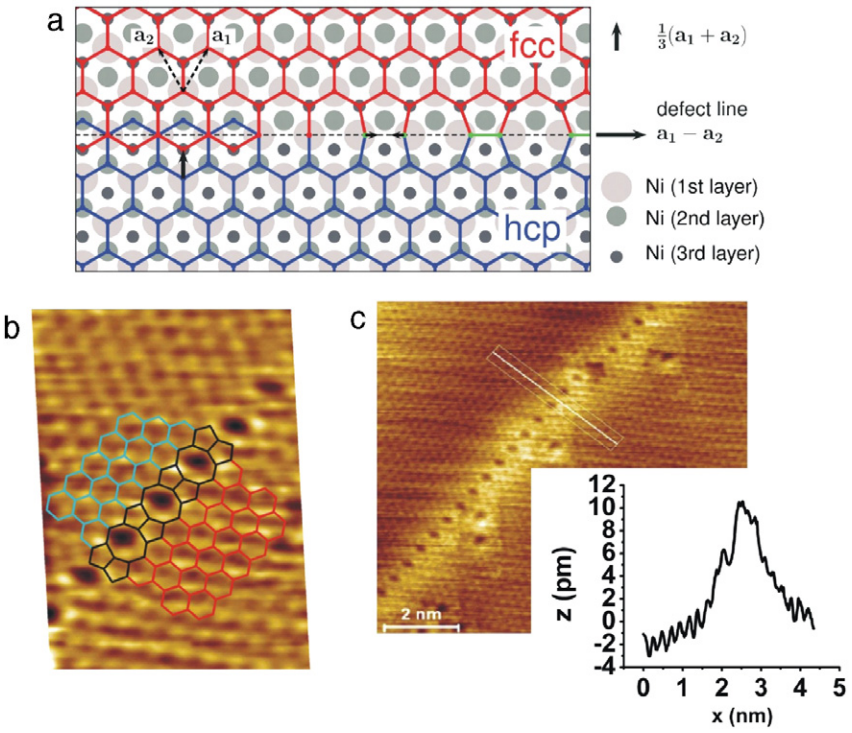

Fig. 20. Domain boundary of graphene sheets translated by a fractional unit cell vector. This structure is formed on a Ni(111) substrate where graphene can adsorb with two adsorption geometries as schematically shown in (a). STM images in (b) and (c) show the structure of the domain boundary and the increased contrast surrounding the defect in (c) is attributed to exponential decaying defect electronic states at the defect line. A cross-section that indicates this exponential decay is shown in the inset of (c).
Source: Reproduced from Ref. [71].

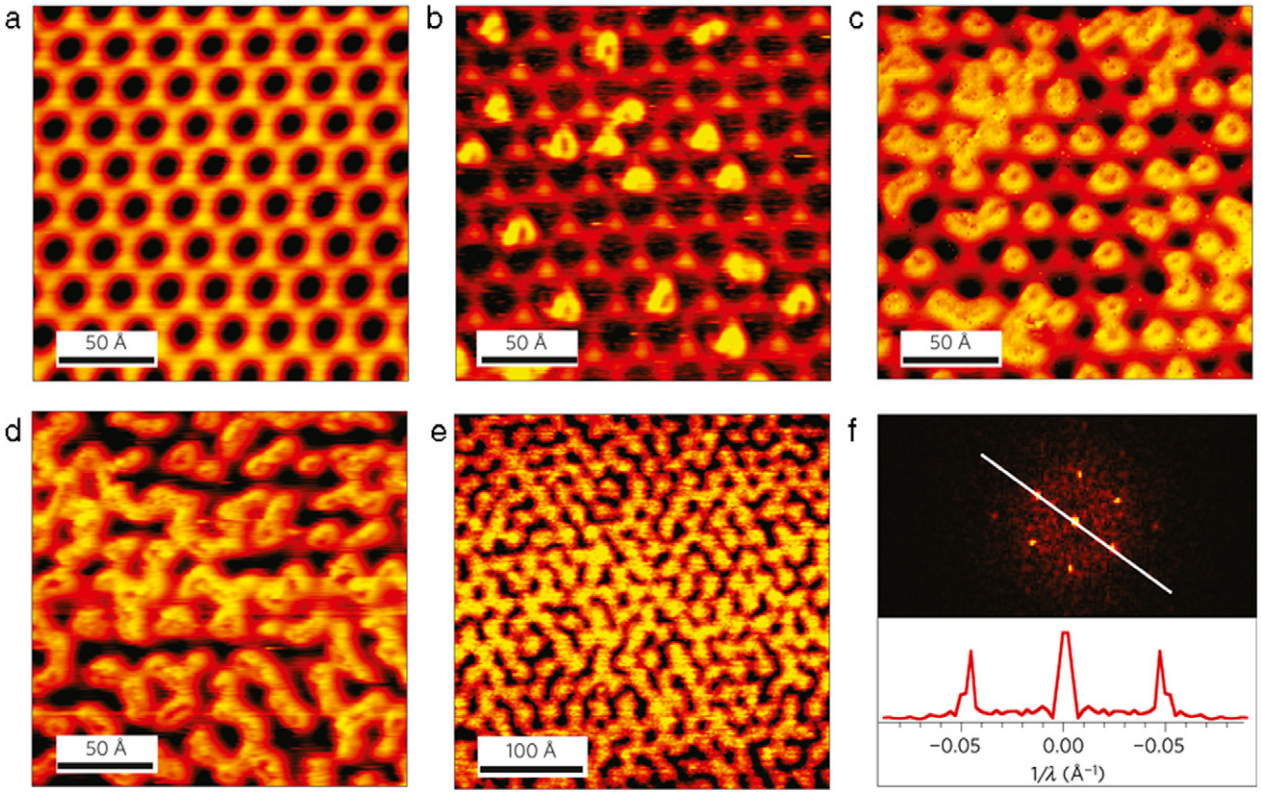

Fig. 21. STM images of hydrogen adsorption on graphene supported on Ir(111). The moiré structure of the pristine graphene is shown in (a). (b)–(e) show the surface structure with increasing atomic hydrogen exposure. It is apparent that hydrogen adsorbs preferentially in the depressions of the graphene-moiré structure. Even at high exposures the periodicity of the moiré structure is preserved as the Fourier transform of the STM image demonstrates (f).
Source: Reproduced from Ref. [235].

wide band gap opens which causes quantum confinement effects in the pristine graphene. ARPES shows a down-ward shift of the top of the π-band to 450 meV below of the Fermi-level as a consequence of this confinement. This demonstrates that chemical patterning of graphene can be used to modify electronic properties, such as opening of defined band gaps, and this may yet be another alternative to nanoribbon formation.

Graphene oxide [237] is an important chemical derivative of graphene. It is essentially a graphene sheet with densely but randomly distributed hydroxyl and epoxy groups which may be formed by exposure of graphite to a liquid oxidizing agent. Graphene oxide may be quite inhomogeneous with regions that appear to be almost pristine graphene and regions that are densely decorated with functional groups [238]. Atomic oxygen adsorption on graphene supported on Pt(111) or Ir(111) has also been recently studied by NEXAFS, XPS, and STM [239]. Adsorption was found to predominantly occur through covalent bonding to C–C entities, i.e. epoxy group formation. Similar to the case of hydrogen on Ir(111) the initial adsorption is in regions of the moiré-pattern where the graphene can be easier re-hybridized from sp^2 to sp^3. Upon annealing, these regions are more susceptible to etching. Consequently, formation of holes in the graphene sheet has been observed preferentially in pre-defined areas of the moiré-structure. This, therefore, may be an approach to utilize the moiré-pattern as a template to create graphene with a high density of holes on the nanometer scale. Such a 'holy' graphene sheet would exhibit electron confinement induced band-gap opening similar to graphene nanoribbons and thus may be a quite useful material for microelectronic applications.

One shortcoming of hydrogenated graphene, or graphane, is its low (thermal) stability. An alternative to hydrogen may be fluorine to form a more stable material. Different approaches have been used to obtain stoichiometric fluorographene (CF). One approach is the exfoliation of graphite fluoride [240], a 3D compound used in batteries or as a lubricant. However, this exfoliation process is difficult and has been demonstrates to result in highly defective layers. An alternative process is the fluorination of graphene by exposure to XeF_2 [241,242]. It is worth mentioning that graphene is stable for exposure to F_2 at room temperature and therefore molecular fluorine cannot be used for graphene fluorination. However, exposure of graphene to XeF_2 resulted in the formation of fluorographene. It is a mechanically stable material with properties rivaling those of graphene with a measured Young's modulus of 100 N m^{-1}. Furthermore, it was found to be thermally stable up to 400 °C even in air. Electronically, fluorographene is an excellent insulator with an optical band gap of 3 eV [241]. It was hypothesized that the insulating property of fluorographene may enable patterning of graphene with quantum confinement structures as shown for hydrogen or to form electrical circuits on a graphene sheet and tunneling barriers made of narrow fluorographene strips.

In conclusion, chemically modified graphene is an approach to transform graphene into an insulator. If such modifications can be localized on a graphene wafer then this may be a method to pattern graphene, i.e. forming insulating and semiconducting regions on a wafer. By forming narrow regions of pristine graphene the band gap can be tuned by defining the width of the quantum confinement region. To further enhance the flexibility of such wafers a method for doping graphene needs to be developed. One such approach, by charge transfer doping, is discussed in the next chapter.

6. Molecular adsorption on graphene

For many electronic applications it is a prerequisite to control the doping of graphene, i.e. to make graphene p- or n-type by shifting the Fermi-level up or down from the Dirac point. Substitutional dopants such as B or N as discussed in Section 4.2 strongly affect charge carrier mobility in graphene and as of yet have to be better controlled. An alternative mechanism for shifting the Fermi-level, which is particular attractive for 2D materials like graphene, is to bring graphene in contact with other materials. Above we have seen that metal contacts can cause such a shift in the Fermi-level due to differences in the work function (see Fig. 6). An alternate and more versatile approach compared to metals is doping graphene by bringing it into contact with electron donating or accepting organic molecules. Molecules adsorbed on graphene can, depending on their functional groups, withdraw or donate electrons into graphene, effectively doping it p- or n-type, respectively. This doping mechanism can also be exploited for gas sensing applications, where adsorption of molecules may result in conductivity changes [243]. For instance adsorption of NO_2 causes electron withdrawal from graphene (i.e. leaving holes behind), because the lowest unoccupied molecular orbital (LUMO) of adsorbed NO_2 is about 0.4 eV below the Dirac point of graphene [244]. Opposite gas response is observed for adsorption of ethanol and ammonia [243], suggesting an electron transfer from these molecules toward graphene. To increase the selectivity of graphene as a gas sensor some efforts are currently underway to functionalize graphene, for example with DNA strands that can be tuned to adsorb specific molecules.

Another significant application of graphene is its use as a transparent electrode. Graphene only adsorbs 2.3% of the light intensity from infrared-to-visible light per graphene monolayer [245]. This low light absorption combined with its high conductivity makes it ideally suited for many applications ranging from touch screens to optoelectronics and solar cells. Organic-electronics is an important subsection of these applications and therefore the organic–graphene interface is of interest for optimizing charge injection from the graphene-electrode into the organic film. Therefore, a fundamental understanding of organic/graphene interfaces is also desirable for transparent electrode applications.

In the next sub-section we concentrate on charge transfer doping as a mechanism of p- and n-type doping of graphene, followed by fundamental studies of ordered molecular overlayer structures on epitaxial graphene.

6.1. Charge transfer doping

Charge transfer doping processes at semiconductor interfaces (including graphene) has been reviewed recently [246]. Graphene can be charge doped if brought into contact with elements or molecules that easily donate or accept electrons. Alkali atoms, for instance, can be used to n-type dope graphene as these elements easily give up their electrons. Alkali atom deposition has been, for example, used to shift the Fermi-level up to investigate the presence of a band gap in graphene in photoemission experiments. This is especially useful if the graphene is otherwise p-doped (e.g. if in contact with a metal as discussed above) and thus the Dirac point is above the occupied states and therefore could not be observed by photoemission without n-type dopants [57,247].

For p-type doping, electron accepting molecules are needed. Fig. 22 shows the split between the highest occupied molecular orbital (HOMO) and lowest unoccupied molecular orbital (LUMO) referenced to the vacuum level in comparison to the Fermi-level of graphene, assuming a graphene work function of 4.6 eV [248]. It is apparent that the LUMO of tetrafluoro-tetracyanoquinodimethane (F_4-TCNQ) and $C_{60}F_{48}$ are below the Dirac point of graphene and therefore if brought into contact, electrons should be transferred from the graphene to these molecules. On the other hand, adsorption of weaker electron acceptor molecules like e.g. C_{60} should not result in significant charge transfer and thus

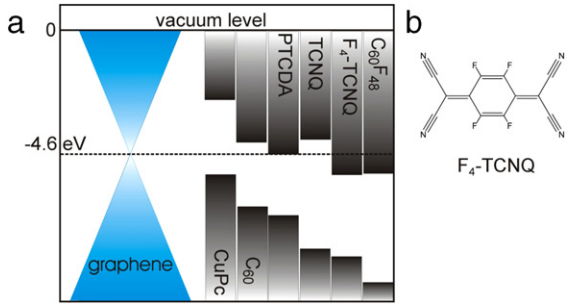

Fig. 22. Energy levels of typical electron accepting molecules referenced to the vacuum level (0 eV) (a). The work function of graphene is set to 4.6 eV, i.e. identical to that of graphite. The LUMO of F_4-TCNQ and $C_{60}F_{48}$ are below the Dirac point of graphene indicating electron transfer from graphene to these molecules if brought into contact. The HOMO–LUMO splitting and ionization potentials for the molecules have been taken from Ref. [246]. The molecular structure of F_4-TCNQ is illustrated in (b).

these molecules are not efficient p-type dopants. This has been demonstrated by photoemission experiments [249].

Several experiments have been conducted for p-type charge transfer doping of graphene with F_4-TCNQ [249,250]. These studies have been performed on epitaxial graphene mono- and bi-layers on SiC(0001). Although, we are not reviewing SiC literature in this article, in this case we make an exception since similar conclusions reached for charge transfer doping on graphene/SiC should also hold for other substrate materials and thus is not SiC specific. Monolayer epitaxial graphene (monolayer refers to the second graphene layer above a strongly interacting graphene buffer layer) is natively n-type doped due to the charge transfer from the SiC substrate. The doping level in graphene can be elegantly monitored by ARPES. Measuring the π-band dispersion around the *K*-point of the graphene Brillouin zone allows an accurate determination of the Fermi-level relative to the Dirac point. For example, the native n-type doping of monolayer graphene on SiC(0001) can be seen by the upward shift of the Fermi-level of 0.42 eV above the Dirac point, see e.g. Fig. 23(a). Vapor deposition of F_4-TCNQ compensates for the substrate induced n-type doping. Fig. 23(b)–(e) shows ARPES data with increasing F_4-TCNQ film thickness. For a thickness of 0.8 nm the Fermi-level in graphene is at the Dirac point. Increasing the F_4-TCNQ thickness further, does not result in a further charge transfer indicating that the charge transfer is saturated at 0.8 nm. Additional information of the charge transfer process and molecular alignment comes from N-1s and F-1s core level photoemission spectra, shown in Fig. 23(f) and (g), respectively. Somewhat surprisingly the F-1s peak does not change with increasing F_4-TCNQ film thickness, suggesting that it is not the fluorine that accepts the charges. On the other hand, the N-1s peak has to be fitted to three peaks, which have been assigned to an N^{-1}, an N^0 and a shake-up peak. The appearance of the N^{-1} peak suggests that the charge transfer takes place through the C $\equiv$ N group and the fluorine remains passive. Only at low coverage does the charged N^{-1} species dominate. In between 0.4 and 0.8 nm film thickness the ratio between uncharged and charged is about 45% indicating that only about half of the cyano groups contribute in the charge transfer for densely packed films. This may be understood by the F_4-TCNQ molecules standing upright on the graphene surface as illustrated in Fig. 23(h). In this case only half of the cyano groups make contact with the graphene and contribute to the charge transfer [250]. Angle dependent NEXAFS measurements by other investigators have, however, concluded that the F_4-TCNQ molecules lie flat with the F_4-TCNQ plane parallel to the graphene [246]. Thus there remains some controversy regarding the molecular orientation. P-type doping of graphene was also reported for other molecules, for instance for tetrasodium 1,3,6,8-pyrenetetrasulfonic acid (TPA) [251]. First-principle calculations suggest that tetracyanoethylene (TCNE) may also act as an efficient p-type dopant [252].

Molecular adsorption of charge donating or accepting molecules clearly has the potential to be used for doping graphene. One main advantage of this process is that the integrity of the graphene is preserved and charge donation may not strongly affect the charge carrier mobility like substitutional dopants do. Furthermore, by appropriate patterning of the organic dopant film on graphene one can envision to modify the doping and create p–n junctions and other structures in graphene.

6.2. Ordered (self-assembled) organic monolayers

As mentioned above there exists some controversy about the orientation of F_4-TCNQ molecules on graphene. STM studies of graphene grown on Ir(111) (in contrast to the epitaxial graphene on SiC(0001) discussed above) showed that F_4-TCNQ lies flat on the surface, at least for submonolayer coverage [253]. Fig. 24(a) shows an STM image of the ordering of F_4-TCNQ on graphene on Ir(111) at 77 K sample temperature. At this temperature the molecules appear with a circular, toroidal shape. This is attributed to a rotation of the molecule around its axis. The location of the molecules are defined by the moiré-pattern of graphene on Ir(111) (see Section 2.1.2). From the STM studies it was concluded that the F_4-TCNQ adsorbs in areas of the moiré-pattern that exhibits hcp-stacking relative to the Ir-substrate. The dominance of the moiré-structure for ordering of the F_4-TCNQ molecules is contrasted by the adsorption of TCNQ shown in Fig. 24(b). For TCNQ intermolecular forces dominate the adsorption structure resulting in a close packing of the molecule at the same surface. The difference in the ordering of these two related molecules has been attributed to electrostatic repulsive forces due to negative charges on the fluorine and cyano groups of F_4-TCNQ (see Fig. 22(b) for molecule structure). Alternatively, the author of this review proposes that the repulsive electrostatic interaction actually originates from the charge transfer from graphene to F_4-TCNQ and thus the difference in ordering of the molecules may represent the different amount of charge transfer doping.

The moiré-structure formed for graphene on Ru(0001) (see Section 2.1.1) has also been used as a template to arrange molecules in unique patterns. Phthalocyanines (molecules with a single metal ion in the central position of a macrocycle consisting of alternating carbon and nitrogen atoms) have been arranged in a Kagome lattice aided by the moiré-structure [254]. A Kagome lattice is a two-dimensional pattern composed of interlaced triangles whose lattice points have four neighboring points each. This is the most geometrically frustrated magnetic system [255] and is only rarely experimentally observed. The Kagome lattice structure on graphene/Ru(0001) is shown in Fig. 25.

A strong influence of the moiré-structure of graphene on Rh(111) (see Section 2.1.6) on the ordering of perylene tetracarboxylic diimide (PTCDI) has also been reported [256]. A commensurate match between the molecule and the moiré structure was suggested to result in alignment of molecules into extended one-dimensional chains. No such structures have been formed on HOPG of the same molecule thus illustrating the importance of the moiré structure in molecular ordering. A related molecule, perylene-3,4,9,10-tetracarboxylic dianhydride (PTCDA) has been grown on graphene on SiC(0001). In this case, *no* alignment of the molecules was observed, but rather a dense packed surface overlayer was obtained [257,258]. In general π-conjugated planar molecules can interact with graphene via π–π interactions, possibly favoring flat-lying molecules. Flat lying pentacene was observed on clean graphene while for graphene 'contaminated' with polymer residues remaining from a lift-off process caused pentacene to stand upright [259]. The upright configuration is preferred for organic FET applications and thus modification of the

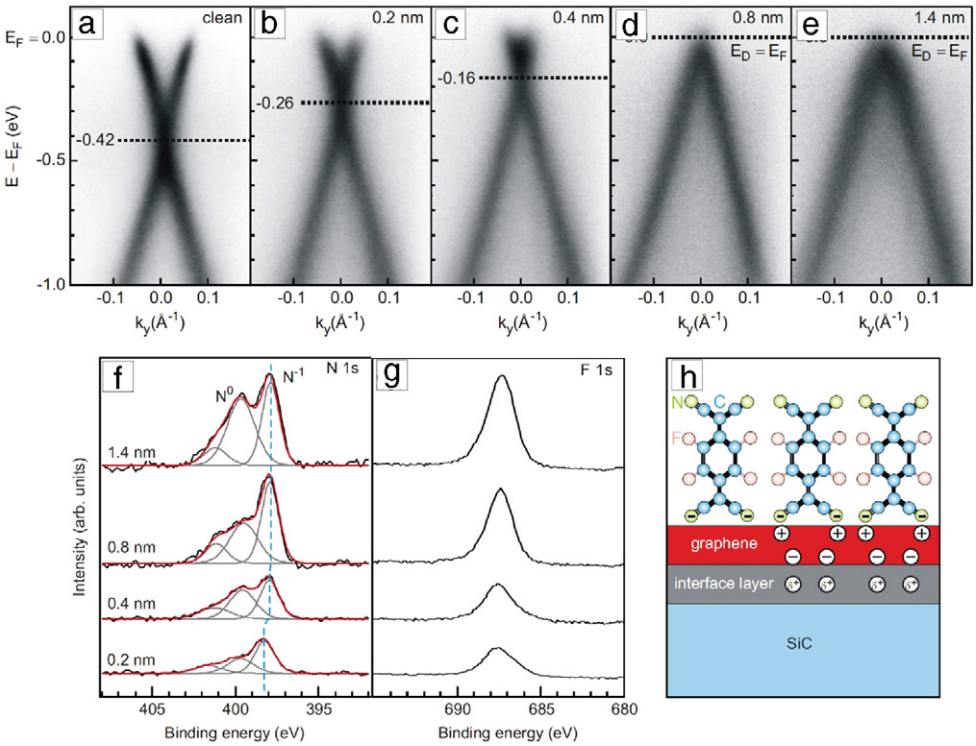

Fig. 23. F_4-TCNQ adsorption on monolayer graphene on SiC(0001). ARPES spectra of the π-bands around the K-point of the graphene Brillouin zone for increasing F_4-TCNQ film thickness: (a) pristine graphene/SiC(0001) showing substrate induced n-type doping with the Fermi-level shifted by 0.42 eV relative to the Dirac point, (b) 0.2 nm, (c) 0.4 nm, (d) 0.8 nm, and (e) 1.4 nm thick F_4-TCNQ film. The Fermi level shifts downward up to a film thickness of 0.8 nm. At 0.8 nm the charge transfer from graphene to F_4-TCNQ is saturated and no further doping can be obtained beyond this film thickness. (f) and (g) show XPS core level spectra of N-1s and F-1s respectively for increasing F_4-TCNQ film thickness. A schematic charge transfer model derived from the XPS peak intensities is illustrated in (h).
Source: Reproduced from Ref. [250].

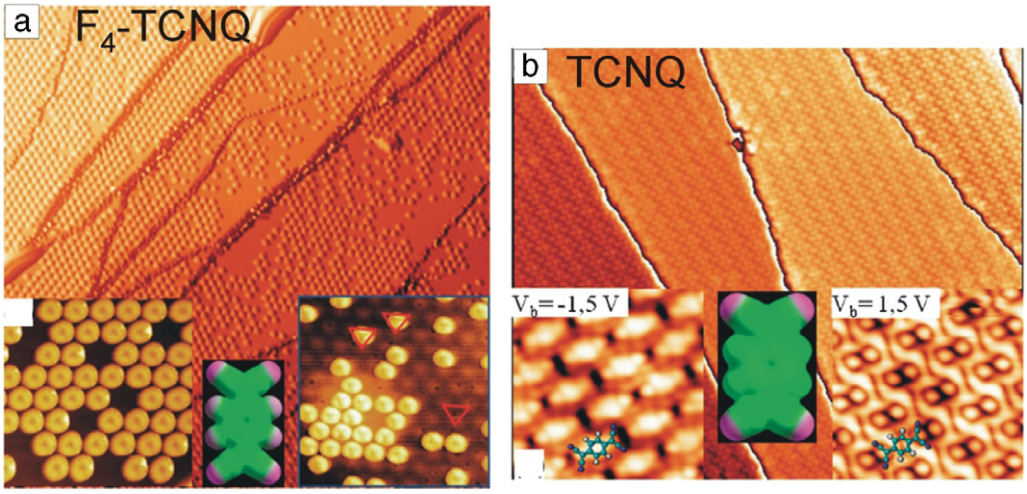

Fig. 24. STM images of molecular ordering of F_4-TCNQ (a) and TCNQ (b) on graphene/Ir(111). Repulsive interactions between F_4-TCNQ molecules results in ordering facilitated by the substrate moiré-pattern, whereas dominant intermolecular forces result in close packing of the TCNQ molecules, with no apparent influence of the substrate.
Source: Reproduced from Ref. [253].

graphene with organic residues can have beneficial effects for device fabrication.

Linear phosphonic acid molecules (octadecylphosphonic acid and tetradecylphosphonic acid, i.e. a phosphonic headgroup attached to an alkyl chain terminated by a methyl group) have been shown to arrange themselves in flat 2D lattices with the molecules aligning along the armchair-direction of the graphene [260]. Similar arrangements of phosphonic acid have been previously reported for HOPG [261]. Theoretical studies also indicate electron transfer from the graphene to the phosphonic acid suggesting its possible use as a p-type dopant.

In conclusion, many molecular arrangements on graphene are very similar to those previously reported for HOPG. However, there are also reports of clear differences which are mostly associated with the support material of the graphene. Moiré-structures of graphene on metals can induce preferred adsorption sites for

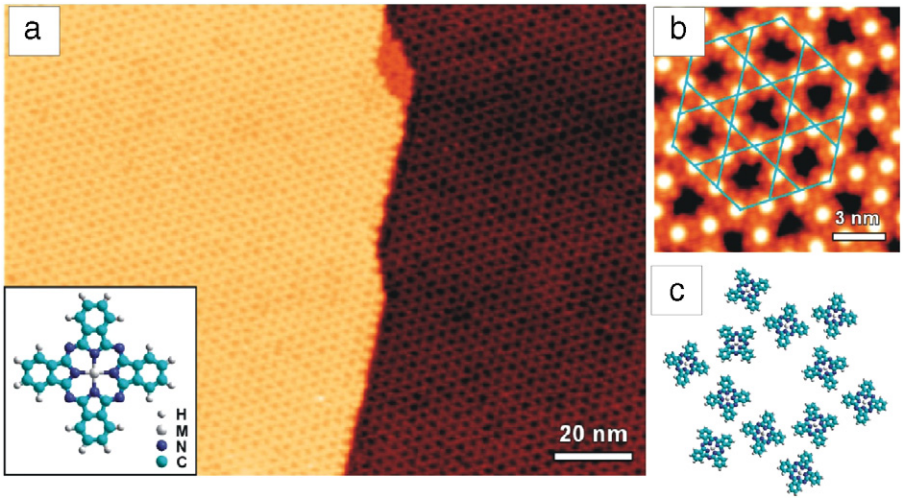

Fig. 25. STM image of a Kagome lattice of self-assembled Fe-phthalocyanines (see inset in (a)) on the moiré-patterned graphene/Ru(0001) surface (a). Detailed view of the Kagome-lattice is shown in (b) with the trihexagonal tiling highlighted. A model for the arrangement of the molecules at the surface is shown in (c).
Source: Reproduced from Ref. [254].

molecules and thus special adsorption structures may be obtained. Moiré-structures can also aid the alignment of molecules if the periodicity of the moiré-structure coincides with the molecular length/structure. One issue that has not been very well studied is how the metal substrates affect the interaction of molecules with the metal supported graphene. For metal–phthalocyanines (M-Pc) on graphene/Ni(111) it was found that the interaction of the metal-center with the underlying Ni-substrate is weak for Ni-, Cu-, and Zn-Pc while there exist stronger metal interaction channels for Fe- and Co-Pc [262]. One may expect that such different interaction also affects the ordering of the different M-Pcs on e.g. moiré-patterns. This, however, has not been observed, and in fact similar structures are reported for Fe-Pc, Ni-Pc and H_2-Pc on graphene/Ru(0001) system [254]. Therefore, a more detail understanding on how the metal substrate in addition to the formation of moiré-structures affects molecular adsorption is desirable.

7. Conclusion and outlook

The isolation of monolayer graphene as a freestanding material by mechanical exfoliation has enabled the investigation of the special physical properties arising from its linear band dispersion at the Dirac point. In addition, properties such as high charge carrier mobility, good optical transparency, and mechanical toughness makes it a promising material for microelectronic devices, transparent electrodes in optoelectronics, and a huge array of other potential applications that exploit the mechanical strength of this thinnest possible material. Some of these applications, e.g. the use of graphene in TEM grids, are already commercial products. To develop the full potential of graphene, the materials science of graphene has to be developed and the progress over the last few years has been breathtaking. We now have a very good basic understanding of how to synthesis large scale wafers of graphene, what imperfections to expect in graphene and what the properties of these imperfections are. Maybe most importantly for device applications, we have also started to understand processing methods of graphene and are developing methods to modify graphene's properties.

Graphene is the ultimate 'surface material' and therefore surface characterization methods will remain central in future studies of graphene. To date, most true surface science studies have been performed on graphene supported on their growth-substrate. This is because it allows the formation of the well defined large area single crystals necessary for many surface science investigations. Furthermore, although the transfer of graphene from metal supports to other materials has become common practice for device fabrication, there is still an issue of contamination of the graphene with e.g. polymer residues. Furthermore, a wafer-sized, single-grain graphene sample transfer to insulating/dielectric materials remains challenging. Although graphene on weak interacting metal supports is a good model system for investigating properties of graphene by surface science studies, future surface studies should be more focused on graphene on relevant substrates for applications, i.e. mainly dielectric substrate materials. Truly free-standing graphene may be ideal for transport measurements at low temperatures. However, it has been shown that for room-temperature devices, suspended graphene is less ideal because of flexural phonons increasing charge carrier scattering [263]. Therefore, it is likely that microelectronic devices will be fabricated on supported graphene, which also seems somewhat easier to achieve. Currently the best insulating support material for graphene is *h*-BN [264]. Unlike SiO_2 or other initially tried insulating substrates, *h*-BN is very uniform. Because *h*-BN is a layered 2D material, similar to graphene, it does not have any 'dangling' bonds or charge inhomogeneities. This is crucial in order to maintain the high charge carrier mobility of graphene. Therefore, in the near term we may expect more studies of graphene/*h*-BN hybrid materials. For surface science studies and also for applications the successful large area synthesis of such heterostructures will be critical. If such samples with sufficient size can be prepared, many of the graphene modification investigations we have summarized for metal or SiC supported graphene may be studied on *h*-BN as the support material.

Another challenge in designing the properties of graphene is to control modifications. We have e.g. shown that defects, like carbon vacancies and grain boundaries in graphene can have interesting properties. However, in order to utilize these defects we have to be able to define their structure (for example multiple defect structures have been reported for divacancies in graphene), density and location in the graphene. Similarly for graphene nanoribbons better control over ribbon-widths and edge structure is needed. Modifications of graphene by adsorbates also should be localized on micro to tens of nanometer scale for example for defining p- or n-type doped regions (by e.g. molecular adsorbates), or electron confinement regions (by e.g. confining pristine graphene within

hydrogen or fluorine modified graphene). In addition, in order to be able to locally modify graphene, the question of stability of the formed patterns needs to be addressed. On a one-to-few nanometers length scale, moiré-patterns formed by graphene on metals have been successfully used as templates for preferential adsorption of metals, hydrogen, and some organic molecules. These self-organization mechanisms are fascinating from a pure chemical point of view, but it is less likely that these patterns remain stable if the graphene is transferred from the metal support to another substrate and therefore these self-organization patterns may not easily be exploitable for electronic applications. On the other hand, these graphene based templates for self-organization of metal clusters may be useful systems for fundamental studies in cluster science. Thus, although graphene for electronic applications is taking the spot light, there are many other interesting aspects in fundamental research for which (supported) graphene can provide a rich resource for researchers for the various aspects of the materials science of nanostructures. The fast moving pace of graphene research will ensure that this remains an exciting field for years to come and new developments will soon add to the materials reviewed here.

Acknowledgment

The financial support from the Office of Naval Research through award # N00014-10-1-0668 is acknowledged.

References

[1] C. Lee, X.D. Wei, J.W. Kysar, J. Hone, Science 321 (2008) 385–388.
[2] W. Bao, F. Miao, Z. Chen, H. Zhang, W. Jang, C. Dames, C.N. Lau, Nat. Nanotechnol. 4 (2009) 562–566.
[3] J. Hass, W.A. de Heer, E.H. Conrad, J. Phys.: Condens. Matter 20 (2008) 323202.
[4] A. Bostwick, J. McChesney, T. Ohta, E. Rotenberg, T. Seyller, K. Horn, Prog. Surf. Sci. 84 (2009) 380–413.
[5] C. Riedl, C. Coletti, U. Starke, J. Phys. D: Appl. Phys. 43 (2010) 374009.
[6] M.S. Dresselhaus, A. Jorio, A.G. Souza, R. Saito, Phil. Trans. R. Soc. A 368 (2010) 5355–5377.
[7] M.S. Dresselhaus, A. Jorio, R. Saito, Annu. Rev. Condens. Matter Phys. 1 (2010) 89–108.
[8] P.R. Wallace, Phys. Rev. 71 (1947) 622–634.
[9] H.P. Boehm, A. Clauss, G.O. Fischer, U. Hoffmann, Z. Naturforsch. B 17 (1962) 150–153.
[10] M.S. Dresselhaus, G. Dresselhaus, Adv. Phys. 30 (1981) 139–326.
[11] H.W. Kroto, J.R. Heath, S.C. O'Brien, R.F. Curl, R.E. Smalley, Nature 318 (1985) 162–163.
[12] S. Iijima, Nature 354 (1991) 56–58.
[13] L.D. Landau, Phys. Z. Sowjetunion 11 (1937) 26.
[14] N.D. Mermin, Phys. Rev. 176 (1968) 250–254.
[15] A.E. Morgan, G.A. Somarjai, Surf. Sci. 12 (1968) 405–425.
[16] J.W. May, Surf. Sci. 17 (1969) 267–270.
[17] T.A. Land, T. Michely, R.J. Behm, J.C. Hemminger, G. Comsa, Surf. Sci. 264 (1992) 261–270.
[18] J.C. Shelton, H.R. Patil, J.M. Blakely, Surf. Sci. 43 (1974) 493–520.
[19] Y. Gamo, A. Nagashima, M. Wakabayashi, M. Terai, C. Oshima, Surf. Sci. 374 (1997) 61–64.
[20] Y.S. Dedkov, A.M. Shikin, V.K. Adamchuk, S.L. Molodtsov, C. Laubschat, A. Bauer, G. Kaindl, Phys. Rev. B 64 (2001) 035405.
[21] A.J. Van Bommel, J.E. Crombeen, A. Van Tooren, Surf. Sci. 48 (1975) 463–472.
[22] C. Berger, Z. Song, T. Li, X. Li, A.Y. Ogbazghi, R. Feng, Z. Dai, A.N. Marchenkov, E.H. Conrad, P.N. First, W.A. de Heer, J.Phys. Chem. B 108 (2004) 19912–19916.
[23] K.S. Novoselov, A.K. Geim, S.V. Morozov, D. Jiang, Y. Zhang, S.V. Dubonos, I.V. Grigorieva, A.A. Firsov, Science 306 (2004) 666–669.
[24] K.S. Novoselov, A.K. Geim, S.V. Morozov, D. Jiang, M.I. Katsnelson, I.V. Grigorieva, S.V. Dubonos, A.A. Firsov, Nature 438 (2005) 197–200.
[25] K.S. Novoselov, D. Jiang, F. Schedin, T.J. Booth, V.V. Khotkevich, S.V. Morozov, A. Geim, Proc. Natl. Acad. Sci. USA 102 (2005) 10451–10453.
[26] K.S. Novoselov, E. McCann, S.V. Morosov, V.I. Falko, M.I. Katsnelson, U. Zeitler, D. Jiang, F. Schedin, A.K. Geim, Nat. Phys. 2 (2006) 177–180.
[27] Y. Zhang, Y.W. Tan, H.L. Stromer, P. Kim, Nature 438 (2005) 201–204.
[28] Y. Zhang, J.P. Small, M.E.S. Amori, P. Kim, Phys. Rev. Lett. 94 (2005) 176803.
[29] D.A. Dikin, S. Stankovich, E.J. Zimney, R.D. Piner, G.H.B. Evemeneko, T. Nguyen, R.S. Ruoff, Nature 448 (2007) 457–460.
[30] S. Gilje, S. Han, M. Wang, K.L. Wang, R.B. Kaner, Nano Lett. 7 (2007) 3394–3398.
[31] X. Li, W. Cai, J. An, S. Kim, J. Nah, D. Yang, R. Piner, A. Velamakanni, I. Jung, E. Tutuc, S.K. Banerjee, K. Sanjay, L. Colombo, R.S. Ruoff, Science 324 (2009) 1312–1314.
[32] S. Bae, H. Kim, Y. Lee, X.F. Xu, J.S. Park, Y. Zheng, J. Balakrishnan, T. Lei, H.R. Kim, Y.I. Song, Y.J. Kim, K.S. Kim, B. Ozyilmaz, J.H. Ahn, B.H. Hong, S. Iijima, Nat. Nanotechnol. 5 (2010) 574–578.
[33] J. Wintterlin, M.L. Bocquet, Surf. Sci. 603 (2009) 1841–1852.
[34] C. Oshima, A. Nagashima, J. Phys.: Condens. Matter 9 (1) (1997).
[35] N.R. Gall, E.V. Rut'kov, A.Y. Tontegode, Internat. J. Modern Phys. B 11 (1997) 1865.
[36] A.L. Vázquez de Parga, F. Calleja, B. Borca, M.C.G. Passeggi Jr., J.J. Hinarejos, F. Guinea, R. Miranda, Phys. Rev. Lett. 100 (2008) 056807.
[37] B. Borca, S. Barja, M. Garnica, M. Minniti, A. Politano, J.M. Rodriguez-García, J.J. Hinarejos, D. Farías, A.L. Vázquez de Parga, R. Miranda, New J. Phys. 12 (2010) 093018.
[38] A.L. Vázquez de Parga, F. Calleja, B. Borca, M.C.G. Passeggi Jr., J.J. Hinarejos, F. Guinea, R. Vázquez de Parga, et al., Phys. Rev. Lett. 101 (2008) 099704.
[39] B. Wang, M.-L. Bocquet, S. Marchini, S. Günther, J. Wintterlin, Phys. Chem. Chem. Phys. 10 (2008) 3530–3534.
[40] D. Jiang, M.H. Du, S. Dai, J. Chem. Phys. 130 (2009) 074702.
[41] W. Moritz, B. Wang, M.-L. Bocquet, T. Brugger, T. Gerber, J. Wintterlin, S. Günther, Phys. Rev. Lett. 104 (2010) 136102.
[42] D. Martoccia, P.R. Willmott, T. Brugger, M. Björck, S. Günther, C.M. Schlepütz, A. Cervellino, S.A. Pauli, B.D. Patterson, S. Marchini, J. Wintterlin, W. Moritz, T. Gerber, Phys. Rev. Lett. 101 (2008) 126102.
[43] D. Martoccia, M. Björck, C.M. Schlepütz, T. Brugger, S.A. Pauli, B.D. Patterson, T. Greber, P.R. Willmott, New J. Phys. 12 (2010) 043028.
[44] M.-C. Wu, Q. Xu, D.W. Goodman, J. Phys. Chem. 98 (1994) 5104.
[45] S. Marchini, S. Günther, J. Wintterlin, Phys. Rev. B 76 (2007) 075429.
[46] A.B. Preobrajenski, M.L. Ng, A.S. VInogradov, N. Mårtensson, Phys. Rev. B 78 (2008) 073401.
[47] C. Enderlein, Y.S. Kim, A. Bostwick, E. Rotenberg, K. Horn, New J. Phys. 12 (2010) 033014.
[48] T. Brugger, Günther, B. Wang, J.H. Dil, M.L. Bocquet, J. Osterwalder, J. Wintterlin, T. Gerber, Phys. Rev. B 79 (2009) 045407.
[49] E. Sutter, D.P. Acharya, J.T. Sadowski, P. Sutter, Appl. Phys. Lett. 94 (2009) 133101.
[50] A.T. N'Diaye, J. Coraux, T.N. Plasa, C. Busse, T. Michely, New J. Phys. 10 (2008) 043033.
[51] J. Coraux, A.T. N'Diaye, C. Busse, T. Michely, Nano Lett. 8 (2008) 565–570.
[52] S. Nie, A.L. Walter, N.C. Bartelt, E. Starodub, A. Bostwick, E. Rotenberg, K.F. McCarty, ACS Nano 5 (2011) 2298–2306.
[53] J. Coraux, A.T. N'Diaye, M. Engler, C. Busse, D. Wall, N. Buckanie, F.J. Meyer zu Heringdorf, R. van Gastel, B. Poelsema, T. Michely, New J. Phys. 11 (2009) 023006.
[54] E. Loginova, S. Nie, K. Thürmer, N.C. Bartelt, K.F. McCarty, Phys. Rev. B 80 (2009) 085430.
[55] H. Hattab, A.T. N'Diaye, D. Wall, G. Jnawali, J. Coraux, C. Busse, R. van Gastel, B. Poelsema, T. Michely, F.-J. Meyer zu Heringdorf, M. Horn-von Hoegen, Appl. Phys. Lett. 98 (2011) 141903.
[56] I. Pletikosić, M. Kralj, P. Pervan, R. Brako, J. Coraux, A.T. N'Diaye, C. Busse, T. Michely, Phys. Rev. Lett. 102 (2009) 056808.
[57] E. Starodub, A. Bostwick, L. Moreschini, S. Nie, F. El Gabaly, K.F. McCarty, E. Rotenberg, Phys. Rev. B 83 (2011) 125428.
[58] C. Busse, P. Lazic, R. Dejemour, J. Coraux, T. Gerber, N. Atodiresei, V. Caiuc, R. Brako, A.T. N'Diaye, S. Buegel, J. Zegenhagen, T. Michely, Phys. Rev. Lett. 107 (2011) 036101.
[59] P. Sutter, J.T. Sadowski, E. Sutter, Phys. Rev. B 80 (2009) 245411.
[60] P. Merino, M. Svec, A.L. Pinnardi, G. Otero, J.A. Martin-Gago, ACS Nano 5 (2011) 5627–5634.
[61] M. Gao, Y. Pan, L. Huang, H. Hu, L.Z. Zhang, H.M. Guo, S.X. Du, H.-J. Gao, Appl. Phys. Lett. 98 (2011) 033101.
[62] G. Giovannetti, P.A. Khomyakov, G. Brooks, V.M. Karpan, J. van den Brink, P.J. Kelly, Phys. Rev. Lett. 101 (2008) 026803.
[63] B. Wang, X. Ma, M. Caffio, R. Schaub, W.X. Li, Nano Lett. 11 (2011) 424–430.
[64] Y. Murata, E. Starodub, B.B. Kappes, C.V. Ciobanu, N.C. Bartelt, K.F. McCarty, S. Kodambaka, Appl. Phys. Lett. 97 (2010) 143114.
[65] S.Y. Kwon, C.V. Ciobanu, V. Petrova, V.B. Shenoy, J. Bareño, V. Gambin, I. Petrov, S. Kodambaka, Nano Lett. 9 (2009) 3985–3990.
[66] E. Miniussi, M. Pozzo, A. Baraldi, E. Vesselli, R.R. Zhan, G. Comelli, T.O. Menteş, M.A. Niño, A. Locatelli, S. Lizzit, D. Alfè, Phys. Rev. Lett. 106 (2011) 216101.
[67] B. Wang, M. Caffiom, C. Bromley, H. Früchtl, R. Schaub, ACS Nano 4 (2010) 5773–5782.
[68] Y. Gamo, A. Nagashima, M. Wakabayashi, M. Terai, C. Oshima, Surf. Sci. 374 (1997) 61–64.
[69] H. Kawanowa, H. Ozawa, T. Yazaki, Y. Gotoh, R. Souda, Japan. J. Appl. Phys. 41 (2002) 6149–6152.
[70] J. Lahiri, T.S. Miller, A.J. Ross, L. Adamska, I.I. Oleynik, M. Batzill, New J. Phys. 13 (2011) 025001.
[71] J. Lahiri, Y. Lin, P. Bozkurt, I.I. Oleynik, M. Batzill, Nat. Nanotechnol. 5 (2010) 326–329.
[72] Y.S. Dedkov, M. Fonin, New J. Phys. 12 (2010) 125004.
[73] J. Lahiri, T. Miller, L. Adamska, I.I. Oleynik, M. Batzill, Nano Lett. 11 (2011) 518–522.
[74] M. Fuentes-Cabrera, M.I. Baskes, A.V. Melechko, M.L. Simpson, Phys. Rev. B 77 (2008) 035405.

[75] W. Zhao, S.M. Kozlov, O. Höfert, K. Gotterbarm, M.P.A. Lorenz, F. Vines, C. Papp, A. Görling, H.-P. Steinrück, J. Phys. Chem. Lett. 2 (2011) 759–764.
[76] A. Nagashima, N. Tejima, C. Oshima, Phys. Rev. B 50 (1994) 17487–17495.
[77] Y.S. Dedkov, M. Fonin, U. Rüdiger, C. Laubschat, Phys. Rev. Lett. 100 (2008) 107602.
[78] A. Varykhalov, J. Sánchez-Barriga, A.M. Shikin, C. Biswas, E. Vescovo, A. Rybkin, D. Marchenko, O. Rader, Phys. Rev. Lett. 101 (2008) 157601.
[79] O. Rader, A. Varykhalov, J. Sánchez-Barriga, D. Marchenko, A. Rybkin, A.M. Shikin, Phys. Rev. Lett. 102 (2009) 057602.
[80] Z.Y. Li, Z.Q. Yang, S. Qiao, J. Hu, R.Q. Wu, J. Phys.: Condens. Matter 23 (2011) 225502.
[81] D. Eom, D. Prezzi, K.T. Rim, H. Zhou, M. Lefenfeld, S. Xiao, C. Nuckolls, M.S. Hybertsen, T.F. Heinz, G.W. Flynn, Nano Lett. 9 (2009) 2844–2848.
[82] K.S. Kim, Y. Zhao, H. Jang, S.Y. Lee, J.M. Kim, K.S. Kim, J.H. Ahn, P. Kim, J.Y. Choi, B.H. Hong, Nature 457 (2009) 706.
[83] X. Li, W. Cai, L. Colombo, R.S. Ruoff, Nano Lett. 9 (2009) 4268–4272.
[84] L. Gao, J.R. Guest, N.P. Guisinger, Nano Lett. 10 (2010) 3512–3516.
[85] X. Li, C.W. Magnuson, A. Venugopal, R.M. Tromp, J.B. Hannon, E.M. Vogel, L. Colombo, R.S. Ruoff, J. Am. Chem. Soc. 133 (2011) 2816–2819.
[86] H.I. Rasool, E.B. Song, M.J. Allen, J.K. Wassei, R.B. Kaner, K.L. Wang, B.H. Weiller, J.K. Gimzewski, Nano Lett. 11 (2011) 251–256.
[87] J. Cho, L. Gao, J. Tian, H. Cao, W. Wu, Q. Yu, E.N. Yitamben, B. Fisher, J.R. Guest, Y.P. Chen, N.P. Guisinger, ACS Nano 5 (2011) 3607–3613.
[88] T. Oznuluer, E. Pince, E.O. Polat, O. Balci, O. Salihoglu, C. Kocabas, Appl. Phys. Lett. 98 (2011) 183101.
[89] L. Huang, Y. Pan, L. Pan, M. Gao, W. Xu, Y. Que, H. Zhou, Y. Wang, S. Du, H.-J. Gao, Appl. Phys. Lett. 99 (2011) 163107.
[90] Yu.S. Dedkov, A.M. Shikin, V.K. Adamchuk, S.L. Molodtsov, C. Laubschat, A. Bauer, G. Kaindl, Phys. Rev. B 64 (2001) 035405.
[91] D. Farías, A.M. Shikin, K.-H. Rieder, Yu.S. Dedkov, J. Phys.: Condens. Matter 11 (1999) 8453–8458.
[92] A.M. Shikin, V.K. Adamchuk, K.-H. Rieder, Phys. Solid State 51 (2009) 2390–2400.
[93] Y.S. Dedkov, M. Fonin, U. Rüdiger, C. Laubschat, Appl. Phys. Lett. 93 (2008) 022509.
[94] J. Lahiri, M. Batzill, Appl. Phys. Lett. 97 (2010) 023102.
[95] P.M. Stefan, M.L. Shek, I. Lindau, W.E. Spicer, L.I. Johansson, F. Herman, R.V. Kasowski, G. Brogen, Phys. Rev. B 29 (1984) 5423–5444.
[96] T. Aizawa, R. Souda, S. Otani, Y. Ishizawa, C. Oshima, Phys. Rev. B 42 (1990) 11469.
[97] T. Aizawa, R. Souda, S. Otani, Y. Ishizawa, C. Oshima, Phys. Rev. Lett. 64 (1990) 768–771.
[98] A. Nagashima, K. Nuka, K. Satoh, H. Itoh, T. Ichinokawa, C. Oshima, S. Otani, Surf. Sci. 287–288 (1993) 609–613.
[99] D. Marchenko, A. Varykhalov, A. Rybkin, A.M. Shikin, O. Rader, Appl. Phys. Lett. 98 (2011) 122111.
[100] Q.J. Wang, J.G. Che, Phys. Rev. Lett. 103 (2009) 066802.
[101] A.T. N'Diaye, S. Bleikamp, P.J. Feibelman, T. Michely, Phys. Rev. Lett. 97 (2006) 215501.
[102] B. Hammer, J.K. Norskov, Adv. Synth. Catal. 45 (2000) 71–129.
[103] P.W. Sutter, J.I. Flege, E.A. Sutter, Nat. Mater. 7 (2008) 406–411.
[104] E. Loginova, N.C. Bartelt, P.J. Feibelman, K.F. McCarty, New J. Phys. 10 (2008) 093026.
[105] E. Loginova, N.C. Bartelt, P.J. Feibelman, K.F. McCarty, New J. Phys. 11 (2009) 063046.
[106] E. Starodub, S. Maier, I. Stass, N.C. Bartelt, P.J. Feibelman, M. Salmeron, K.F. McCarty, Phys. Rev. B 80 (2009) 235422.
[107] S. Günther, S. Dänhardt, B. Wang, M.-L. Bocquet, S. Schmitt, J. Wintterlin, Nano Lett. 11 (2011) 1895–1900.
[108] A. Zangwill, D.D. Vvedensky, Nano Lett. 11 (2011) 2092–2095.
[109] P. Lacovig, M. Pozzo, D. Alfe, P. Vilmercati, A. Baraldi, S. Lizzit, Phys. Rev. Lett. 103 (2009) 166101.
[110] A.T. N'Diaye, R. van Gastel, A.J. Martínez-Galera, J. Coraux, H. Hattab, D. Wall, F.-J. Meyer zu Heringdorf, M. Horn-von Hoegen, J.M. Gómez-Rodríguez, B. Poelsema, C. Busse, T. Michely, New J. Phys. 11 (2009) 113056.
[111] G. Odahara, S. Otani, C. Oshima, M. Suzuki, T. Yasue, T. Koshikawa, Surf. Sci. 605 (2011) 1095–1098.
[112] A. Grüneis, K. Kummer, D.V. Vyalikh, New J. Phys. 11 (2009) 073050.
[113] J.J. McCarroll, T. Edmonds, R.C. Pitkethly, Nature 223 (1969) 1260–1262.
[114] C. Klink, I. Stensgaard, F. Besenbacher, E. Lægsgaard, Surf. Sci. 342 (1995) 250–260.
[115] X. Li, C.W. Magnuson, A. Venugopal, R.M. Tromp, J.B. Hannon, E.M. Vogel, L. Colombo, R.S. Ruoff, J. Am. Chem. Soc. 133 (2011) 2816–2819.
[116] J.W. Wofford, S. Nie, K.F. McCarty, N.C. Bartelt, O.D. Dubon, Nano Lett. 10 (2010) 4890–4896.
[117] C.-M. Sung, M.-F. Tai, Int. J. Refract. Met. Hard Mater. 15 (1997) 237–256.
[118] S. Nie, J. Wofford, N.C. Bartelt, O.D. Dubon, K.F. McCarty, Phys. Rev. B 84 (2011) 155425.
[119] A.J. Martinez-Galera, I. Brihuega, J.M. Gomez-Rodriguez, Nano Lett. 11 (2011) 3576–3580.
[120] T. Oznuluer, E. Pince, E.O. Polat, O. Balci, O. Salihoglu, C. Kocabas, Appl. Phys. Lett. 98 (2011) 183101.
[121] J. Wofford, E. Starodub, N.C. Bartelt, K. McCarty, Graphene growth on Au(111), in: American Vacuum Society 58th International Symposium, Nashville, 2011.
[122] A.T. N'Diaye, S. Bleikamp, P.J. Feibelman, T. Michely, Phys. Rev. Lett. 97 (2006) 215501.
[123] A.T. N'Diaye, T. Gerber, C. Busse, J. Mysliveček, J. Coraux, T. Michely, New J. Phys. 11 (2009) 103045.
[124] Y. Pan, M. Gao, L. Huang, F. Liu, H.-J. Gao, Appl. Phys. Lett. 95 (2009) 093106.
[125] K. Donner, P. Jakob, J. Chem. Phys. 131 (2009) 164701.
[126] Q. Liao, H.J. Zhang, K. Wu, H.Y. Li, S.N. Bao, P. He, Nanotechnology 22 (2011) 125303.
[127] Z. Zhou, F. Gao, D.W. Goodman, Surf. Sci. 604 (2010) L31–L38.
[128] E. Sutter, P. Albrecht, B. Wang, M.L. Bocquet, L. Wu, Y. Zhu, P. Sutter, Surf. Sci. 605 (2011) 1676–1684.
[129] M. Sicot, S. Bouvron, O. Zander, U. Rüdiger, Y.S. Dedkov, M. Fonin, Appl. Phys. Lett. 96 (2010) 093115.
[130] P.J. Feibelman, Phys. Rev. B 77 (2008) 165419.
[131] P. Feibelman, Phys. Rev. B 80 (2009) 085412.
[132] L. Liu, Z. Zhou, Q. Guo, Z. Yan, Y. Yao, D.W. Goodman, Surf. Sci. 605 (2011) L47–L50.
[133] G.G. Naumis, M. Terrones, H. Terrones, L.M. Gaggero-Sager, Appl. Phys. Lett. 95 (2009) 182104.
[134] Y.W. Son, M.L. Cohen, S.G. Louie, Nature 444 (2006) 347–349.
[135] Y.W. Son, M.L. Cohen, S.G. Louie, Phys. Rev. Lett. 97 (2006) 216803.
[136] M.Y. Han, B. Özyilmaz, Y. Zhang, P. Kim, Phys. Rev. Lett. 98 (2007) 206805.
[137] V. Barone, O. Hod, G.E. Scuseria, Nano Lett. 6 (2006) 2748–2754.
[138] X. Jia, J. Campos-Delgado, M. Terones, V. Meunier, M.S. Dresselhaus, Nanoscale 3 (2011) 86–95.
[139] L. Tapaszto, G. Dobrik, P. Lambin, L.P. Biro, Nat. Nanotechnol. 3 (2008) 397–401.
[140] S. Fujii, T. Enoki, J. Am. Chem. Soc. 132 (2010) 10034–10041.
[141] A. Sinitskii, J.M. Tour, J. Am. Chem. Soc. 132 (2010) 14730–14732.
[142] A. Dimiev, D.V. Kosynkin, A. Sinitskii, A. Slesarev, Z. Sun, J.M. Tour, Science 331 (2011) 1168–1172.
[143] H. Murayama, T. Maeda, Nature 345 (1990) 791–793.
[144] P. Mahanandia, K.K. Nanda, V. Prasad, S.V. Subramanyam, Mater. Res. Bull. 43 (2008) 3252–3262.
[145] J. Campos-Delgado, J.M. Romo-Herrera, X.T. Jia, D.A. Cullen, H. Muramatsu, Y.A. Kim, T. Hayashi, Z.F. Ren, D.J. Smith, Y. Okuno, T. Ohba, H. Kanoh, K. Kaneko, M. Endo, H. Terrones, M.S. Dresselhaus, M. Terrones, Nano Lett. 8 (2008) 2773–2778.
[146] W.H. Soe, A.M. Shikin, F. Moresco, V.K. Adamchuk, K.H. Rieder, Phys. Rev. B 64 (2001) 235404.
[147] A.M. Shikin, G.V. Prudnikova, V.K. Adamchuk, W.H. Soe, K.H. Rieder, S.L. Moldotsov, C. Laubschat, Phys. Solid State 44 (2002) 677–680.
[148] A.M. Shikin, S.A. Gorovikov, V.K. Adamchuk, W. Gudat, O. Rader, Phys. Rev. Lett. 90 (2003) 256803.
[149] M. Terai, N. Hasegawa, M. Okusawa, S. Otani, C. Oshima, Appl. Surf. Sci. 130–132 (1998) 876–882.
[150] J. Cai, P. Ruffieux, R. Jaafar, M. Bieri, T. Braun, S. Blankemburg, M. Muoth, A.P. Seitsonen, M. Saleh, X. Feng, K. Müllen, R. Fasel, Nature 466 (2010) 470–473.
[151] J.L. Li, K.N. Kudin, M.J. McAllistre, R.K. Prud'homme, I.A. Aksay, R. Car, Phys. Rev. Lett. 96 (2006) 176101.
[152] Z. Li, W. Zhang, Y. Luo, J. Yang, J.G. Hou, J. Am. Chem. Soc. 131 (2009) 6320–6321.
[153] D.V. Kosynkin, A.L. Higginbotham, A. Sinitskii, J.R. Lomeda, A. Dimiev, B.K. Price, J.M. Tour, Nature 458 (2009) 872–876.
[154] A.L. Higginbotham, D.V. Kosynkin, A. Sinitskii, Z. Sun, J.M. Tour, ACS Nano 4 (2010) 2059–2069.
[155] L. Jiao, L. Zhang, X. Wang, G. Diankov, H. Dai, Nature 458 (2009) 877–880.
[156] A.G. Cano-Marquez, F.J. Rodríguez-Macıas, J. Campos-Delgado, C.G. Espinosa-Gonzalez, F. Tristan-Lopez, D. Ramírez-Gonzalez, D.A. Cullen, D.J. Smith, M. Terrones, Y.I. Vega-Cantu, Nano Lett. 9 (2009) 1527–1533.
[157] L.C. Campos, V.R. Manfrinato, J.D. Sanchez-Yamagishi, J. Kong, P. Jarillo-Herrero, Nano Lett. 9 (2009) 2600–2604.
[158] L. Ci, Z. Xu, L. Wang, W. Gao, F. Ding, K.F. Kelly, B.I. Yakobson, P.M. Ajayan, Nano Res. 1 (2008) 116–122.
[159] S.S. Datta, D.R. Strachan, S.M. Khamis, A.T.C. Johnson, Nano Lett. 8 (2008) 1912–1915.
[160] L. Zhang, S. Diao, Y. Nie, K. Yan, N. Liu, B. Dai, A. Reina, J. Kong, Z. Liu, J. Am. Chem. Soc. 133 (2011) 2706–2713.
[161] L. Xie, L. Jiao, H. Dai, J. Am. Chem. Soc. 132 (2010) 14751–14753.
[162] X. Wang, H. Dai, Nat. Chem. 2 (2010) 661–665.
[163] Y. Cui, Q. Fu, X. Bao, Phys. Chem. Chem. Phys. 12 (2010) 5053–5057.
[164] E. Starodub, N.C. Bartelt, K.F. McCarty, J. Phys. Chem. C 114 (2010) 5134–5140.
[165] Y. Cui, Q. Fu, H. Zhang, D. Tan, X. Bao, J. Phys. Chem. C 113 (2009) 20365–20370.
[166] P. Sutter, J.T. Sadowski, E.A. Sutter, J. Am. Chem. Soc. 132 (2010) 8175–8179.
[167] O.V. Yazyev, I. Tavernelli, U. Rothlisberger, L. Helm, Phys. Rev. B 75 (2007) 115418.
[168] J. Kotakoski, C.H. Jin, O. Lehtinen, K. Suenaga, A.V. Krasheminnikov, Phys. Rev. B 81 (2010) 113404.
[169] R.F. Egerton, P. Li, M. Malec, Micron 35 (2004) 399–409.
[170] B.W. Smith, D.W. Luzzi, J. Appl. Phys. 90 (2001) 3509–3515.
[171] F. Banhart, Rep. Progr. Phys. 62 (1999) 1181–1222.
[172] J.H. Warner, M.H. Rümmeli, L. Ge, T. Gemming, B. Montanari, N.H. Harrison, B. Büchner, G.A.D. Briggs, Nat. Nanotechnol. 4 (2009) 500–504.
[173] C. Jin, L. Haiping, P. Lianmao, K. Suenaga, S. Iijima, Phys. Rev. Lett. 102 (2009) 205501.
[174] J. Kotakoski, A.V. Krasheninnikov, U. Kaiser, J.C. Meyer, Phys. Rev. Lett. 106 (2011) 105505.

[175] M.D. Fischbein, M. Drndić, Appl. Phys. Lett. 93 (2008) 113107.
[176] Z. Xu, L. Chen, J. Li, R. Wang, X. Qian, X. Song, L. Liu, G. Chen, Appl. Phys. Lett. 98 (2011) 183112.
[177] A.A. El-Barbary, R.H. Telling, C.P. Ewels, M.I. Heggie, P.R. Briddon, Phys. Rev. B 68 (2003) 144107.
[178] L. Li, S. Reich, J. Robertson, Phys. Rev. B 72 (2005) 184109.
[179] J. Ma, D. Alfé, A. Michaelides, E. Wang, Phys. Rev. B 80 (2009) 033407.
[180] J.C. Meyer, C. Kisielowski, R. Erni, M.D. Rossell, M.F. Crommie, A. Zettl, Nano Lett. 8 (2008) 3582–3586.
[181] E. Cockayne, G.M. Rutter, N.P. Guisinger, J.N. Crain, P.N. First, J.A. Stroscio, Phys. Rev. B 83 (2011) 195425.
[182] H.J. Park, V. Skákalová, J. Meyer, D.S. Lee, T. Iwasaki, C. Bumby, U. Kaiser, S. Roth, Phys. Status Solidi B 247 (2010) 2915–2919.
[183] G.M. Rutter, J.N. Crain, N.P. Guisinger, T. Li, P.N. First, J.A. Stroscio, Science 317 (2007) 219–222.
[184] N.P. Guisinger, G.M. Rutter, J.N. Crain, C. Heiliger, P.N. First, J.A. Stroscio, J. Vac. Sci. Technol. A 26 (2008) 932.
[185] A.V. Krasheninnikov, P.O. Lehtinen, A.S. Foster, R.M. Nieminen, Chem. Phys. Lett. 418 (2006) 132–136.
[186] O. Cretu, A.V. Krasheninnikov, J.A. Rodriguez-Manoz, L. Sun, R.M. Nieninen, F. Banhart, Phys. Rev. Lett. 105 (2010) 196102.
[187] G.D. Lee, C.Z. Wang, E. Yoon, N.M. Hwang, D.Y. Kim, K.M. Ho, Phys. Rev. Lett. 95 (2005) 205501.
[188] M.T. Lusk, D.T. Wu, L.D. Car, Phys. Rev. B 81 (2010) 155444.
[189] M.T. Lusk, L.D. Car, Phys. Rev. Lett. 100 (2008) 175503.
[190] H. Terrones, M. Terrones, E. Hernández, N. Grobert, J.-C. Charlier, P.M. Ajayan, Phys. Rev. Lett. 84 (2000) 1716.
[191] D.W. Boukhvalov, M.I. Katsnelson, Nano Lett. 8 (2008) 4373–4379.
[192] G. Cantele, Y.S. Lee, D. Ninno, N. Marzari, Nano Lett. 9 (2009) 3425–3429.
[193] J.M. Englert, C. Dotzer, G. Yang, M. Schmid, C. Papp, J.M. Gottfried, H.P. Steinrück, E. Spiecker, F. Hauke, A. Hirsch, Nat. Chem. 3 (2011) 279–287.
[194] A.H. Castro Neto, F. Guinea, N.M.R. Peres, K.S. Novoselov, A.K. Geim, Rep. Progr. Phys. 81 (2009) 109–162.
[195] M.M. Ugeda, I. Brihuega, F. Guinea, J.M. Gómez-Rodríguez, Phys. Rev. Lett. 104 (2010) 096804.
[196] X. Peng, R. Ahuja, Nano Lett. 8 (2008) 4464–4468.
[197] D.J. Appelhans, L.D. Carr, M.T. Lusk, New J. Phys. 12 (2010) 125006.
[198] L.S. Panchakarla, K.S. Subrahmanyam, S.K. Saha, A. Govindaraj, H.R. Krishnamurthy, U.V. Waghmare, C.N.R. Rao, Adv. Mater. 21 (2009) 4726–4730.
[199] D. Wei, Y. Liu, Y. Wang, H. Zhang, L. Huang, G. Yu, Nano Lett. 9 (2009) 1752–1758.
[200] G. Imamura, K. Saiki, J. Phys. Chem. C 115 (2011) 10000–10005.
[201] Y.C. Lin, C.Y. Lin, P.W. Chiu, Appl. Phys. Lett. 96 (2010) 133110.
[202] Y. Wang, Y. Shao, D.W. Matson, J. Li, Y. Lin, ACS Nano 4 (2010) 1790–1798.
[203] H.M. Jeong, J.W. Lee, W.H. Shin, Y.J. Choi, H.J. Shin, J.K. Kang, J.W. Choi, Nano Lett. 11 (2011) 2472–2477.
[204] K. Brenner, R. Murali, Appl. Phys. Lett. 98 (2011) 113115.
[205] B. Guo, Q. Liu, E. Chen, H. Zhu, L. Fang, J.R. Gong, Nano Lett. 10 (2010) 4975–4980.
[206] X. Wang, X. Li, L. Zhang, Y. Yoon, P.K. Weber, H. Wang, J. Guo, H. Dai, Science 324 (2009) 768–771.
[207] J.C. Meyer, S. Kurasch, H.J. Park, V. Skakalova, D. Künzel, A. Groß, A. Chuvilin, G. Algara-Siller, S. Roth, T. Iwasaki, U. Starke, J.H. Smet, U. Kaiser, Nat. Mater. 10 (2011) 210–215.
[208] S.M.M. Dubois, A. Lopez-Bezanilla, A. Cresti, F. Triozon, B. Biel, J.-C. Charlier, S. Roche, ACS Nano 4 (2010) 1971–1976.
[209] E.J.H. Lee, K. Balasubramanian, R.T. Weitz, M. Burghard, K. Kern, Nat. Nanotechnol. 3 (2008) 486–490.
[210] Ç.Ö. Girit, J.C. Meyer, R. Erni, M.D. Rossell, C. Kisielowski, L. Yang, C.-H. Park, M.F. Crommie, M.L. Cohen, S.G. Louie, A. Zettl, Science 323 (2009) 1705–1708.
[211] X. Jia, M. Hofmann, V. Meunier, B.G. Sumpter, J. Campos-Delgado, J.M. Romo-Herrera, H. Son, Y.-P. Hsieh, A. Reina, J. Kong, M. Terrones, M.S. Dresselhaus, Science 323 (2009) 1701–1705.
[212] P. Koskinen, S. Malola, H. Hakkinen, Phys. Rev. Lett. 101 (2008) 115502.
[213] K. Suenaga, M. Koshino, Nature 468 (2010) 1088.
[214] K.A. Ritter, J.W. Lyding, Nat. Mater. 8 (2009) 235–242.
[215] C. Tao, L. Jiao, O.V. Yazyev, Y.C. Chen, J. Feng, X. Zhang, R.B. Capaz, J.M. Tour, A. Zettl, S.G. Louie, H. Dai, M.F. Crommie, Nat. Phys. 7 (2011) 616–620.
[216] H. Yang, A.J. Mayne, M. Boucherit, G. Comtet, G. Dujardin, Y. Kuk, Nano Lett. 10 (2010) 943–947.
[217] K. Nakada, M. Fujita, G. Dresselhaus, M.S. Dresselhaus, Phys. Rev. B 54 (1996) 17954–17960.
[218] Y. Kobayashi, K. Fukui, T. Enoki, Phys. Rev. B 73 (2006) 125415.
[219] P. Simonis, C. Goffaux, P.A. Thiry, L.P. Biro, P. Lambin, V. Meunier, Surf. Sci. 511 (2002) 319–322.
[220] Q. Yu, L.A. Jauregui, W. Wu, R. Colbym, J. Tian, Z. Su, H. Cao, Z. Liu, D. Pandey, D. Wei, T.F. Chung, P. Peng, N.P. Guisinger, E.A. Stach, J. Bao, S.-S. Pei, Y.P. Chen, Nat. Mater. 10 (2011) 443–449.
[221] R. van Gastel, A.T. N'Diaye, D. Wall, J. Coraux, C. Busse, N.M. Buckanie, F.-J. Meyer zu Heringdorf, T. Michely, B. Poelsema, Appl. Phys. Lett. 95 (2009) 121901.
[222] F.S. Khokhar, R. van Gastel, B. Poelsema, Phys. Rev. B 82 (2010) 205409.
[223] P.Y. Huang, C.S. Ruiz-Vargas, A.M. van der Zande, W.S. Whitney, M.P. Levendorf, J.W. Kevek, S. Garg, J.S. Alden, C.J. Hustedt, Y. Zhu, J. Park, P.I. McEuen, D.A. Muller, Nature 469 (2011) 389–392.
[224] K. Kim, Z. Lee, W. Regan, C. Kisielowski, M.F. Crommie, A. Zettl, ACS Nano 5 (2011) 2142–2146.
[225] J. An, E. Voelkl, J.W. Suk, X. Li, C.W. Magnuson, L. Fu, P. Tiemeijer, M. Bischoff, B. Freitag, E. Popova, R.S. Ruoff, ACS Nano 5 (2011) 2433–2439.
[226] R. Grantab, V.B. Shenoy, R.S. Ruoff, Science 330 (2010) 946–948.
[227] O.V. Yazyev, S.G. Louie, Phys. Rev. B 81 (2010) 195420.
[228] D. Gunlycke, C.T. White, Phys. Rev. Lett. 106 (2011) 136806.
[229] L. Ci, L. Song, C. Jin, D. Jariwala, D. Wu, Y. Li, A. Srivastava, Z.F. Wang, K. Storr, L. Balicas, F. Liu, P.M. Ajayan, Nat. Mater. 9 (2010) 430.
[230] J.O. Sofo, A.S. Chaudhari, G.D. Barber, Phys. Rev. B 75 (2007) 153401.
[231] J. Zhou, M.M. Wu, X. Zhou, Q. Sun, Appl. Phys. Lett. 95 (2009) 103108.
[232] D.C. Elias, R.R. Nair, T.M.G. Mohiuddin, S.V. Morozov, P. Blake, M.P. Halsall, A.C. Ferrari, D.W. Boukhvalov, M.I. Katsnelson, A.K. Geim, K.S. Novoselov, Science 323 (2009) 610–613.
[233] P. Sessi, J.R. Guest, M. Bode, N.P. Guisinger, Nano Lett. 9 (2009) 4343–4347.
[234] R. Balog, B. Jørgensen, J. Wells, E. Lægsgaard, P. Hofmann, F. Besenbacher, L. Hornekær, J. Am. Chem. Soc. 131 (2009) 8744–8745.
[235] R. Balog, B. Jørgensen, L. Nilsson, M. Andersen, E. Rienks, M. Bianchi, M. Fanetti, E. Lægsgaard, A. Baraldi, S. Lizzit, Z. Sljivancanin, F. Besenbacher, B. Hammer, T.G. Pedersen, P. Hofmann, L. Hornekær, Nat. Mater. 9 (2010) 315–319.
[236] N. Guisinger, G. Rutter, J. Crain, P. First, J. Stroscio, Nano Lett. 9 (2009) 1462–1466.
[237] S. Oark, R.S. Ruoff, Nat. Nanotechnol. 4 (2009) 217.
[238] G. Eda, M. Chhowalla, Adv. Mater. 22 (2010) 2392.
[239] N.A. Vinogradov, K. Schulte, M.L. Ng, A. Mikkelsen, E. Lundgren, N. Mårtensson, A.B. Preobrajenski, J. Phys. Chem. C 115 (2011) 9568–9577.
[240] R. Zbořil, F. Karlický, A.B. Bourlinos, T.A. Steriotis, A.K. Stubos, V. Georgakilas, K. Šafářová, D. Jančík, C. Trapalis, M. Otyepka, Small 6 (2010) 2885–2891.
[241] R.R. Nair, W. Ren, R. Jalil, I. Riaz, V.G. Kravets, L. Britnell, P. Blake, F. Schedin, A.S. Mayorov, S. Yuan, M.I. Katsnelson, H.M. Cheng, W. Strupinski, L.G. Bulusheva, A.V. Okotrub, I.V. Grigorieva, A.N. Grigorenko, K.S. Novoselov, A.K. Geim, Small 6 (2010) 2877–2884.
[242] J.T. Robinson, J.S. Burgess, C.E. Junkermeier, S.C. Badescu, T.L. Reinecke, F.K. Perkins, M.K. Zalalutdniov, J.W. Baldwin, J.C. Culbertson, P.E. Sheehan, E.S. Snow, Nano Lett. 10 (2010) 3001–3005.
[243] F. Schedin, A.K. Geim, S.V. Morozov, E.W. Hill, P. Blake, M.I. Katnelson, K.S. Novoselov, Nat. Mater. 6 (2007) 652.
[244] T.O. Wehling, K.S. Novoselov, S.V. Morozov, E.E. Vdovin, M.I. Katnelson, A.K. Geim, A.I. Lichtenstein, Nano Lett. 8 (2008) 173.
[245] A.B. Kuzmenko, E. van Heumen, F. Carbone, D. van der Marel, Phys. Rev. Lett. 100 (2008) 117401.
[246] W. Chen, D. Qi, X. Gao, A.T.S. Wee, Prog. Surf. Sci. 84 (2009) 279–321.
[247] T. Ohta, A. Bostwick, T. Seyller, K. Jorn, E. Rotenberg, Science 313 (2006) 951–954.
[248] Y.J. Yu, Y. Zhao, S. Ryu, L.E. Brus, K.S. Kim, P. Kim, Nano Lett. 9 (2009) 3430–3434.
[249] W. Chen, S. Chen, D.C. Qi, X.Y. Gao, A.T.S. Wee, J. Am. Chem. Soc. 129 (2007) 10418–10422.
[250] C. Coletti, C. Riedl, D.S. Lee, B. Krauss, L. Patthey, K. von Klitzing, J.H. Smet, U. Starke, Phys. Rev. B 81 (2010) 235401.
[251] X. Dong, D. Fu, W. Fang, Y. Shi, P. Chen, L.J. Li, Small 5 (2009) 1422–1426.
[252] Y.H. Lu, W. Chen, Y.P. Feng, P.M. He, J. Phys. Chem. B 113 (2009) 2–5.
[253] S. Barja, M. Garnica, J.J. Hinarejos, A.L. Vázquez de Parga, N. Martín, R. Miranda, Chem. Commun. 46 (2010) 8198–8200.
[254] J. Mao, H. Zhang, Y. Jiang, Y. Pan, M. Gao, W. Xiao, H.-J. Gao, J. Am. Chem. Soc. 131 (2009) 14136.
[255] I. Syôzi, Progr. Theoret. Phys. 6 (1951) 306–308.
[256] A.J. Pollard, E.W. Perkins, N.A. Smith, A. Saywell, G. Goretzki, A.G. Phillips, S.P. Argent, H. Sachdev, F. Müller, S. Hüfner, S. Gsell, M. Fischer, M. Schreck, J. Osterwalder, T. Greber, S. Berner, N.R. Champness, P.H. Beton, Angew. Chem. Int. Ed. 49 (2010) 1794–1799.
[257] Q.H. Wang, M.C. Hersam, Nat. Chem. 1 (2009) 206–211.
[258] H. Huang, S. Chen, X. Gao, W. Chen, A.T.S. Wee, ACS Nano 3 (2009) 3431–3436.
[259] W.H. Lee, J. Park, S.H. Sim, S. Lim, K.S. Kim, B.H. Hong, K. Cho, J. Am. Chem. Soc. 133 (2011) 4447–4454.
[260] M.C. Prado, R. Nascimento, L.G. Moura, M.J.S. Matos, M.S.C. Mazzoni, L.G. Cancado, H. Chacham, B.R.A. Neves, ACS Nano 5 (2011) 394–398.
[261] G.N. Fontes, B.R.A. Neves, Langmuir 21 (2005) 11113–11118.
[262] W. Dou, S. Huang, R.Q. Zhang, C.S. Lee, J. Chem. Phys. 134 (2011) 094705.
[263] E.V. Castro, H. Ochoa, M.I. Katsnelson, R.V. Gorbachev, D.C. Elias, K.S. Novoselov, A.K. Geim, F. Guinea, Phys. Rev. Lett. 105 (2010) 266601.
[264] R. Decker, Y. Wang, V.W. Brar, W. Regan, H.Z. Tsai, Q. Wu, W. Gannett, A. Zettl, M.F. Crommie, Nano Lett. 11 (2011) 2291–2295.
[265] C. Gong, G. Lee, B. Shan, E.M. Vogel, R.M. Wallace, K. Cho, J. Appl. Phys. 108 (2010) 123711.
[266] M. Vanin, J. Mortensen, A.K. Kelkkanen, J.M. Garcia-Lastra, K.S. Thygesen, K.W. Jacobsen, Phys. Rev. B 81 (2010) 081408(R).